Surya Deo Yadav, M.Tech.

Creep study of 9-12% Cr steels for power plants

DOCTORAL THESIS

to achieve the university degree of

Doktor der technischen Wissenschaften

submitted to

Graz University of Technology

Supervisor

Assoc. Prof. Dr. tech. Cecilia Poletti

Institute of Materials Science and welding

Graz, April 2016

AFFIDAVIT

I declare that I have authored this thesis independently, that I have not used other than the declared sources/resources, and that I have explicitly indicated all material which has been quoted either literally or by content from the sources used. The text document uploaded to TUGRAZonline is identical to the present doctoral thesis.

Date

Signature

Abstract

In this research work we investigated the nature of cavities, developed both a cavity growth and a hybrid creep model, and studied the substructure evolution during creep. P91 was selected for the cavitation study, P92 for the creep model and a novel 12% Cr steel to study the substructure evolution during creep. Creep experiments were carried out to support this work employing both interrupted and continuous creep testing techniques.

Light optical microscope (LOM), conventional scanning electron microscope (SEM) and computed tomography (CT) were employed to investigate pre-existing cavities in P91 steel. FEG-SEM equipped with in-lens detector was found to be a correct choice to distinguish AlN from cavities formed during creep. The growth of pre-existing cavities was described using a developed physical growth model based on migration of vacancies. From this research it was deduced that pre-existing cavities are detrimental for the creep resistance of power plants components. The number density and volume fraction of creep cavities was obtained from 2D stereological method and the results were compared to those obtained from FIB serial sectioning and 3D reconstruction. It was found that 2D stereological method overestimated the number density and volume fraction of cavities due to the actual complex shape of cavities not taken into account in the stereological analysis.

The hybrid creep model was developed combining a physical model with continuum damage mechanics approach (CDM). Physical model accounted for the substructure evolution and CDM approach accounted for the damage in material during creep. The model was validated using the experimental data of P92 such as creep strain (up to onset of tertiary stage), dislocation density and subgrain size. For the first time the evolution of internal variables involved in the model was thoroughly discussed.

Transmission electron microscopy (TEM), X-ray diffraction (XRD) and electron backscatter diffraction (EBSD) were used to characterize the substructure of a 12% Cr steel. The distinction among mobile, dipole and boundary dislocations was achieved by applying all three techniques together. Total dislocation density was evaluated applying EBSD and TEM. This research also revealed that heat treatments carried out in the as-received condition significantly influenced the starting configuration of dislocations. This last point should be taken into account for the development and validation of future creep models.

Kurzfassung

In dieser Arbeit untersuchten wir das Verhalten von Poren, entwickelten ein Porenwachstums- sowie ein Hybridkriechmodel, und studierten die Entwicklung der Substruktur während des Kriechens. Für diese Untersuchungen wurden ein P91 Stahl, ein P92 Stahl sowie ein neuartiger 12% Cr-Stahl herangezogen. Zur weiteren Unterstützung dieser Arbeit wurden unterbrochene sowie kontinuierliche Kriechversuche durchgeführt.

Diverse Mikroskopietechniken wurden angewandt um die Poren im P91 Stahl eingehend zu untersuchen. Lichtmikroskopie (LOM), konventionelle Rasterelektronenmikroskopie (REM), sowie Computertomographie (CT) wurden verwendet um bereits vorhandene Poren im Material zu untersuchen. Die Feldemissions-Rasterelektronenmikroskopie wurde herangezogen um AlN von Poren welche sich während des Kriechens gebildet haben unterscheiden zu können. Des Weiteren wurde das Wachstum von bereits vorhandenen Poren untersucht. Dazu wurde ein physikalisches Wachstumsmodell welches auf der Bewegung von Leerstellen basiert entwickelt. Von diesem Teil der Arbeit konnte gefolgert werden, dass sich bereits vorhandene Poren negativ auf den Kriechwiderstand von Kraftwerkskomponenten auswirken. Die Teilchendichte sowie der Volumenanteil an Kriechporen wurden mittels einer 2D stereologischen Methode bestimmt. Diese Ergebnisse wurden mit jenen Ergebnissen welche durch fokussierte Ionenstrahlmessungen (FIB) und 3D Rekonstruierungen erhalten wurden, verglichen. Dabei stellte sich heraus, dass die 2D stereologischen Ergebnisse sowohl die Teilchendichte als auch den Volumenanteil der Poren auf Grund der komplexen Geometrie der Poren, überschätzten.

Als weiterer Punkt in der vorliegenden Arbeit, wurde ein Hybridkriechmodell basierend auf einer Kombination aus physikalischem Modell mit einem Kontinuums Mechanik (CDM) Ansatz entwickelt. Das darin enthaltene physikalische Modell wurde verwendet um die Substrukturentwicklung zu beschreiben. Der CDM Ansatz wurde dabei angewandt um den Schaden im Material während des Kriechens aufzuzeigen. Das entwickelte Hybridkriechmodell wurde mittels experimentell erhaltenen Daten des P92 Stahls, wie Kriechdehnung bis zum Beginn der tertiären Stufe, der Versetzungsdichte und der Subkorngröße validiert. Zum ersten Mal wurde die Entwicklung von internen Variablen des Modells ausführlich diskutiert.

Um die Substruktur des 12% Cr-Stahls zu charakterisieren, wurden Transmissionselektronenmikroskopie (TEM), Röntgenbeugung (XRD) und EBSD Messungen durchgeführt. Die Unterscheidung von Versetzungen bezüglich ihrer Art, ob beweglich, mit Dipolcharakter oder als Subkorngrenzenversetzungen, wurde durch die Kombination dieser drei genannten Techniken erreicht. Die gesamte Versetzungsdichte wurde mittels EBSD und TEM bestimmt. Diese Arbeit zeigte außerdem, dass Wärmebehandlungen welche am Ausgangsmaterial durchgeführt wurden, die Ausgangskonfiguration der Versetzungen stark beeinflussten. Dieser letzte Punkt sollte für die Entwicklung und Validierung weiterer Kriechmodelle berücksichtigt werden.

Acknowledgement

I am highly indebted to Assoc. Prof. Dr. Cecilia Poletti for accepting me as a PhD student and encouraging me to undertake this dissertation as well as providing me all the necessary guidance, moral and inspirational support throughout the study. The words couldn't express my gratitude for her.

I also express my sincere thanks to Prof. Dr. B. Sonderegger and Dr. C. Beal for their fruitful discussions and encouragement throughout the work.

Many thank to Prof. Dr. C. Sommitsch for his support, scientifically as well as shorting the other administrative difficulties in the beginning of PhD admission.

I also like to express my gratitude to Prof. Groma, Prof. Resel, Dr. Sartory, Dr. Brunner, Dr. Rosc, Szilvia and Dr. Domankova for supporting the work with different experiments and to share their knowledge.

Special thanks to my friends from Lab: Thomas, Kerschi, Gernot, Leander, Herbert and all others for their valuable support, guidance and co-operations.

Many thank to Isabella, Manuela, Claudia and Sandra for their instant help and support in different issues. Thanks to Daniela from Welcome Centre (TUG) for many administrative help.

I would like to thank all my colleagues and friends: Schlachi, Ernst, Johannes, Romain, Dilek, David, Martina, Claudia, Fritz, Fernando, Muhammad, Stojan, Monica, Thierry, Bernedette, Bernhard, Kashyap, Karthik, Matia and Gita for sharing valuable information as well as motivating me on different occasions.

I also express my sincere thanks to friends from IIT Roorkee: Sandan, Sanjeev and Neeraj. Special thanks to Assoc. Prof. Dr. G. P. Chaudhari for boosting my confidence.

I would like to thanks my parents and my family members for all kind of support during the work period.

Financial support from FFG Project Hot-Pipes, Grant no. 826434 and European commission project Z-Ultra, Grant no. 309916 is thankfully acknowledged.

At last I would like to thanks the Almighty for being with me all the time.

Table of Contents

1. Introduction and state of the Art

The dependency on fossil fuel steam power plants will still remain for many years to fulfil the growing power demand of the world, until highly efficient technologies based on non-conventional resources are not fully developed. Working principle of these power plants is based on the steam energy that is converted into mechanical energy and further transformed into electrical energy. The power plants require large amount of materials with good high temperature properties for constructing different components. 9-12% Cr steels are used to fabricate many components of these power plants. The different aspects of these steels are briefly discussed in the subsections below. Furthermore, a description of creep models developed until now is summarized.

1.1 9-12% Cr steels

9-12% Cr steels with martensitic/ferritic structure are appropriate candidates for power plant components such as super heater tubes, boiler tubes and large forgings, due to their low cost and good high temperature properties [1-10]. They combine creep strength, thermal fatigue and oxidation resistance up to a certain extent [11]. Recently developed 9 Cr steels are suitable only for up to 600 °C/300 bar. This operating condition resulted in an increase of the efficiency from 30-35% to 42-47% and a decrease of 30% of specific CO_2 emission when comparing with subcritical plants (540 °C/180 bar) [1]. To protect the environment from greenhouse gases as well as meeting the power demand, the efficiency of power plants should be raised more, and that relies on steam condition. For that purpose we need to increase the temperature and pressure of steam and the power plant components should have desired properties to resist this temperature and pressure for long time without large deformations or breakage. The current developments are focused at 650 °C/325 bar steam condition. 9% Cr steels have shown good creep strength at 650 °C. Apart from creep resistance, high temperature oxidation has to be taken into account. 9% Cr steels are not resistant enough. Thus, they must be coated or the amount of Cr should be increased to achieve desired oxidation resistance. Many attempts have been made to develop 11-12% Cr steels in the last decades. These steels have offered excellent short term creep strength but failed dramatically due to microstructural degradation during long term tests, generally after 10000 h [11-13].

One might suggest that austenitic steels or Ni base alloy such as: 617, 625 and 263 can be used as replacement for the martensitic steels due to their excellent properties at high temperatures. These alloys are very expensive in comparison to martensitic steels. Thus, martensitic steels are still drawing the attention of the global market in such applications. Simplified relative costs of different materials such as carbon steel, low alloyed steel, 9-12% Cr steel, austenitic steel and nickel base alloys are compared in Figure 1.

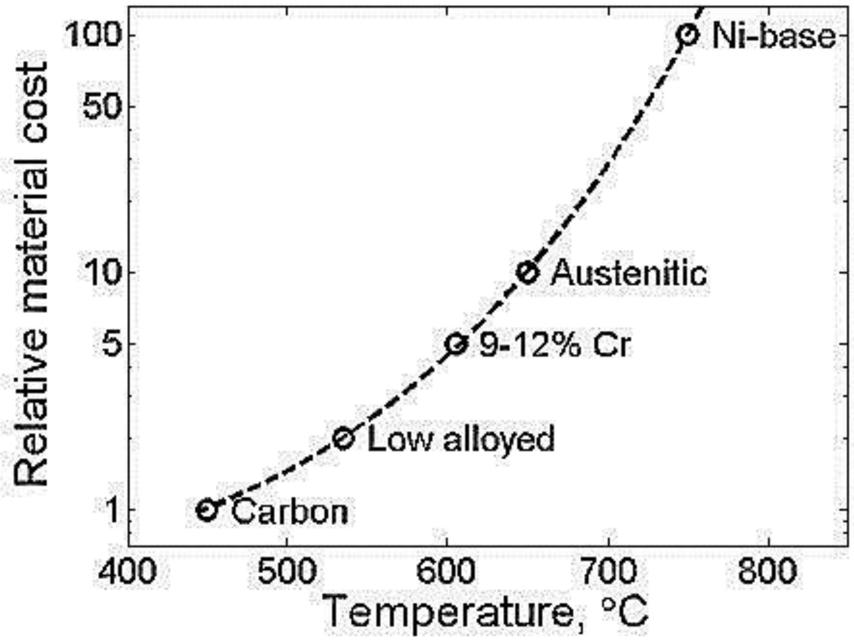

Figure 1. Relative costs of the potential materials for power plants applications [14]

1.2 Microstructure

In tempered condition, also frequently designated as as-received condition, the microstructure of the martensitic steels comprises of prior austenitic grain boundaries (PAGBs), blocks, packets, laths and subgrains boundaries. These boundaries are decorated with $M_{23}C_6$ carbides while MX type carbonitrides are distributed throughout the matrix [15]. The substructure consists of different dislocations types. According to their location and energy they can be classified into: mobile, dipoles and boundary [16]. Subgrain boundaries are the manifestation of boundary dislocations configured in low energy positions. The interior of subgrains contain mobile and dipole dislocations with different energies.

The creep strength relies on stability of microstructure during the exposure. The different strengthening mechanisms reported in the literature are discussed briefly in the next section.

1.3 Strengthening mechanisms

The basic high temperature strengthening mechanisms reported in the literature for these steels are: solid solution strengthening, precipitate strengthening, dislocation strengthening and subgrain-boundary strengthening.

1.3.1 Solid solution strengthening

Alloying elements such as Mo and W with atomic radii different from solvent iron atom radii provides solid solution strengthening due to the Hume-Rothery size effect [17-19]. The alloying elements produce a local strain field in the matrix that offers additional resistance to the plastic deformation. The effect can be explained due to differences in the size of atoms and shear modulus. For accounting atomic size differences, a misfit parameter is defined as:

$$\delta = \frac{1}{a}\frac{da}{dC_0} \qquad (1)$$

where a is the lattice parameter and C_0 the concentration of solute atom in the respective matrix.

Similarly, the shear modulus effect can be given as:

$$\eta = \frac{1}{G}\frac{dG}{dC_0} \qquad (2)$$

where G is the shear modulus. The increase in solid solution strengthening $\Delta\sigma_{sss}$ due to the incorporation of solute atoms can be given empirically as:

$$\Delta\sigma_{sss} \sim (\sqrt{\delta^2 + \eta^2}\,)^m \cdot \ {C_0}^n \quad (3)$$

where exponent m lies in the range of 1-2 and n lies between 0.5-1, depending on solute concentration and temperature.

1.3.2 Precipitate strengthening

The second phase particles stabilize the substructure and retard recovery during creep.

Fine MX type precipitates distributed throughout the matrix impede the dislocation movement. The Orowan stress σ_{or} for dislocation to pass through the precipitates is given as [17, 20]:

$$\sigma_{or} = c_1 MGb/\lambda \qquad (4)$$

where c_1 is a constant, M is the Taylor factor, b is the Burgers vector and λ is the average inter-precipitate spacing.

Apart from MX precipitates, large $M_{23}C_6$ carbides pin the subgrain boundaries and retard their growth during the creep exposure. The formulation proposed by Zener [21] for the pressure produced by the precipitates P_{ZD}, also known as Zener drag pressure, can be given as:

$$P_{ZD} = 2\pi r_P^2 N_p \gamma_{sb} \qquad (5)$$

where r_p is the mean radius of precipitates, N_p is the number density of precipitates and γ_{sb} is the surface energy of subgrains.

1.3.3 Dislocation strengthening

The free dislocations inside the subgrains are obstacles to the movement of other dislocations due to their long range stress fields. The dislocation hardening $\sigma_\rho$can be given as [17, 20]:

$$\sigma_\rho = c_2 MGb\sqrt{\rho_f} \qquad (6)$$

where c_2 is a constant and ρ_f is the free dislocation density inside the subgrains.

1.3.4 Subgrain-boundary strengthening

The subgrain boundaries have been treated as strengthening element by Maruyama [22] and accordingly the subgrain boundary strengthening can be given as [17, 22]:

$$\sigma_{sg} = 10Gb/\lambda_{sg} \qquad (7)$$

where λ_{sg} is minimum width of elongated subgrains. In literature subgrain hardening is also considered based on Hall-Patch approach and is given as:

$$\sigma_{sg} = k_{sg}/\sqrt{d_{sg}} \qquad (8)$$

where k_{sg} is the strengthening coefficient and d_{sg} the equivalent subgrain size.

1.4 Microstructural degradation during creep

When materials are loaded under the application of an external force, the microstructure evolves due to diffusional and relaxation processes. Dislocation density decreases due to recovery and subgrains coarsen with ongoing creep. The second phase particles/precipitates are non-deformable plastically and are unstable from the thermodynamic point of view. The existing precipitates coarsen to minimize the surface energy of the system through Ostwald ripening process. The coarsening of precipitates can be described semi-empirically by the equation given below [22-23]

$$(d_{p,t})^p - (d_{p,t=0})^p = K_d \cdot t \qquad (9)$$

Where $d_{p,t=0}$ is the average diameter of precipitates before loading at time $t = 0$, $d_{p,t}$ is the average precipitates diameter at time t, and p and K_d are constants depend on the type of precipitates, stress and temperature. Coarsening means an increment in the mean diameter and a decrement in the number density of precipitates.

Furthermore, new precipitates called Laves phase, form at expense of solid solution strengthening elements such as Mo and W. The precipitation of coarse Z-phase takes place at expenses of fine MX precipitates. Additionally, cavities are formed from the early stages of creep and grow with the exposure time. The synergistic effect of all these physical processes weakens the material and finally leads to failure.

Z-Phase is reported in the literature to be responsible of premature failure in these steels, since it consumes the useful fine MX precipitates from the matrix. Z-phase particles are quite large, so they do not contribute to the precipitate strengthening [11-13]. The microstructural degradation during creep is illustrated in Figure 2.

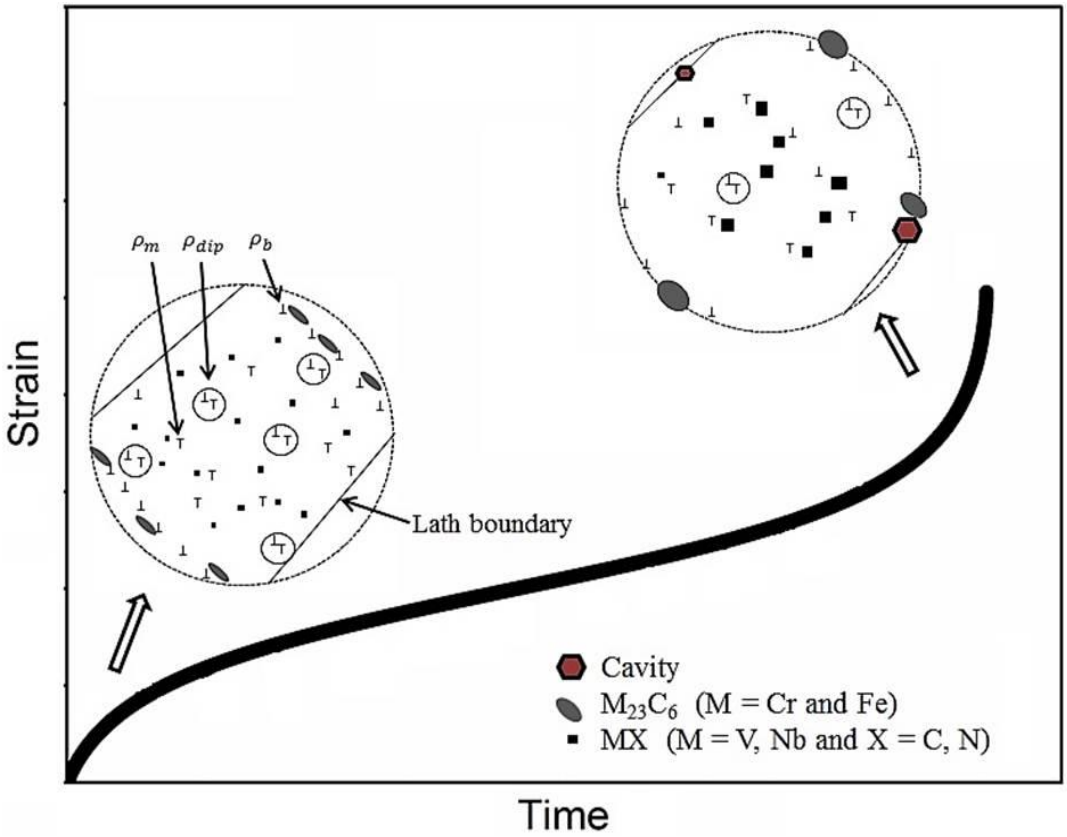

Figure 2. Schematic draw of microstructural degradation during creep

1.5 Creep strain modelling

The modelling of creep has been started long back with classical approaches [24-28]. Many models have been developed addressing the creep behaviour of martensitic/ferritic steels and they have added considerable knowledge about the creep behaviour in this field. Some of the models, physically based [21, 29-30] as well as continuum damage mechanics (CDM) approach [31] based, are briefly discussed here.

1.5.1 Ghoniem *et al.* [1990]

First comprehensive dislocation based creep model was developed by N. Ghoniem and co-workers in 1990 [21]. The model considered three types of dislocation densities such as: mobile (ρ_m), static (ρ_s) and boundary (ρ_b). The reactions between different dislocations and subgrains were considered, and the effect of precipitates was incorporated in terms of Zener drag. The creep strain rate was considered to be a function of different internal variables, and was given as:

$$\dot{\varepsilon} = f(\rho_m, \rho_s, \rho_b, R_{sub}, \sigma, T, r_m, N_v) \qquad (10)$$

where R_{sub} is the subgrain radius, σ is the applied stress, T is the temperature, r_m is the mean radius of precipitates and N_v the number density of precipitates. The model was applicable until secondary creep stage, since cavitation was not considered.

1.5.2 Barkar *et al.* [2005]

In the model of Barkar *et al.* [30] the concept of hard and soft region was used to simulate the creep curves. The material was treated as composite and creep strain rate was given as:

$$\dot{\varepsilon}_{\mathrm{tot,pl}} = (1 - f_{\mathrm{h}})\dot{\varepsilon}_{\mathrm{s,pl}} + f_{\mathrm{h}}\dot{\varepsilon}_{\mathrm{h,pl}} + \dot{f}_{\mathrm{h}}(\varepsilon_{\mathrm{h,pl}} - \varepsilon_{\mathrm{s,pl}}) \qquad (11)$$

where f_{h} is the volume fraction of hard region (cell boundary), $\dot{\varepsilon}_{\mathrm{s,pl}}$ is the local strain rate in soft region (cell interior) and $\dot{\varepsilon}_{\mathrm{h,pl}}$ the local strain rate in hard region of the material. The model was applicable up to secondary creep stage. The cavitation was not considered in the model.

1.5.3 Magnuson *et al.* [2007]

In this model [29] the creep strain rate was considered to be a function of two different dislocation densities types and the precipitation state given as:

$$\dot{\varepsilon} = f(\rho_f, \rho_{im}, \sigma, T, R_{sub}, r_m, f_p) \qquad (12)$$

where ρ_f is the free dislocation density, ρ_{im} is the immobile dislocation density and f_p the volume fraction of precipitates. The model was applicable up to secondary creep stage and cavitation damage was not considered in the model.

1.5.4 McLean *et al.* [2000]

Continuum damage mechanics (CDM) based approaches have been used extensively for the creep modelling in these materials. In the approach suggested by McLean and Dyson [31] creep strain rate was considered as function of different state variables given by:

$$\dot{\varepsilon} = \dot{\varepsilon}_0 \frac{(1+D_d)}{(1-D_s)} \sinh\left[\frac{\sigma(1-H)}{\sigma_0(1-D_p)}\right] \qquad (13)$$

where H is a parameter that accounts for stresses redistribution around the precipitates, D_p is the damage parameter for particle coarsening, D_s is the damage parameter for solid solution depletion and D_d the softening due to mobile dislocations. These parameters can be obtained from creep experiments.

1.5.5 Basirat *et al.* [2012]

In this model Basirat *et al.* [16] came up with the idea to couple the physically based model with damage parameters of the CDM approach. The creep strain rate was given as:

$$\dot{\varepsilon} = f(\rho_m, \rho_{dip}, \sigma, T, D_s, D_P, D_N) \qquad (14)$$

where ρ_{dip} is the dipole dislocation density, D_p is the damage parameter for particle coarsening, D_s is the damage parameter for solid solution depletion and D_N the softening due cavitation during creep. This model didn't include the evolution of subgrains.

The summary of the above described models is given in Table 1.

Table 1 Summary of the models

Models	Creep strain rate	Rate equations
Ghoniem *et al.* [21]	$\dot{\varepsilon} = b \cdot \rho_m \cdot v_g$	$\dot{\rho}_m = \dot{\rho}_m{}^{+} - \dot{\rho}_m{}^{-} - \dot{\rho}_s{}^{+}$ $\dot{\rho}_s = \dot{\rho}_s{}^{+} - \dot{\rho}_s{}^{-} - \dot{\rho}_b{}^{+}$ $\dot{\rho}_b = \dot{\rho}_b{}^{+} - \dot{\rho}_b{}^{-}$ $\dot{R}_{sub} = \dot{R}_{sub}{}^{+} - \dot{R}_{sub}{}^{-}$
Barkar *et al.* [30]	$\dot{\varepsilon}_{\mathrm{tot,pl}} = (1 - f_{\mathrm{h}})\dot{\varepsilon}_{\mathrm{s,pl}} + f_{\mathrm{h}}\dot{\varepsilon}_{\mathrm{h,pl}} + \dot{f}_{\mathrm{h}}(\varepsilon_{\mathrm{h,pl}} - \varepsilon_{\mathrm{s,pl}})$	$\dot{\varepsilon}_{\mathrm{s}} = f(\sigma_s, X)$ $\dot{\varepsilon}_{\mathrm{h}} = f(\sigma_h, X)$
Magnuson *et al.* [29]	$\dot{\varepsilon} = A_N \cdot \exp[-Q_c/RT][\sigma_{app} - \sigma_{back,tot}]^N$	$\dot{\rho}_f = \dot{\rho}_f{}^{+} - \dot{\rho}_f{}^{-} - \dot{\rho}_{im}{}^{+}$ $\dot{\rho}_{im} = \dot{\rho}_{im}{}^{+} - \dot{\rho}_{im}{}^{-}$ $\dot{R}_{sub} = R_{sub}{}^{+}$
Dyson *et al.* [31]	$\dot{\varepsilon} = \dot{\varepsilon}_0 \dfrac{(1 + D_d)}{(1 - D_s)} \sinh\left[\dfrac{\sigma(1 - H)}{\sigma_0(1 - D_p)}\right]$	$\dot{H} = \dfrac{h'}{\sigma}\left(1 - \dfrac{H}{H^*}\right)\dot{\varepsilon}$ $\dot{D}_d = C\dot{\varepsilon}$ $\dot{D}_p = \dfrac{k_p}{3}(1 - D_p)^4$ $\dot{D}_S = K_S D_S^{1/3}(1 - D_s)$
Basirat *et al.* [16]	$\dot{\varepsilon} = \dfrac{b \cdot \rho_m \cdot v_g}{M \cdot (1 - D_s) \cdot (1 - D_P) \cdot (1 - D_N)}$	$\dot{\rho}_m = \dot{\rho}_m{}^{+} - \dot{\rho}_m{}^{-} - \dot{\rho}_{dip}{}^{+}$ $\dot{\rho}_{dip} = \dot{\rho}_{dip}{}^{+} - \dot{\rho}_{dip}{}^{-}$

Note: Superscript ($^{+}$) on the variables in rate equations of table 1 represents production term and Superscript ($^{-}$) represents reduction term.

2. Problem formulation

In present time best creep resistant steel is P92, developed in 1980s [11]. The applicability of this steel is up to 600 °C. Continuous efforts in last decades have been made to develop new kind of steels that can be used at 650°C. Unfortunately, all these attempts were unsuccessful [11]. For further development of the new alloys in this category, the understanding of material response at high temperatures under a mechanical load as well as governing creep mechanism is necessary. In that direction, one way would be to develop a physically based model for creep on the ground of microstructural evolution. The up to date physical models based on dislocations interactions are capable to simulate creep curves only up to secondary stage. Physical based model are unable to model the creep curve up to tertiary creep stage, because tertiary creep stage depends on the synergistic effect of recovery, precipitate coarsening and cavitation and these mechanisms are not included in physical models. CDM approach can be used to couple the dislocation based physical model with softening parameters to simulate the creep curves up to the onset of tertiary stage. In this regard, the nature of cavitation damage should be known to define the softening parameter. On the other hand, physical models require the values of experimental data such as the different dislocation densities and subgrain size in as received as well as in crept conditions.

In short, some important issues to be solved are summarised below:

- The distinction between creep cavities and AlN cannot be realised using conventional techniques. Furthermore, the nature of cavities (if pre-existing or formed during creep) has not investigated thoroughly until now.
- The existing physically based creep models cannot simulate the tertiary creep. Moreover, the evolution of internal variables is not described, neither interpreted. Therefore, creep model describing tertiary creep as well addressing internal variables deeply is a need to understand the creep phenomena in detail.
- The different methods to quantify the evolution of the substructure consisting of different dislocation configurations were never systematically used to characterize all internal variables under different loading conditions. The use of each technique producing different results and their interpretations are spread all over the existing literature.

Based on the above issues described the objectives of this work are:

- To characterize and describe the nature of cavities and their evolution during creep by means of traditional microscopy, 2D stereological method, computed tomography (CT) and focused ion beam (FIB) serial sectioning [Paper I and II].
- To develop a hybrid creep model describing the creep curve up to the onset of tertiary stage coupling a dislocation based model with CDM approach, and to interpret the evolution of variables involved in the model [Paper III].

- To systematically characterize the substructure evolution in terms of different dislocation densities using a combination of techniques such as: TEM, XRD and EBSD [Paper IV].

Papers I, II, III and IV are given in Annex 1

3. Materials and methods

3.1 Materials and creep tests

P91, P92 and a newly developed 12% Cr steel ZL3 were used in this work.

P91 was supplied by RWE power AG (Germany) in the form of a pipe with a wall thickness of 21 mm and a diameter of 250 mm. The pipe was normalised at 1060 °C for 30 min followed by air cooling, tempered at 770 °C for 60 min and air cooled. To study the nature and type of cavities, specimens were machined from the pipe in as-received condition and creep loaded at 650 °C with an initial tensile stress of 60 MPa for 7000 h and 9000 h [Paper I and II].

P92 was used to validate the developed model [Paper III] for dislocation creep using data from literature [32].

The material ZL3 was produced by Saarschmiede GmbH (Germany) in form of a forged block. The heat treatment consisted of a solution treatment at 1150 °C for 1 hour, air cooling, an intermediate tempering of 6 hours at 650 °C and a final tempering of 6 hours at 740 °C. The creep specimens were loaded at 650 °C with three different initial tensile stresses of 150, 130 and 80 MPa. Creep properties and substructure evolution were studied in different conditions [Paper IV]. The chemical compositions of these alloys are given in Papers I, II, [32] and IV.

3.2 Creep testing machines

Creep tests were conducted on specimens from P91 [Paper I and II] and ZL3 [Paper IV] steels using, both interrupted [Paper I, II, and IV] and continuous [Paper IV] creep testing machines. Figure 3 shows the uniaxial interrupted creep testing machine and associated measurement devices. This machine has the ability to test up to 7 specimens with different stresses at constant load and temperature. The stresses in different specimens can be varied by changing the diameters of specimens and keeping a constant load. The maximal temperature gradient from top to bottom measured inside the creep furnace was of about ± 4 °C. Specimens were taken out at regular intervals and the elongation was measured with the help of a camera. The monitor was used to match the cross hair with specimen ridges to measure the elongation precisely.

Figure 4 shows the continuous creep testing machine. In this machine, the elongation is measured continuously using two strain gauges. In this machine, only one specimen is tested at once.

All creep tests were conducted according to EN ISO 204:2009 standard. Short term creep tests were carried out in continuous and long term creep tests in interrupted testing machines for getting enough data to produce creep curves.

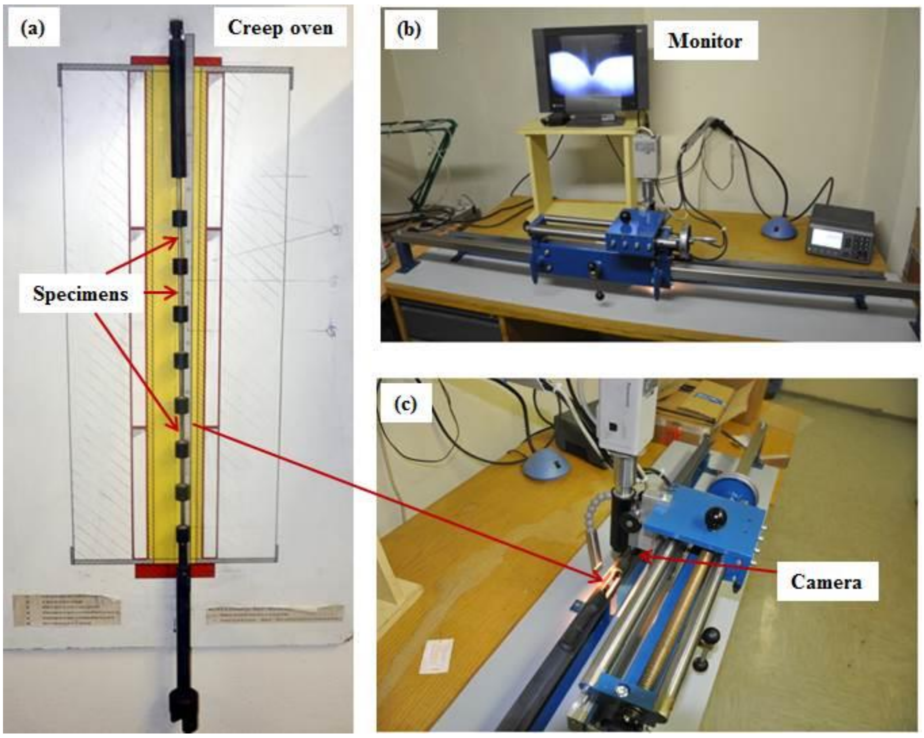

Figure 3. Open view of inturpted creep testing machine (a), length measurement using monitor (b) and camera (c)

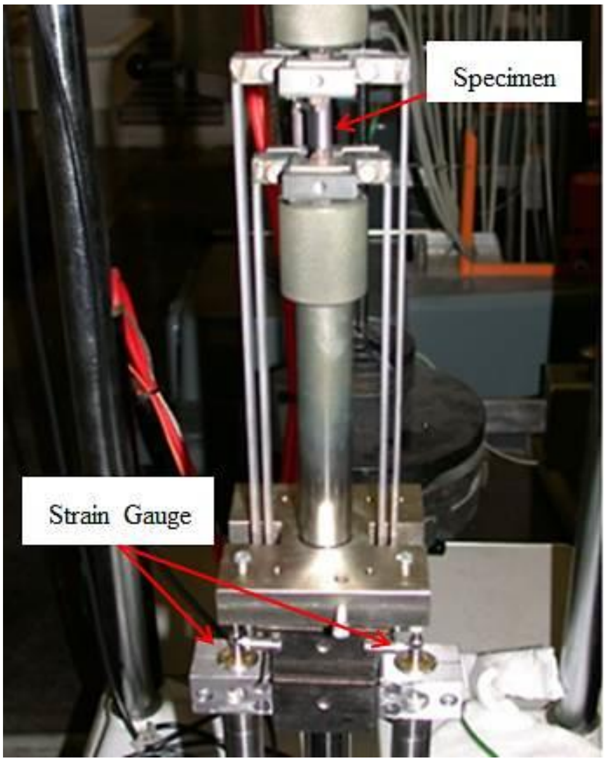

Figure 4. Continuous creep testing machine

3.3 Metallography

The specimens for microscopy were first mechanically ground with silicon carbide papers down up to P4000 grit size (European standard). After that, 1 µm diamond paste was applied for the fine polishing using a Tegrapol-31 polishing machine. Finally, a neutral OP-AN solution with 0.02 µm alumina particles was used to achieve a scratch free surface using a VIBROMET 2 vibratory polisher. Vibrational polishing with neutral solution gives the best polished surface, without modifications in cavities size [Paper I and II]. Specimens from ZL3 steel were etched with Villela's reagent to investigate the prior austenitic grain boundaries and block boundaries. Further specific specimen's preparation techniques were used for XRD, EBSD and TEM investigations as described in Paper IV.

3.3 MatCalc© simulations

The phase state of P92 was simulated using software MatCalc©, based on the chemical composition and temperature history reported in [32]. The precipitation kinetic simulations were based on Wagner-Kampmann-type model that includes (a) classical nucleation theory and (b) growth/shrinkage/coarsening/composition change based on maximum energy dissipation [33-34]. The simulation results such as mean radius and number density of precipitates after tempering were used for creep modelling [Paper III]. Information about nucleation sites, mobility and thermodynamic database used for the calculation are given in Paper III.

3.4 Creep modelling approach

The approach for modelling the dislocation creep is shown Figure 5. The set of related rate equations [Paper III] were solved simultaneously using software Matlab. The initial input parameters were taken from the literature and software MatCalc©. The output of the model was validated with the experimental data reported in literature [32].

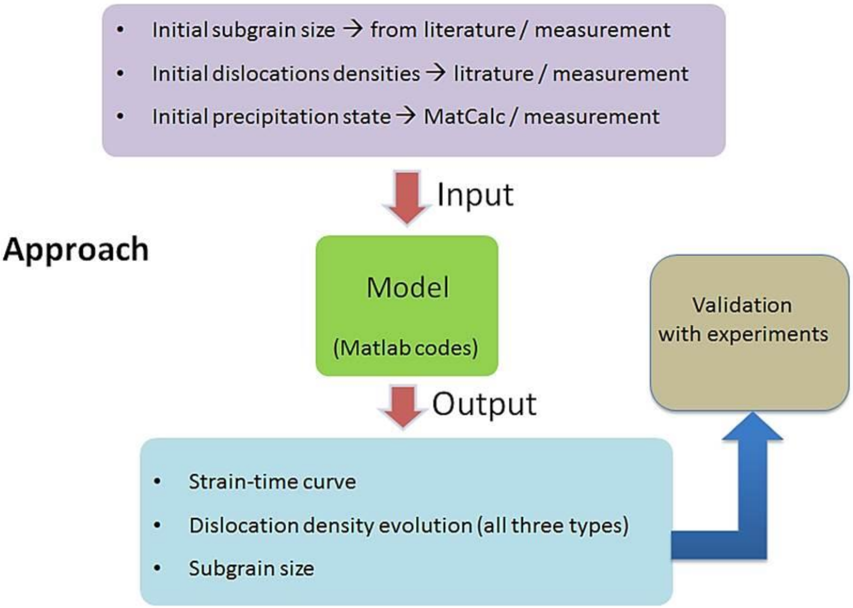

Figure 5. Schematic of modelling approach used in paper III

4. Microstructure characterization techniques

Different techniques were utilized to characterize different microstructural features and are discussed briefly below.

4.1 Light optical microscopy

ZEISS-AXIO observer.Z1m light optical microscope was used for taking the images of pre-existing pores and inclusions in Paper II (P91 steel). It was used also to reveal the prior austenitic grain boundaries and block boundaries in Paper IV (ZL3 steel).

4.2 Electron microscopy

4.2.1 Scanning electron microscopy (SEM)

LEO-SEM conventional scanning electron microscope in back scattered electron (BSE) mode was used to characterize the pre-existing pores in Paper I and II (P91 steel). In combination with BSE mode, energy dispersive x-ray analysis (EDX) system was used to investigate Laves phase and $M_{23}C_6$ precipitates in Paper IV (ZL3 steel).

4.2.2 Focused ion beam and field emission gun SEM (FIB-FEG SEM)

FIB-serial sectioning was employed to reveal the small creep cavities in Paper II (P91 steel). A dual beam set up with focused ion beam (FIB) column and field emission gun (FEG) column was used. FIB was used to cut the slices (Figure 6a) and the milled surface was scanned using secondary electrons (Figure 6b). Figure 6c shows an example of the FEG-SEM image of the cross section after slicing the material. 425 slices were milled and the cross sections were imaged using an in-lens detector. For the quantification 3D reconstruction of creep cavities was obtained using Avizo software.

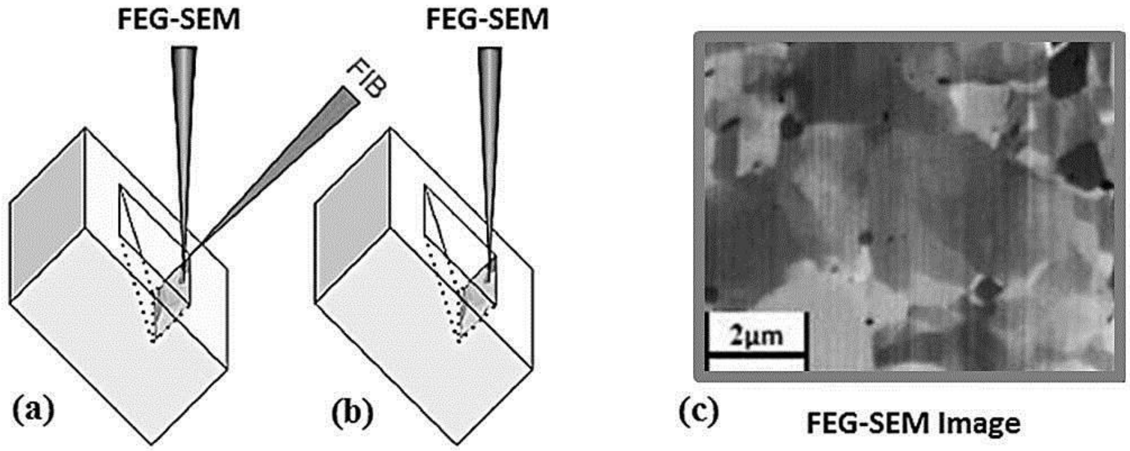

Figure 6. Illustration of FIB-FEG SEM serial sectioning, slicing by FIB (a), Imaging by FEG-SEM (b), FEG-SEM image (in-lens) of cross section (c)

4.2.3 Electron back scatter diffraction (EBSD)

EBSD measurements were carried out on a FEI Quanta 3D FEG-SEM equipped with EDAX [Paper IV, ZL3 steel]. The area of scanning was 60 × 60 μm^2 having a step size of 0.15 µm.

Software TSL OIM™ 7 was employed to analyse the EBSD data. Orientation maps and grain boundary maps were generated accordingly. Mean subgrain size, misorientation angle and amount of low angle grain boundaries were obtained from these measurements.

4.2.4 Transmission electron microscopy (TEM)

TEM was used for imaging dislocations inside the subgrains, i.e. mobile and dipoles [Paper IV, ZL3 steel]. TEM specimens were analysed employing microscopes JEOL 200CX operating at 200 kV and Philips CM 300 operating at 300 kV.

4.3 Computed tomography (CT)

A GE *nanotom m* was used for the investigation of pre-existing pores [Paper I, P91 steel]. Many radiographic images (Figure 7a) were generated and they were stacked together (Figure 7b) using mathematical algorithm for constructing 3D views (Figure 7c). Details of the measurement parameters can be found in [Paper I].

Figure 7. Schematic of CT and 3D reconstruction, radiographic image (a), stacking of all radiographic images (b), 3D reconstruction of pore (c) [35]

4.4 X-Ray diffraction

X-ray line profile analysis was applied to characterize the mobile dislocation density inside the subgrains, as explained in detail in Paper IV. Mobile dislocations are the ones mostly contributing to lattice microstrain and hence, responsible for broadening the peak. The stress fields of other dislocations type, i.e. dipole and boundary are relatively low in comparison to mobile dislocations, and hence, their effect in peak broadening was neglected.

5. Results

5.1 Cavitation in P91 [Paper I and II]

Two types of cavities/pores were detected in the P91 steel: the pre-exiting ones and the others formed during creep. Pre-existing pores were found in the as-received condition. SEM investigation revealed that their size range was between 1-6 µm before creep. During the creep at 60 MPa/650 °C, new creep cavities were formed. FIB serial sectioning and 3D reconstruction revealed that the size of creep cavities was between 0.1 to 0.6 µm in a given condition. The creep cavities were nucleated at high angle grain boundaries (HAGB) and besides coarse precipitates along HAGBs.

The circularity of pre-existing pores was decreased from 0.86 to 0.62 after creep. From the stereological calculations, it was found that the number density of these pores decreased with ongoing creep while nearest neighbours distance increased due to the agglomeration of pores. Additionally, the mean diameter and volume fraction of pre-existing pores were increased after creep exposure. All these modifications in morphology, amount and volume fraction were related to growth and agglomeration of pre-existing pores. 3D rendered data set from computed tomography (CT) measurements confirmed the agglomeration of pre-existing pores during creep. Unfortunately and due to the high density of P91 steel, scattered radiation created blurred edges in CT data set. Thus, quantification of pores using CT methodology was not possible. The growth of pre-existing pores was explained and modelled based on the chemical potential of vacancies. The developed physically based model was based on migration of vacancies towards the pores, since pores acted like sinks for vacancies.

Comparing the volume fraction of creep cavities obtained from 2D stereology and 3D FIB serial sectioning, it was revealed that stereological calculation overestimated the volume fraction. In any case, stereological calculations were used to calculate and compare the volume fraction of the two types of pores (pre-existing pores and creep pores), and the results showed that the volume fraction of pre-existing pores was nearly 12 times higher than the volume fraction of creep cavities.

5.2 Precipitation state simulation of P92 steel [Paper III]

The simulation of the precipitation state during heat treatment was performed using MatCalc© according to the material history reported in [32], see Figure 8a. The precipitates considered in the simulation were $M_{23}C_6$ (M = Cr and Fe), $MX_{Austenite}$ in austenitic matrix and $MX_{Martensite}$ (M = V, Nb and X = C, N) in martensitic matrix. Figures 8b, c and d depict the evolution during the heat treatment of number density, mean radius, and phase fraction of the considered precipitates, respectively. All three precipitates $M_{23}C_6$, $MX_{Austenite}$ and $MX_{Martensite}$ were growing during the heating up to normalizing temperature. Once normalizing temperature was achieved, during the holding time, $M_{23}C_6$ carbides were dissolved while $MX_{Austenite}$ precipitates continued to grow. Significant change was not observed in $MX_{Martensite}$ precipitates during normalizing. Further, at tempering stage both MX types of precipitates started to grow slightly and $M_{23}C_6$ carbides precipitates form and coarsen. It was observed that the precipitates number density, mean radius and phase fraction reached nearly constant values in the end of the tempering stage (see Figures 8b, 8c and 8d at 10.4 hours).

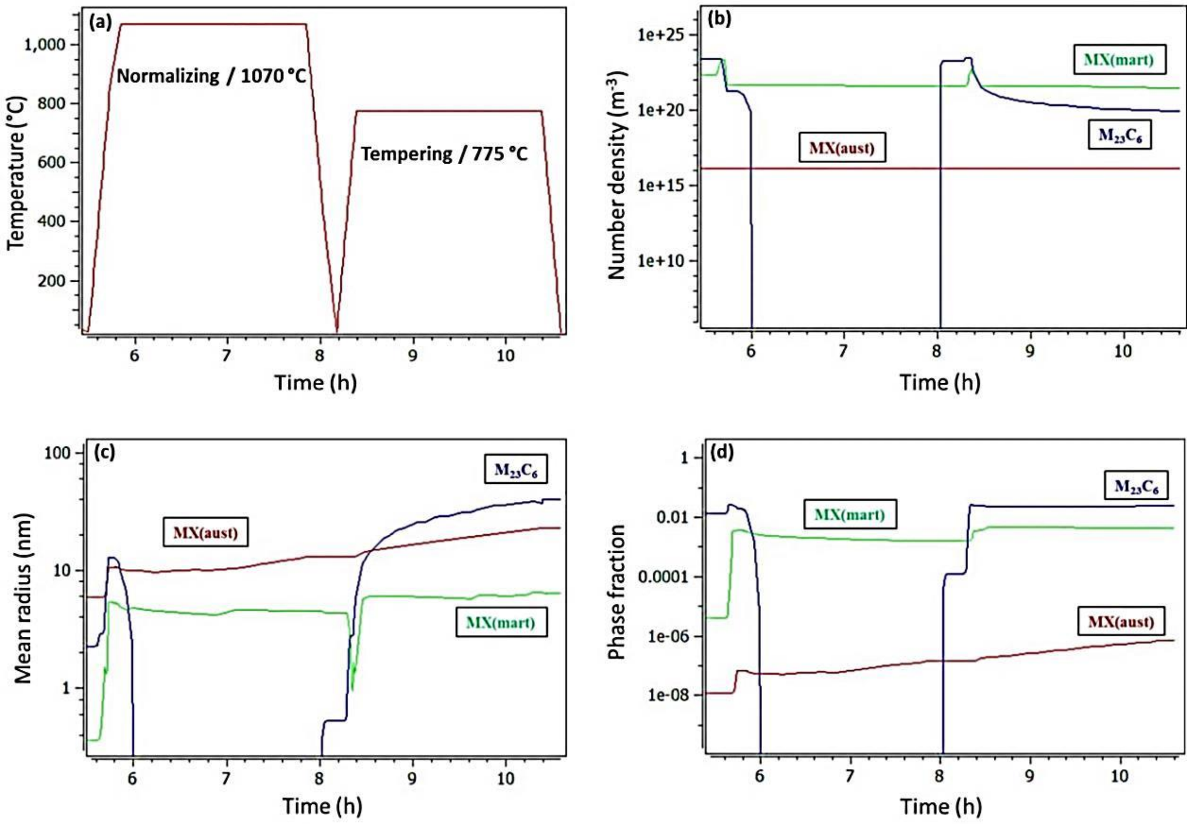

Figure 8 Simulation of the precipitation state during the heat treatment using MatCalc©, temperature cycle (a), number density (b), mean radius (c) and phase fraction (d)

The phase fraction of $M_{23}C_6$, $MX_{\text{Martensite}}$ and $MX_{\text{Austenite}}$ after the tempering was found to be 2.5×10^{-2}, 4.21×10^{-3} and 6.9×10^{-7}, respectively. The results from the simulation i.e. mean radius and number density were used as input parameters for the numerical simulation of the Zener drag pressure (see equation (7) of Paper III).

5.3 Creep modelling of a traditional Cr-steel [Paper III]

Creep curves of grade P92 steel extracted from [32] were modelled up to the onset of tertiary creep stage using a hybrid model. In this approach, a physical model based on dislocation interactions and subgrain evolution was developed and coupled with CDM approach. A detailed description of the model is given in [Paper III]. The results of the model showed good agreement with the experimental data. The model was validated in terms of experimental creep curves, mobile dislocation density and subgrain size.

The initial value of the mobile dislocation density was high and decreased with ongoing creep due to spontaneous annihilation and creation of new dipoles. By further creep, the formed dipoles were annihilated as well as transformed to boundary dislocations. Therefore, boundary dislocation density increased in the beginning of the creep exposure due to the transformation of dipoles into boundary dislocations. By increasing the strain, the boundary dislocation density decreased due to the subgrain growth. The main model results can be summarized as follows:

- All three dislocation densities (mobile, dipole and boundary), effective stress on dislocations, internal stress and glide velocity reached nearly steady values after the primary creep.
- The recovery rate was high at the beginning of creep and decreased with the exposure time.
- The internal stress was large at the beginning and decreased with ongoing creep.
- Effective stress increased at the beginning of creep and achieved a steady state value. The glide velocity followed a similar behaviour like effective stress.
- The effective stress and the glide velocity increased with increasing the applied stress levels.

The model predicted higher mobile dislocation density and smaller subgrain size at higher stresses. All results were in agreement with empirical relationships between applied stress and mobile dislocation density, as well as between applied stress and subgrain size [22, 36-37]. The growth rate of subgrains at higher stresses was found to be high due to larger creep rate. However, due to the early failures at higher stresses and short creep times, subgrain sizes of broken samples were smaller than those of samples fractured at low stresses.

5.4 Substructure evolution during creep of a novel Cr-steel [Paper IV]

The novel 12% Cr steel named ZL3 had a martensitic/ferritic structure after processing and presented different type of boundaries, such as: PAGBs, packet, block and lath boundaries. PAGBs were decorated with $M_{23}C_6$ and Laves phase particles identified with EDX analysis. Norton's exponent from the creep law was found to be 4.08, suggesting dislocation creep in the testing regime of 80-150 MPa/650 °C.

All experimental measurements showed that lattice microstrain and all three dislocation densities decreased after creep. The main results are summarized as follows:

- The dislocation density inside subgrains (dipole + mobile) was decreased in one order of magnitude after creep at 80 MPa/650 °C.
- The annihilation rate was larger for dipoles than for mobile dislocations.
- Polygonized subgrains were found after the creep exposure.
- After almost 6000 hours of creep loading at 80 MPa/650 °C, the total dislocation density decreased 4.5 times and the subgrain size increased 3 times.
- The estimated glide velocity was 4.15×10^{-15} m/s at 130 MPa/650 °C.

6. Discussion

The discussion chapter analyses the impact of the here obtained results in the advance of the existing knowledge of this research field.

6.1 Cavities and their characterization

The nature of cavities, their identification and quantification are essential to describe and predict creep rupture. Therefore, some main points are discussed here.

A detailed study on crept P91 with the latest technologies proved, contrary to what was reported in the literature, that not all the entities producing black contrast in BSE mode of SEM investigations are creep cavities. In earlier studies, straight conclusions on pore densities have been drawn using only the dark black contrast [15]. In our work we have shown that, precipitates having elements with low atomic weight, as for example AlN in P91 will show dark black contrast under application of high voltage in back scattered electron (BSE) mode.

Usually, creep cavities are nucleated at grain boundaries or in the vicinity of big particles along grain boundaries [15]. Therefore, the identification and quantification of cavities nucleated at $M_{23}C_6$ particles (placed at the grain boundaries) becomes complex. This can be explained as follows: since the steel contains Al and N, the precipitation of AlN takes place during creep exposure, and this precipitation occurs in the vicinity of $M_{23}C_6$ [38]. Thus, it is hard to differentiate the cavities from AlN particles, both nucleated around $M_{23}C_6$. Novel developments in the scanning electron microscopy allowed us to distinguish between AlN and pores. In this way, FEG-SEM equipped with In-lens detector proved to be one solution of this problem. In-lens detector allows highly efficient collections of secondary electrons (SE) inside the column at very low voltages. Since secondary electrons are good for imaging surface topography, the edges of cavities appeared brighter in the images due to the production of more electrons [Paper II]. In contrast, AlN did not show any topography effect.

The cavities formed in P91 during creep were rather small in comparison to a second population i.e. pre-existing pores due to the fact that all vacancies were not available for contributing to the growth of creep cavities [Paper I and II]. Pre-existing pores have not been reported in the literature before, although unidentified entities can be seen in Figure 9 from the literature [15]. The marked entities in Figure 9 looked like pores or inclusions, although no conclusions can be made, since there is not any comment about them in the original paper.

The pre-existing pores grow during creep by reducing the chemical potential of vacancies in their respective regions of material. The big pores act like sink for the vacancies and therefore vacancies migrate towards pores. Besides of the vacancies that participated in the growth of pre-existing pores, the total vacancy concentration was still enough to create new creep cavities. In our work we characterized the morphology [39] of creep cavities as well, and found that they have a flake type shape.

In our studied case, the volume fraction of pre-existing pores after creep was twelve times higher than the volume fraction of creep pores. This indicates that if pre-existing defects exist in the material, they will be more detrimental with respect to failure than the cavities formed during creep.

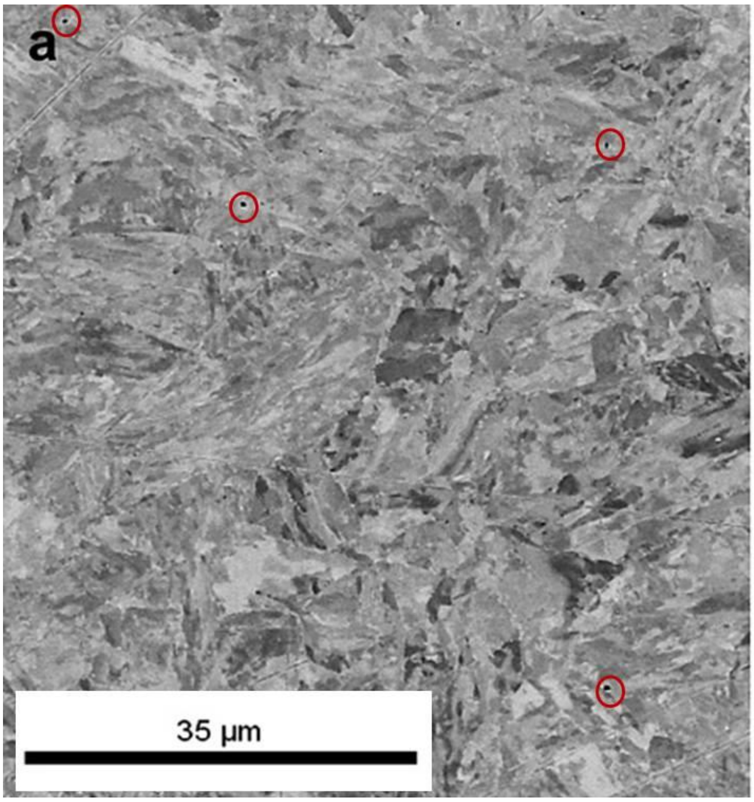

Figure 9 Pre-existing defects marked with red circles in as-received P91 [15]

Since 3D characterization techniques are time consuming, stereological methods may be used to obtain the 3D information from 2D measurements. In the case of pores, this information can be size, volume fraction, and number density. The usual assumptions done to transform 2D information into 3D information are: pores have spherical shape and the pores are distributed homogeneously throughout the material [Paper II]. With these assumptions, the volume fraction of flakes type creep cavities calculated using 2D stereology was nearly four times higher than the actual volume fraction obtained from FIB serial sectioning [Paper II]. Therefore, 3D characterization techniques are recommended when accurate quantification, 3D morphological and interconnectivity information is required. A comparison is shown between 2D stereological method and 3D FIB serial sectioning in Table 2.

Table 2 Comparison of 2D stereological method vs. 3D FIB serial sectioning

Technique	Advantage	Disadvantage
2D Stereology	Cheap and easy to apply	Less accurate due to number of assumptions
3D FIB serial sectioning	Accurate quantification and useful for morphological and interconnectivity characterization	Expensive, trained personal required and time consuming

6.2 Creep modelling

The hybrid creep model presented in [Paper III] is complete in the sense that it considers the microstructural evolution as well as damage. Models based on purely dislocations interactions are not capable to simulate tertiary creep [30, 40]. Figure 10 shows the example of creep curves obtained from dislocation model that can only simulate the curves up to secondary stage [40]

Tertiary creep is governed by the collective effect of recovery, precipitate coarsening and cavitation. The cavitation investigations carried out on P91 [Paper I and II] allowed us to develop a semi-empiric softening parameter to couple the physically based dislocation model with the CDM approach. The advantage of this hybrid approach is that the model not only reproduces the creep curves, but also provides microstructural and internal information such as evolution of dislocation densities and subgrain size. The model is suitable to simulate the creep curve up to onset of tertiary stage [Paper III]. After the onset of tertiary stage the remaining life is only about approximately 20% of the total life, thus it is sufficient if the onset of tertiary creep stage is modelled [41]. The model should take into account the necking occurring just before fracture where triaxial stresses occur. This is not the case in the present version of the here developed model. Finally it must be noted that the present model can be used for 9-12% Cr steels.

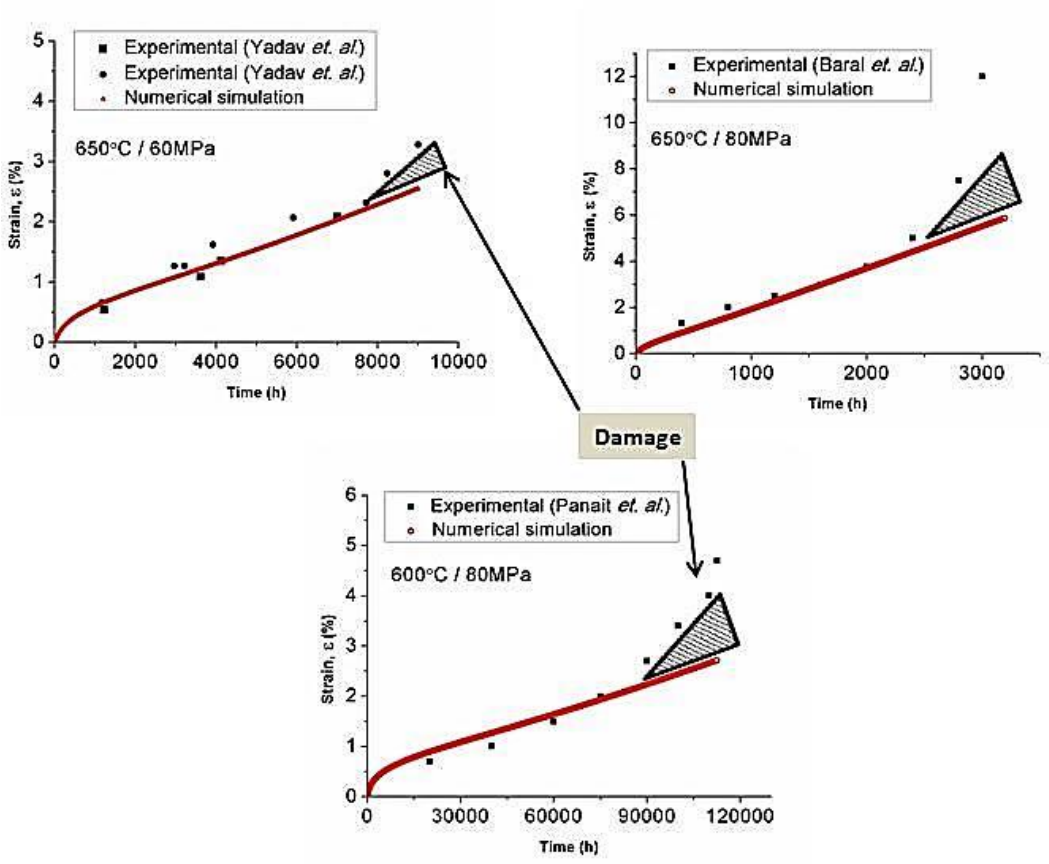

Figure 10 Creep curves of P91, simulation (full line) vs. experimental results (squared symbols). Model cannot reproduce tertiary creep [40]

When materials are creep loaded the mobile and dipole dislocation densities decrease with the exposure time. The boundary dislocation increases in the beginning and decreases with the exposure time after primary creep due to subgrain growth [Paper III]. It was found that recovery of dipole dislocations is faster than recovery of mobile dislocations [Paper IV].

The model suggests that if we ignore the interaction between fine MX precipitates and dislocations inside the subgrains then recovery rate is high, see Figure 8 of Paper III. In the same way if we remove the $M_{23}C_6$ carbides from the subgrain boundaries the subgrain coarsening will be high, see equation (7) of Paper III. This indirectly indicates that, steels developed with thermodynamically stable precipitates will be more resistant against creep for longer time.

6.3 Microstructure evolution

In general, the microstructure of any material depends on the processing history. In particular, 9-12% Cr steels power plant components are first normalized followed by tempering steps to obtain a so called “as-received condition”. Under this condition, the material is used in service for power plant applications [16, 32, Paper IV]. When these steels are normalized and quenched, the developed microstructure contains a very large amount of dislocations within the laths (Figure 11a) due to the martensitic transformation [42].

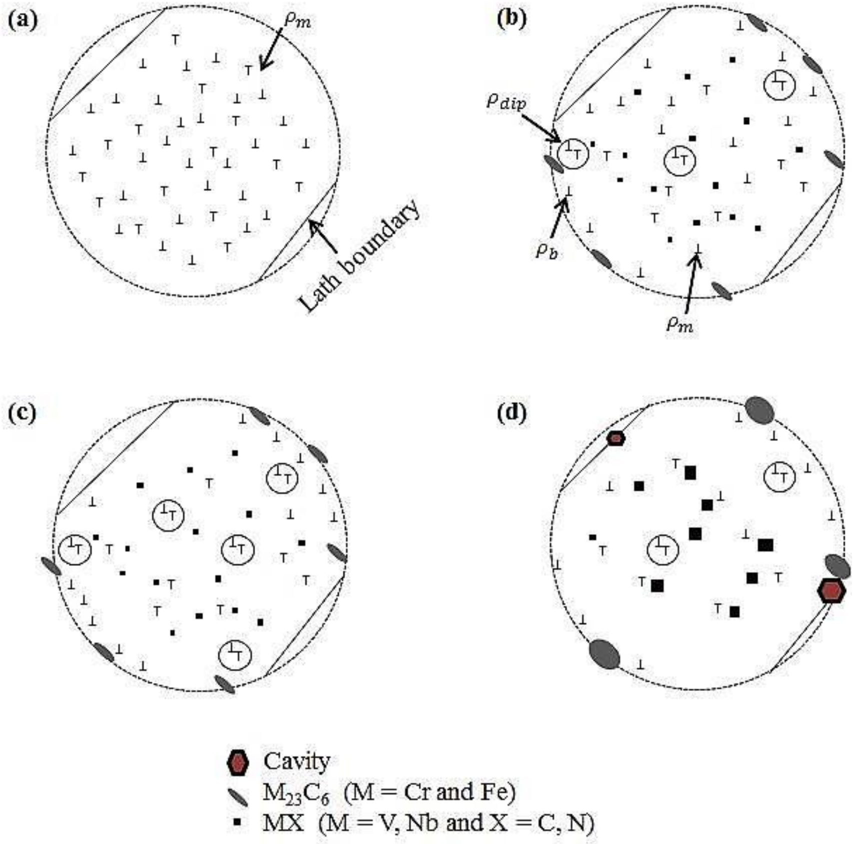

Figure 11 Layout of the substructure evolution of 9-12% Cr steels in different conditions, quenching (a), after tempering for time t_1 (b), after tempering for time $t_2 > t_1$ (c), after long term creep (d)

The dislocation density is in the order of 10^{16} m^{-2} within laths. Kurdjumov and Sachs (K–S) transformation [43], induces the formation of high number of mobile dislocations inside the martensitic laths [44] due to shear deformation. During the tempering stage, the density of mobile dislocations decreases due to climb recovery, dipoles as well as subgrains form and strengthening particles ($M_{23}C_6$) precipitate (Figure 11b). In the case of X20, a 12% Cr steel, it was found that the dislocation density was 9.3×10^{14} m^{-2} after normalizing, and that it went down to 1×10^{14} m^{-2} after 1 h tempering [45]. The density of different dislocation classes depends on the tempering time of the as received material. The longer the tempering time applied, the more mobile dislocation will be annihilated and transformed to dipole dislocations (Figure 11c) [Paper IV]. The dipole dislocations were found to be almost in equal to the amount of mobile dislocations (~1×10^{14} m^{-2}) in the as-received ZL3 steel due to the long (6 hours) two step tempering process [Paper IV]. On the other hand, in a 9% Cr steel it was reported that the density of dipoles is 10 times less than the density of mobile dislocations in as-received condition, where tempering time was only 43 minutes [16].

6.4 Characterization of substructure

The characterization of the substructure is an important issue for modelling creep as well as for predicting mechanical properties of materials [Paper I, II and III]. TEM, XRD and EBSD are the most applied techniques for substructure characterization in case of 9-12% Cr steels [45-46]. Each of them has limitations that allow characterizing only some part of the substructure (see Figure 12).

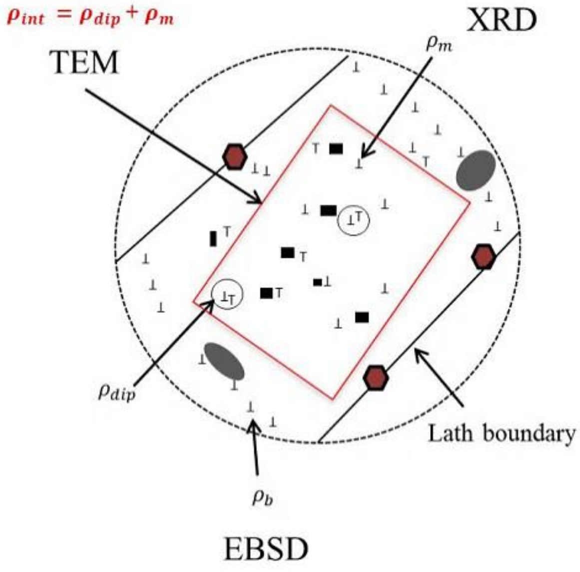

Figure 12 Draw showing the applicability of different characterization techniques

TEM can be used for the characterization of dislocations (mobile + dipole) inside the subgrains of small areas. XRD can be applied to large area of material to characterize the mobile dislocations, assuming dipole and boundary dislocations have negligible influence on peak broadening, and assuming a homogeneous distribution of dislocations. Boundary dislocation density can be evaluated from EBSD measurements. We suggested one possible way to quantify the dipole dislocations using XRD and TEM together. Subtracting the XRD result (mobile) from the TEM result (mobile + dipole), dipoles can be quantified [Paper IV]. All three techniques (TEM, XRD and EBSD) have to be applied together in order to distinguish and quantify mobile, dipole and boundary dislocations. However, total dislocation density can be quantified using TEM (mobile + dipole) and EBSD (boundary). Applying all three techniques together a complete description of the substructure and its evolution can be realised. The different techniques and related assumptions used to characterize the particular class of dislocation are summarized in Table 3.

Table 3 Type of dislocations and applicability of different characterization techniques

Techniques	Dislocations	Physical nature	Assumptions / limitation
XRD	ρ_m	Individual mobile dislocations inside subgrains	Broadening due to the boundary and dipole dislocations is negligible
EBSD	ρ_b	Boundary dislocations those are configured in low energy state	Grains having 1-4° misorientation were only considered as subgrains
TEM - XRD	$\rho_{dip} = \rho_{int} - \rho_m$	Dipole dislocations having strain field about 30% of mobile dislocations	Dipoles close to subgrain boundary were neglected
TEM	$\rho_{int} = \rho_m + \rho_{dip}$	Individual mobile and dipole dislocations inside the subgrains	Measurement area was selected inside the subgrain
TEM + EBSD	$\rho_{tot} = \rho_m + \rho_b + \rho_{dip}$	Total dislocations inside the microstructure	Assumption for TEM and EBSD applied

7. Conclusions

From this work, the following conclusions can be drawn:

1. If pre-existing pores exist in the as received material they will decrease the creep resistance of the component.
2. Complex flake type creep cavities can be characterized using In-lens detector and distinguish them from AlN. They nucleate along the high angle grain boundaries (HAGBs), as well as in the vicinity of precipitates those are at HAGBs.
3. The overestimation of the number density and volume fraction of creep cavities using the stereological method is attributed to the actual complex shape of cavities.
4. The developed hybrid creep model is capable to model the creep curve up to the onset of tertiary stage, as well as to determine the evolution of internal variables. In general:

  - Mobile and dipole dislocation density decreases and subgrains coarsen during creep.
  - Boundary dislocation density increases at the beginning of creep due to formation of subgrains, and decreases afterwards due to subgrain growth.
5. Creep model predicts that:
  - The recovery rate is high at the beginning of creep and slows down with time.
  - With ongoing creep, material becomes softer and effective stress and glide velocity increases up reaching near steady state.
  - The effective stress and the glide velocity increases with increasing the applied stress levels.
  - The higher applied stress, the faster growth rate of subgrains. However, due to the early failures at higher stresses, subgrain sizes are smaller in the broken samples compared to broken specimens tested at low stresses.
6. TEM, XRD and EBSD must be applied together for the complete characterization and quantification of the different dislocation densities.
7. TEM and EBSD together are necessary to measure the total dislocation density in the materials.
8. Dipole dislocation density can be measured applying XRD and TEM together.

8. References

1. J. Hald: Microstructure and long-term creep properties of 9-12% Cr steels, International Journal of Pressure Vessels and Piping, 85, (2008), 30-37
2. Z. Ye, P. Wang, D. Li, Y. Zhang and Y. Li: Effect of carbon and niobium on the microstructure and impact toughness of a high silicon 12% Cr ferritic/martensitic heat resistant steel, Materials Science and Engineering A, 616, (2014), 12-19
3. A. Chatterjee, D. Chakrabarti, A. Moitra, R. Mitra and A. K. Bhaduri: Effect of deformation temperature on the ductile-brittle transition behavior of a modified 9Cr–1Mo steel, Materials Science and Engineering A, 630, (2015), 58-70
4. N. Dudova, A. Plotnikova, D. Molodov, A. Belyakov and R. Kaibyshev: Structural changes of tempered martensitic 9%Cr-2%W-3%Co steel during creep at 650 °C, Materials Science and Engineering A, 534, (2012), 632-639

5. S. S. Wang, L. Chang, L. Wang, T. Wang, Y. D. Wu, J. J. Si, J. Zhu, M. X. Zhang and X. D. Hui: Microstructural stability and short-term creep properties of 12Cr-W-Mo-Co steel, Materials Science and Engineering A, 622, (2015), 204-211
6. A. Kipelova, A. Belyakov and R. Kaibyshev: Laves phase evolution in a modified P911 heat resistant steel during creep at 923 K, Materials Science and Engineering A, 532, (2012), 71-77
7. Z. Cong and Y. Murata: Dislocation density of lath martensite in 10Cr-5W Heat-resistant steels, Materials Transactions, 52 (12), (2011), 2151-2154
8. K. Sawada, M. Takeda, K. Maruyama, R. Ishii, M. Yamada, Y. Nagae and R. Komine: Effect of W on recovery of lath structure during creep of high chromium martensitic steels, Materials Science and Engineering A, 267 (1), (1999), 19-25
9. Y. Xu, X. Zhang, Y. Tian, C. Chen, Y. Nan, H. He and M. Wang: Study on the nucleation and growth of $M_{23}C_6$ carbides in a 10% Cr martensite ferritic steel after long-term aging, Materials Characterization, 111, (2016), 122-127
10. B. Sonderegger, S. Mitsche and H. Cerjak: Martensite laths in creep resistant martensitic 9-12% Cr steels - Calculation and measurement of misorientations, Materials Characterization, 58, (2007), 874-882
11. H. K. Danielsen: Review of Z phase precipitation in 9–12 wt-%Cr steels, Materials Science and Technology, 32(2) , (2016), 126-137
12. H. K. Danielsen and J. Hald: Behaviour of Z phase in 9-12% Cr steels, Energy Materials, 1, (2006), 49-57
13. H. K. Danielsen, P. E. D. Nunzio, and J. Hald: Kinetics of Z-phase precipitation in 9-12% Cr steels, Metallurgical and Materials Transactions A, 44A, (2013), 2445-2452
14. F. Masuyama: Materials for advanced power engineering, Forschungszentrum Jülich GmbH, Jülich, Germany, 53, (2006), 175-187
15. C. G. Panait, W. Bendick, A. Fuchsmann, A. F.Gourgues-Lorenzon and J. Besson: Study of the microstructure of the Grade 91 steel after more than 100,000h of creep exposure at 600 °C, International Journal of Pressure Vessels and Piping, 87, (2010), 326-335

16. M. Basirat, T. Shrestha, G. P. Potirniche, I. Charit and K. Rink: A study of the creep behavior of modified 9Cr-1Mo steel using continuum-damage modelling, International Journal of Plasticity, 37, (2012), 95-107
17. I. Holzer: Modelling and Simulation of Strengthening in Complex Martensitic 9-12% Cr Steel and a Binary Fe-Cu Alloy, PhD thesis, Graz University of Technology, Austria, (2010)
18. R. L Fleischer: Substitutional solution hardening, Acta Metallurgica, 11(3), (1963), 203-209
19. L. A. Gypen and A. Deruyttere: The combination of atomic size and elastic modulus misfit interactions in solid solution hardening, Scripta Metallurgica, 15 (8), (1981), 815-820
20. Creep-resistant steels, Woodhead Publishing and Maney Publishing, Edited by: Fujio Abe, Torsten-Ulf Kern and R. Viswanathan, (2008), 279-304
21. N. Ghoniem, J. Matthews and R. Amodeo: A dislocation model for creep in engineering materials, Res Mechanica, 29, (1990), 197-219
22. K. Maruyama, K. Sawada and J. Koike: Strengthening mechanisms of creep resistant tempered martensitic steel, ISIJ International, 41(6), (2001), 641-653
23. Y. Kadoya, N. Nishimura, B. F. Dyson and M. McLean: Origins of tertiary creep in high chromium steels, Creep & Fracture of Engineering Materials & Structures, J. C. Earthman and F. A. Mohamed, eds., TMS, War-rendale, USA, (1997), 343-352
24. M. E. Kassner and M. T. Pérez-Prado: Five-power-law creep in single phase metals and alloys, Progress in Materials Science, Volume 45 (1), (2000), 1-102
25. T. G. Langdon: Grain boundary sliding revisited: Developments in sliding over four decades, Journal of Materials Science, 41 (3), (2006), 597-609
26. F. R. N. Nabarro: Strength on solids, Physical Society, London, England, 1948
27. C. Herring: Diffusional viscoyity of a polycrystalline solid, Journal of Applied Physics, 21 (5), (1950), 437-445
28. R. L. Coble: A Model for boundary diffusion controlled creep in polycrystalline materials, Journal of Applied Physics, (1963), 34, 1679-1682
29. H. Magnusson and R. Sandström: Creep strain modeling of 9 to 12 pct Cr steels based on microstructure evolution, Metallurgical and Materials Transactions A, 38A, (2007), 2033-2039

30. T. Barkar and J. Ågren: Creep simulation of 9-12% Cr steels using the composite model with thermodynamically calculated input, Materials Science and Engineering A, 395, (2005), 110-115
31. M. McLean and B. F. Dyson: Modeling the effects of damage and microstructural evolution on the creep behavior of engineering alloys, Journal of Engineering Materials and Technology, 122, (2000), 273-278
32. P. J. Ennis, A. Zielinska-Lipiec, O. Wachter and A. Czyrska-Filemonowicz: Microstructural stability and creep rupture strength of the martensitic steel P92 for advanced power plant, Acta Materialia, 45(12), (1997), 4901-4907
33. B. S. Srinivas Prasad, V. B. Rajkumar and K. C. Hari Kumar: Numerical simulation of precipitate evolution in ferritic-martensitic power plant steels, Calphad, 36, (2012), 1-7
34. E. Kozeschnik, J. Svoboda, P. Fratzl and F. D. Fischer: Modelling of kinetics in multi-component multi-phase systems with spherical precipitates: II: Numerical solution and application, Materials Science and Engineering A, 385, (2004), 157-165
35. G. Nicoletto, R. Konečná and S. Fintova: Characterization of microshrinkage casting defects of Al–Si alloys by X-ray computed tomography and metallography, International Journal of Fatigue, 41, (2012), 39-46
36. B. Sonderegger, S. Mitsche and H. Cerjak: Microstructural analysis on a creep resistant martensitic 9-12% Cr steel using the EBSD method, Materials Science and Engineering A, 481-482, (2008), 466-470
37. A. Orlova, J. Bursik, K. Kucharova and V. Sklenicka: Microstructural development during high temperature creep of 9% Cr steel, Materials Science and Engineering A, 245, (1998), 39-48
38. H. Naoi, M. Ohgami, X. Kiu and T. Fujita: Effect of aluminum content on the mechanical properties of a 9Cr-0.5Mo-1.8W steel, Metallurgical and Materials Transactions A, 28A, (1997), 1195-1203
39. C. Gupta, H. Toda, C. Schlacher, Y. Adachi, P. Mayr, C. Sommitsch, K. Uesugi, Y. Suzuki, A. Takeuchi and M. Kobayashi: Study of creep cavitation behavior in tempered martensitic steel using synchrotron micro-tomography and serial sectioning techniques, Materials Science and Engineering A, 564, (2013), 525-538

40. S. D. Yadav, M. Schuler, C. Sommitsch and C. Poletti: Physical based creep strain modelling of 9Cr martensitic steel, Proceedings ECCC, Rome, Italy, (2014)
41. V. Sklenička, K. Kuchařová, M. Svoboda, L. Kloc, J. Buršík and A. Kroupa: Long-term creep behavior of 9-12%Cr power plant steels, Materials Characterization, 51, (2003), 35-48
42. F. R. N. Nabarro: Dislocations in Solids, Volume 7, Elsevier Science Publishers B. V., (1986), 297-403
43. B. Sonderegger, S. Mitsche and H. Cerjak: Martensite laths in creep resistant martensitic 9-12% Cr steels - Calculation and measurement of misorientations, Materials Characterization, 58, (2007), 874-882
44. S. Takebayashi, T. Kunieda, N. Yoshinaga, K. Ushioda and S. Ogata: Comparison of the dislocation density in martensitic steels evaluated by some X-ray diffraction methods, ISIJ International, 50(6), (2010), 875-882
45. J. Pesicka, A. Dronhofer and G. Eggeler: Free dislocations and boundary dislocations in tempered martensite ferritic steels, Materials Science and Engineering A, 387-389 (2004), 176-180
46. J. Pešička, R. Kužel, A. Dronhofer and G. Eggeler: The evolution of dislocation density during heat treatment and creep of tempered martensite ferritic steels, Acta Materialia, 51, (2003), 4847-4862

Annex 1: Research papers compiled for the thesis

[I] **S. D. Yadav**, J. Rosc, B. Sartory, R. Brunner, B. Sonderegger, C. Sommitsch, and C. Poletti: Investigation of Pre-Existing Pores in Creep Loaded 9Cr Steel, in 2nd International Congress on 3D Materials Science, (eds D. Bernard, J.-Y. Buffière, T. Pollock, H. F. Poulsen, A. Rollett and M. Uchic), John Wiley and Sons, Inc., Hoboken, NJ, USA, (2014), doi: 10.1002/9781118990278.ch14

[II] **S. D. Yadav**, B. Sonderegger, B. Sartory, C. Sommitsch and C. Poletti: Characterisation and quantification of cavities in 9Cr martensitic steel for power plants, Materials Science and Technology, 31(5), (2015), 554-564

[III] **S. D. Yadav**, B. Sonderegger, M. Stracey and C. Poletti: Modelling the creep behaviour of tempered martensitic steel based on a hybrid approach, Materials Science and Engineering A, 662, (2016), 330-341

[IV] **S. D. Yadav**, S. Kalácska, M. Dománková, D. C. Yubero, R. Resel, I. Groma, C. Beal, B. Sonderegger, C. Sommitsch and C. Poletti: Evolution of the substructure of a novel 12% Cr steel under creep conditions, Materials Characterization, 115, (2016), 23-31

2nd International Congress on 3D Materials Science
Edited by: Dominique Bernard, Jean-Yves Buffière, Tresa Pollock, Henning Friis Poulsen, Anthony Rollett, and Michael Uchic
TMS (The Minerals, Metals & Materials Society), 2014

INVESTIGATION OF PRE-EXISTING PORES IN CREEP LOADED 9Cr STEEL

Surya Deo Yadav[1], Joerdis Rosc[2], Bernhard Sartory[2], Roland Brunner[2], Bernhard Sonderegger[1,3], Christof Sommitsch[1], Cecilia Poletti[1]

[1]Institute for Materials Science and Welding, Graz University of Technology, Kopernikusgasse 24, A-8010 Graz, Austria
[2]Materials Center Leoben Forschung GmbH (MCL), Roseggerstraße 12, A-8700 Leoben, Austria
[3]Centre for Materials Engineering, Department of Mechanical Engineering, University of Cape Town, Cape Town, South Africa

Keywords: Cavity growth, P91, Martensitic steel, Computed tomography, Modelling

Abstract

Creep failure of materials under service conditions strongly rely on the formation and growth of cavities, encouraging the characterization and modelling of the cavitation process. In the present work pre-existing pores from manufacturing process are investigated in 9Cr steel creep loaded for up to 9000 hours. Scanning electron microscopy (SEM) is used for 2D analysis while Computer tomography (CT) is employed for 3D exploration. Nearest neighbours distances in 3D are calculated from 2D measurements and are decreasing with creep exposure time. The pore growth is studied applying a physical growth model, and experimental results are compared with numerical simulation. From this research it is deduced that damage occurs by agglomeration and growth of pre-existing cavities. The developed model can predict the growth of pores as a function of temperature and load at service.

Introduction

P91 belongs to the family of 9-12 wt-% Cr steels, widely used by the power plant industries to manufacture components such as boiler tubes, super heater tubes and turbine rotors. The microstructure of this 9 wt-% Cr steel consists of tempered martensite having $M_{23}C_6$ carbides distributed along prior austenitic grain boundaries, lath and packet boundaries. Furthermore MX type fine carbonitrides are dispersed throughout the matrix. When the material is exposed to high temperature loading, coarsening of precipitates, formation of new phases (Laves phase, Z-phase) and decrease of the dislocation density within laths due to recovery take place [1]. The precipitation of Laves phase drops the Mo content in the matrix, reducing solid solution strengthening. Precipitation of coarse Z-phase occurs at the expense of finely distributed MX type carbonitrides. Therefore, the density of restraining particles inside the matrix decreases [2]. The synergistic effect of these processes weakens the material and promotes cavitation/pore formation. The cavity nucleation, growth and interlinking are the leading failure mechanism in this material [3]. If macro cavities/pores exist in the material from the manufacturing process, they will be responsible for the final rupture [4]. These pre-existing macro cavities can grow either by diffusion, plasticity or by coupled diffusion and plasticity depending on temperature and applied stress [5].

The main objective of the present research is to characterize and model growth of pre-existing cavities/pores. Scanning electron microscope (SEM) and computed tomography (CT) are employed for characterization while standard stereological method is used for quantification.

Experiments and Methodology

Material and Creep Test

The chemical composition of P91 steel is given in Table 1. The material was supplied by RWE power AG in the form of a pipe with a wall thickness of 21 mm and a diameter of 250 mm. The creep samples were machined from the pipe with an aspect ratio of five. These specimens were creep loaded for 7000 hours and 9000 hours, at 650 ºC with an initial tensile stress of 60 MPa. The elongation was measured using the interrupted strain measurement technique. Mechanical polishing was employed up to 1 µm with silicon carbide polishing paper followed by vibrational polishing with neutral OPH solution for investigation.

Table 1 Chemical composition of used P91steel

Material	**C**	**Si**	**Mn**	**P**	**S**	**Cr**	**Mo**	**Ni**	**Al**	**Nb**	**V**	**N**	**Fe**
Wt-%	0.12	0.31	0.45	0.013	0.003	8.23	0.98	0.13	0.014	0.06	0.22	0.041	balance

Characterization

The pores produced from the manufacturing process having size larger than 1 µm were detected in as received condition by the means of SEM in BSE mode. SEM images using BSE detector were used for 2D measurements. The open source Image J software [6] was used to analyse the images in 2D and features like equivalent diameter, circularity and area were calculated.
X-ray computed tomography (CT) was used to get the 3D localization of the pores within the sample. A GE *nanotom m* was applied for the present investigation. The sample was positioned between an X-ray tube and an X-ray-sensitive flat panel detector to obtain CT scan. A number of radioscopic images were taken and three-dimensional volume was reconstructed by means of a mathematical algorithm [7]. Due to the high density of the P91, a smaller sample of about 560×340 µm was inspected with a resolution of about 2 µm. The quantitative analysis of defects within the sample was not possible due to artefacts within the CT data set which come from scattered radiation, which leads to highly blurred edges in the data [8].

Number Density and Nearest Neighbours Distance

A standard stereological method [4, 9] is used for estimation of number density and volume fraction, assuming that cavities are spherical. The number density in particular size class of cavity having diameter (D_i) is given as:

$$(N_v)_i = \left[(N_A)_i - \sum_{n=i+1}^{k} P_{i,n} D_n (N_v)_n \right] / \ P_i \cdot D_i \qquad (1)$$

Where i = 1, 2, 3…k and n ≤ k. In above equation $(N_A)_i$ is, number of sections of particular size per unit area from all possible sizes and P_i the probability that a random plane intersecting the cavity of diameter i produces a section diameter i. The details about the derivation can be found elsewhere [4]. The nearest neighbour distance is a key parameter for the modelling of pore growth. In terms of number density, the nearest neighbour distance [10-11] of cavities (λ_{3d}) in 3D from the 2D measurements, is given as,

$$\lambda_{3d} = \sqrt[3]{3 \cdot \ln(2)/4\pi \cdot N_v} \tag{2}$$

Growth Modelling of Cavities

The present model was developed to describe the growth of pre-existing cavities, which can grow by addition of vacancies to their surface, under the influence of the local stress. The cavity growth rate is derived in terms of vacancies diffusion flux, which depends on the gradient of chemical potential [5, 12].

$$\frac{dr_{mean}}{dt} = \left(\frac{D_g \nabla\mu}{2kTr_{mean}}\right) \tag{3}$$

In above equation $D_g = D_0 \cdot exp(-Q/RT)$, is the grain boundary diffusion coefficient, $\nabla\mu$ the gradient of chemical potential, k the Boltzmann constant, Q the activation energy, R the gas constant and T is the temperature of loading. The chemical potential at grain boundaries is given by $\mu_{gb} = -\sigma_l\Omega$, while the chemical potential at a cavities surface is given as $\mu_{cavity} = -2\Omega\gamma/r_{mean}$, where σ_l is the local normal stress, Ω is the atomic volume, γ the cavity surface tension and r_{mean} is the mean radius of cavities [13]. The calculated chemical potentials in as received condition are 1.41×10^{-21} and 7.72×10^{-23} J/kg at the grain boundary and at the cavity surface, respectively. Thus cavities act like a sink for vacancies and grain boundaries as sources, triggering the growth of cavities. In the present model it was assumed that the vacancies which are produced in the regime where the local stress is about 10% percentage of the applied stress will diffuse to the cavity surface and contribute to growth (see fig. 1).

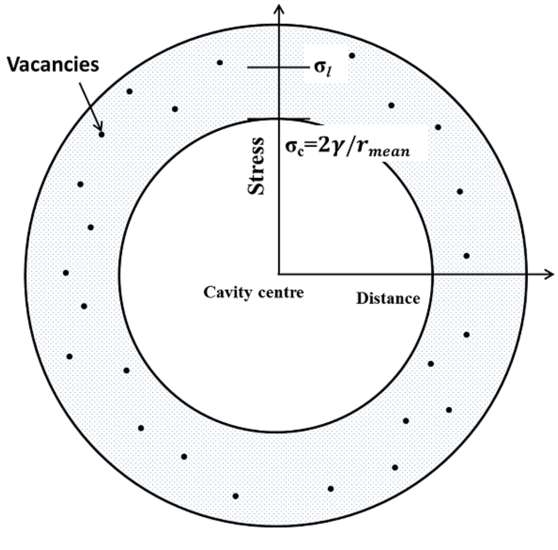

Figure 1. Surface tension at cavity surface and local stress away from cavity

The rest of the produced vacancies, other than in this region, have the tendency to agglomerate elsewhere and form a new cavity. The gradient of the chemical potential can be derived as:

$$\nabla\mu = \frac{\Omega}{\lambda_{3d}k_1}\left(\sigma_l - \frac{2\gamma}{r_{mean}}\right) \tag{4}$$

Here, λ_{3d} is the nearest neighbour distance calculated from equation (2) and k_1 is a constant. The numerical simulation was carried out by MatLab software package taking the mean radius of cavities as 1.28 μm in as received condition as input parameter. The activation energy was taken as Q = 290 kJ/mol and the following values have been chosen for the calculation: $\Omega = 2.35\times10^{-29}$ m^3 ; γ = 2.1 J/m^2 [14-15]. The simulation was performed for three different temperatures, including the experimental tested one.

Results and Discussion

Creep Data

The creep curves of specimens creep loaded for 7000 and 9000 hours with an initial tensile stress of 60 MPa at 650 ºC have shown [4] that the 9000 hours crept specimen has just started moving towards tertiary creep while the 7000 hours crept specimen still is in the secondary creep region. The specimens have shown, steady state creep rate of 8.3×10^{-10} s^{-1}.

Cavities

The pores are almost circular in shape and have a size range of 1 to 6 μm in the as received condition. The size was increased into the range of 2 to 11 μm, while the mean circularity was reduced from 0.86 in as received condition to 0.62 after 9000 hours of creep loading (see fig. 2).

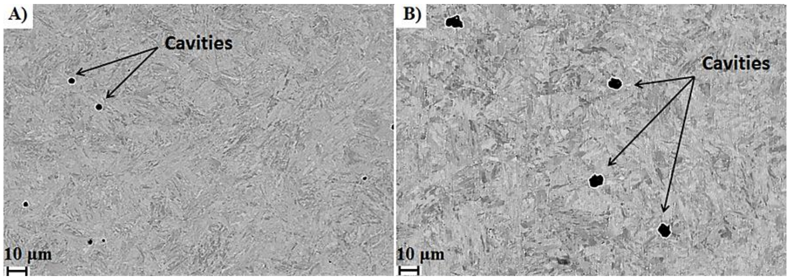

Figure 2. SEM micrograph (in BSE mode) of (a) as received material (b) specimen crept for 9000 hours

The number density of pores was estimated by a stereological method in as received and creep loaded condition. Although, it has been reported that stereological method overestimates the number density [4]. Before creep it was 4.95×10^4 mm^{-3}, while it decreased to 3.95×10^4 and 2.77×10^4 mm^{-3} for 7000 and 9000 hours creep exposed samples, respectively. The mean diameter was 2.56 μm in as received state, which was raised to 5.42 μm after 9000 hours of loading. The initial volume fraction was 0.11% which was upraised to 0.47% after 9000 hours of creep exposure. The increase in mean diameter and volume fraction while the lessening of number density with exposure time suggests growth and agglomeration of pre-existing pores.

The nearest neighbour distance was estimated from equation (2) assuming a random distribution without preferential nucleation sites. Investigation reveals that the distance is found 14.95 μm for as received material while increasing to 16.12 μm and 18.14 μm for 7000 and 9000 hours creep exposed samples, respectively. The nearest neighbour distance between pores is increasing with the creep loading time, which can be attributed to the agglomeration of the pores.

The CT measurement gives an overview of the 9000 hours creep loaded specimen (see fig. 3). The CT data set clearly showed a number of pores within the sample. The pores are represented as dark areas within the brighter volume. As can be estimated from the scale bar at the bottom of the three slices, pores having size range of 6 to 10 μm could be visualized. Figure 3 shows three orthogonal slices and a 3D view of the sample. One specific pore is marked in the slice views as well as in the 3D views. The observation reveals the pores agglomeration which is in accordance with 2D measurements. The spatial distribution shows a heterogeneous spread of the pores throughout the reconstructed volume.

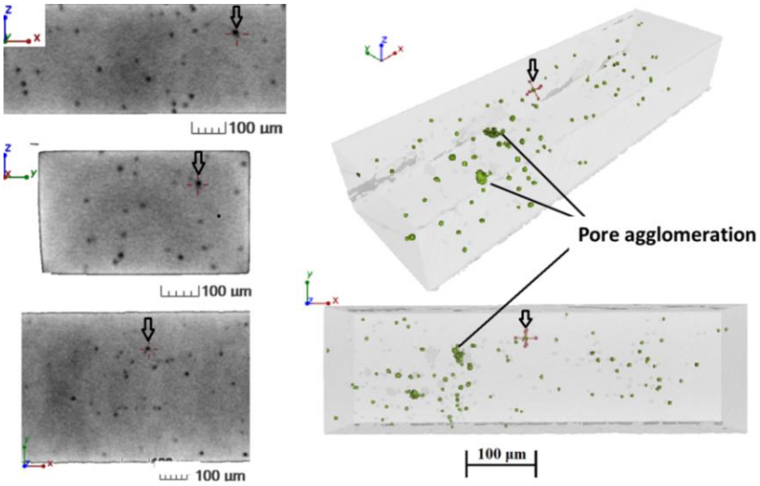

Figure 3. Three orthogonal slices and 3D reconstructed volume (850×789×2398 voxels) of 9000 hours crept specimen

Growth of Cavities

Figure 4 depicts the evolution of the mean radius of cavities with exposure time at three different temperatures. The numerical simulation was carried out assuming that the local stress is 10% of the applied stress. The model shows a good correlation with the experimental results at 650 ºC up to 7000 hours in the secondary creep stage while deviate at 9000 hours. The underestimation of the cavity mean size at 9000 hours is attributed to the macro volume interaction such as cavity agglomeration. After 9000 hours of loading the related specimen is in the tertiary creep stage and thus agglomeration of cavities take place.

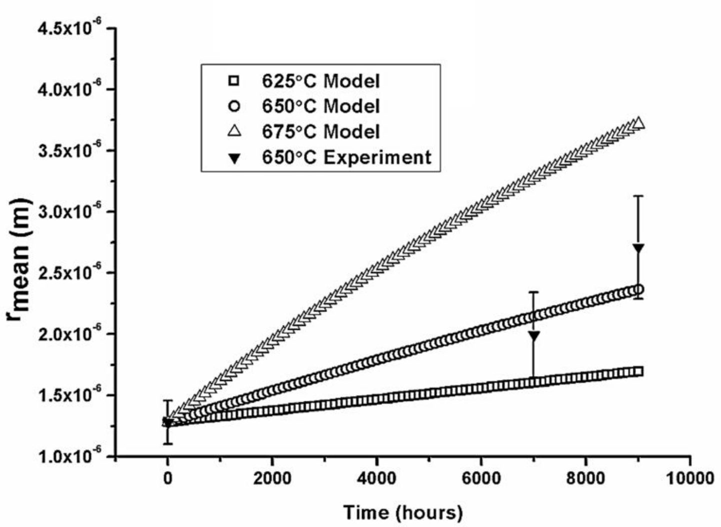

Figure 4. Growth of pre-existing cavities with loading time and temperature using a load of 60 MPa

Summary and Conclusions

This work characterizes the pre-existing pores in a P91 steel employing SEM and CT. The quantification was done using stereological methods. A cavities growth model was developed based on local stress levels. This research reveals that the pre-existing pores are growing followed by agglomeration with creep exposure time.

Acknowledgement

This research work was carried out under the project Hot Pipes number 826434, supported by the FFG -- Austrian Research Promotion Agency.

References

1. C. G. Panait, W. Bendick, A. Fuchsmann, A. F. Gourgues-Lorenzon and J. Besson, “Study of the microstructure of the Grade 91 steel after more than 100000 h of creep exposure at 600 ºC,” *Int. J. of Press. Vessel. and Pip.*, 87 (2010), 326-335.
2. H. K. Danielsen and J. Hald “Behaviour of Z phase in 9-12%Cr steels,” *Energy Mater.*, 1 (2006), 49-57.
3. H. T. Yao, F. Z. Xuan, Z. Wang and S. T. Tu, “A review of creep analysis and design under multi-axial stress states,” *Nucl. Eng. and Des.*, 237 (2007), 1969-1986.
4. S. D. Yadav, B. Sonderegger, B. Sartory, C. Sommitsch and C. Poletti, “Characterization and quantification of cavities in 9Cr martensitic steel for power plants,” *Mater. Sci. Technol.*, under review.
5. M. E. Kassner and T. A. Hayes, “Creep cavitation in metals,” *Int. J. of Plast.*, 19 (2003), 1715-1748.
6. http://imagej.nih.gov/ij/download.html.
7. L. A. Feldkamp, L. C. Davis and J. W. Kress, “Practical cone-beam algorithm,” *J. Opt. Soc. Am. A*, 1 (6) (1984), 612-619.
8. T. Buzug, Einführung in die Computertomographie, Springer-Verlag Berlin Heidelberg 2004.
9. E. E. Underwood, Quantitative Stereology, Addison Wesley Series In Metallurgy And Materials, (1970).
10. B. Sonderegger and E. Kozeschnik, “Particle strengthening in fcc crystals with prolate and oblate precipitates,” *Scripta Mater.*, 66 (2012), 52-55.
11. S. Chandrasekhar, “Stochastic problems in physics and chemistry,” *Rev. Mod. Phys.*, 15 (1943), 1-89.
12. W. Beere and M. V. Speight, “Creep cavitation by vacancy diffusion in plastically deforming solid,” *Metal Science*, April (1978), 172-176.
13. D. Hull and D. E. Rimmer, “The growth of grain-boundary voids under stress,” *Philos. Mag.*, 4 (1959), 673-687.
14. H. Magnusson and R. Sandström, “Creep strain modeling of 9 to 12 Pct Cr steels based on microstructure evolution,” *Metall. Mater. Trans. A*, 38A (2007), 2033-2039.
15. P. Shewmon and P. Anderson, “Void nucleation and cracking at grain boundaries,” *Acta Mater.*, 46 (1998), 4861-4872.

Characterisation and quantification of cavities in 9Cr martensitic steel for power plants

S. D. Yadav*[1], B. Sonderegger[2], B. Sartory[3], C. Sommitsch[1] and C. Poletti[1]

This work focuses on the characterisation of cavities evolution in a P91 steel pipe in three conditions: as received, and after creep at 650°C and 60 MPa for 7000 and 9000 h. A field emission gun scanning electron microscope (FEG-SEM) equipped with focused ion beam (FIB) gun, a conventional scanning electron microscope (SEM) and a light optical microscope (LOM) have been employed for the investigation. This study reveals two types of cavities: the pre-existing cavities, which are rare in this type of heat resistant steels, with a mean diameter of 2·56 μm and the cavities produced during creep with diameters smaller than 0·6 μm. Lath boundaries and precipitates are found to be preferential sites for cavity nucleation. Furthermore, the number density and volume fraction of these small cavities are calculated from 2D measurements and compared to 3D results obtained by FIB serial sectioning.

Keywords: Creep cavities, FIB serial sectioning, Stereology, Precipitates, Martensite, P91

This paper is part of a special issue on Cavitation in materials: new insights from 2D/3D/4D characterisation

Introduction

The material P91 is extensively used for power plant applications such as boiler tubes and super-heater tubes. The microstructure of this 9 wt-%Cr steel consists of tempered martensite with $M_{23}C_6$ (M=Cr, Fe, Mo) carbides distributed along prior austenitic grain boundaries, lath and packet boundaries. Furthermore, fine MX (M=V, Nb and X=C, N) type carbonitrides are dispersed throughout the matrix. When the material is loaded at high temperatures, the microstructure evolves towards the equilibrium due to diffusion and relaxation processes. These main processes are: coarsening of carbides, precipitation of new phases (Laves phase, Z-phase) and decrease in the dislocation density within laths due to recovery and subgrain growth.[1] The precipitation of the Laves phase decreases the solid solution strengthening due to the consumption of Mo from the matrix. It has been reported that the Laves phase form after less than 4000 h of creep exposure at 600°C.[2] Precipitation of the modified Z-phase occurs at the expense of finely dispersed MX type carbonitrides. Z-phase forms after relatively long time of creep exposure i.e. after 34 141 h at 600°C.[3] Therefore, the number density of pinning particles inside the matrix decreases.[4] The synergistic effect of these processes weakens the material and promotes cavitation.

Generally it is well accepted that cavity nucleation, growth and coalescence lead to failure of this type of material during creep.[5] It has been reported that cavities nucleate from the early stage of creep life, i.e. in the primary and secondary creep stages in polycrystalline metals and alloys.[6–8] There are several mechanisms for cavity nucleation described by researchers as a function of temperature and stress.[6,7] These are vacancy accumulation, grain boundary sliding (GBS) and dislocation pile-ups. Furthermore, nucleated micro or any pre-existing cavities[9] have the tendency to grow either by diffusion, plasticity or by coupled diffusion and plasticity, transforming to macro cavities.[6,7,9] Finally, coalescence of these macro cavities leads to the rupture. In 9Cr steels it has been reported that cavities are nucleated at coarse precipitates such as at second phase particles and along grain boundaries.[1,10] In a similar study on 9Cr steel fractured specimen creep loaded at 600°C under a stress of 80 MPa, creep cavities are identified with a size between 3 and 7 μm.[1] Creep damage investigation on E911 steel was done by Sket *et al.*[11] in the similar condition of power plant components and cavity nucleation at lath boundaries was reported. Further it was deduced that cavities growth mechanism is constrained cavity growth. Additionally, the work carried out by Gupta *et al.*[12] gives a deep insight into transition behaviour of cavitation as a function of stress levels which could not be explained by conventional sequence of failure. Although the investigation carried out by Gupta *et al.*[12] is at higher stress levels than the stress used in the present work.

With respect to the characterisation methods, it can be said, that the creep damage investigation in materials has been done by different techniques such as LOM, SEM and synchrotron tomography by different researchers.[11–13] The FIB serial sectioning is an emerging technique enabling the characterization of very small entities (cavities, phases, particles, etc.) up to 0·1 μm resolution. The combination of the high resolution provided by the field emission gun scanning electron microscope (FEG-SEM) with the

---

[1]Institute for Materials Science and Welding, Graz University of Technology, Kopernikusgasse 24, A-8010 Graz, Austria
[2]Centre for Materials Engineering, Department of Mechanical Engineering, University of Cape Town, Cape Town, South Africa
[3]Materials Center Leoben Forschung GmbH (MCL), Roseggerstraße 12, A-8700 Leoben, Austria

*Corresponding author, email surya.yadav@ tugraz.at

Published by Maney on behalf of the Institute
Received 14 February 2014; accepted 29 July 2014
DOI 10.1179/1743284714Y.0000000635

accurate subsequently slicing of the focused ion beam (FIB) enables the characterization of submicron entities. The 3D reconstruction of these entities is obtained from the serial sectioned pictures to get information such as shape factor, number density and morphology.[14] Especially remarkable is the unique description of the morphology and interconnectivity of these features, examples of which include the investigations of TiB whiskers in Ti6Al4V alloy,[15] as well as the description of the complex Si structure in Al–Si12 and Al–Si12–Sr alloys.[16]

The life time of heat resistant steels under service conditions relies heavily on cavitation state.[17] In the authors knowledge, there is no clear correlation of the final damage with the cavities which are formed during creep, neither by the evolution of pre-existing ones.[9] This lack in the literature is our first motivation to study the evolution of these two types of cavities separately. The second motivation is to explore the difference in damage quantification between 2D stereological analysis and 3D serial sectioning for a given morphology of cavities. This encouraged the comparison of results obtained from stereological calculations with serial sectioning techniques.

Experiments and methodology

Material and creep experiments

The chemical composition of the used P91 steel is given in Table 1. The material was supplied by RWE power AG in the form of a pipe with a wall thickness of 21 mm and a diameter of 250 mm. The pipe was normalised at 1060°C for 30 min followed by air cooling, tempered at 770°C for 60 min and air cooled. The creep samples were machined from the pipe with an aspect ratio of five (gauge length/diameter). These specimens were creep loaded for 7000 and 9000 h at 650°C with an initial tensile stress of 60 MPa. The elongation was measured using the interrupted strain measurement technique according to the EN ISO 204:2009 standard.

Characterisation techniques

The present work is focused on the characterisation (LOM, SEM, FEG-SEM equipped with FIB) and quantification of two types of cavities, the pre-existing ones and the ones formed during the creep exposure. While the first ones were characterised by light optical microscope LOM and a conventional (tungsten filament) scanning electron microscope (SEM), the second ones were studied by means of FEG-SEM and FIB serial sectioning. Finally, the volumetric information of creep (small) cavities was calculated from 2D measurements and compared with 3D results obtained from FIB serial sectioning.

Specimens for metallographic preparation were machined from the as received pipe, head and the shaft/gauge of crept samples. Mechanical polishing was employed with silicon carbide polishing paper up to P4000 grit size (European standard) followed by 1 μm diamond paste using Tegrapol-31 polishing machine. Finally, specimens were polished with neutral OPH solution (0·02 μm alumina particles) to avoid modification in the structure of the cavities using VIBROMET 2 vibratory polisher.[18]

The pre-existing cavities (mean diameter 2·56 μm) were imaged by LOM and conventional scanning electron microscopy (SEM) in the back scattered electron (BSE) mode. The tiny creep cavities (diameter <0·6 μm) and some precipitates could not be distinguished using SEM. Therefore, the field emission gun scanning electron microscope (FEG-SEM) imaging technique equipped with In-lens detector was used instead.

The In-lens detector was used at a voltage of 2 kV and a working distance of 5 mm, allowing a highly efficient collection of the secondary electrons (SE1). The edges of cavities produce more electrons than the surrounding areas, appearing brighter in the images (Fig. 1). This effect was used to distinguish cavities from dark precipitates. Pre-existing and small creep cavities were further analysed by means of the open source Image J software[19] and features such as equivalent diameters, circularity and area were quantified.

A dual beam workstation consisting of a focused ion beam (FIB) column and field emission gun column (FEG) was used for serial sectioning to study the small creep cavities (diameter <0·6 μm). The angle between both columns was 52°. Gallium ions were used for slicing, perpendicular to the surface of the sample. The surface was covered with a platinum layer to reduce curtaining effects, and to provide a sharp cutting edge.[15,16,20] The sample was milled in 425 slices by means of a 10 nm diameter ion beam with an inter-slice distance of 30 nm. After each slice, the cross section was imaged using an In-lens detector. Finally, a three dimensional visualisation was obtained from all 425 images using Avizo software, giving a total volume of analysis of $26{\cdot}4\times17{\cdot}3\times12{\cdot}5$ μm^3. The used voxel size was $15\times15\times30$ nm^3. As the segmentation of cavities from some precipitates was not possible using the automatic contrast selection, each cavity was marked manually based on their edge contrast (Fig. 1).

Stereological analysis

In this work, a standard stereological method described in the literature[21–23] was adopted under the assumption that cavities are spherical. The spherical cavities produce imprint of circles on an intersecting random plane as illustrated in Fig. 2. The diameters of the circles are then divided into different size classes D_j. The number of cavities per unit volume $(N_v)_j$ for a particular size class is defined as

$$(N_v)_j=\Sigma_i(N_A)_{i,j}/D_j \tag{1}$$

In equation (1) $\Sigma_i(N_A)_{i,j}$ represents the number of sections of all sizes obtained from the cavities of constant size j per unit area. It is an immeasurable quantity from polished surface but can be calculated.

The probability $P_{i,j}$ that a random plane intersecting the cavity of diameter j produces a section diameter i can be defined as

Table 1 Chemical composition of studied P91steel

Element	C	Si	Mn	P	S	Cr	Mo	Ni	Al	Nb	V	N	Fe
wt-%	0·12	0·31	0·45	0·013	0·003	8·23	0·98	0·13	0·014	0·06	0·22	0·041	Bal.

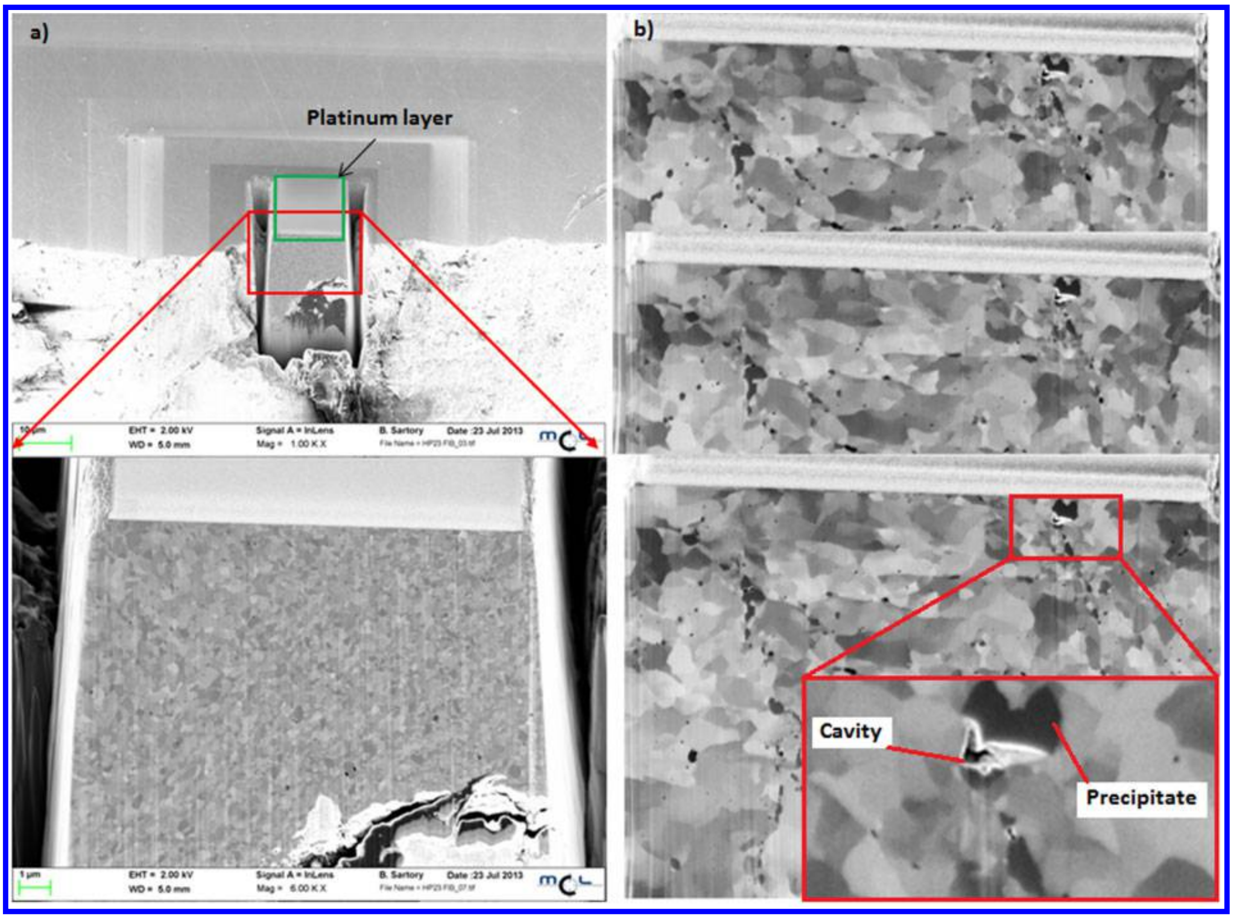

1 FIB-FEG-SEM images of 9000 h crept specimen (gauge) *a* XY section scanned by electron beam; *b* back to back slices (XY) showing lath boundary cavity and precipitate

$$P_{i,j} = \Sigma_j (N_A)_{i,j} / \Sigma_i (N_A)_{i,j} \tag{2}$$

In the equation above, the term $\Sigma_j(N_A)_{i,j}$ represents the number of sections of size i from cavities of all possible sizes per unit area. It is a measurable quantity from the polished plane (Fig. 3).

Merging equations (1) and (2), it yields

$$(N_v)_j = \Sigma_j (N_A)_{i,j} / P_{i,j} D_j \tag{3}$$

In terms of the sections radius, the probability can be derived as (Fig. 4)

$$P_{i,j} = \Delta h / r_{max} = (h_{i-1} - h_i)/r_{max} \tag{4}$$

In the equation above, Δh, the thickness of a slice, is produced by a random plane intersecting a cavity at heights h_i and h_{i-1} yielding to section radii r_i and r_{i-1} respectively. r_{max} is the maximum radius obtained when the random plane intersects a cavity. The probability calculation can be simplified as

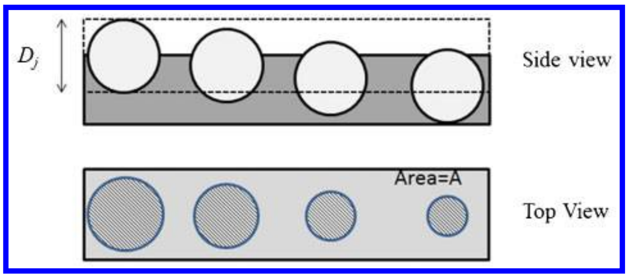

2 Different sections are produced from particular size of cavity intersected by random plane

$$P_{i,j} = \left\{ \left[(r_{max})^2 - (r_{i-1})^2 \right]^{1/2} - \left[(r_{max})^2 - (r_i)^2 \right]^{1/2} \right\} / r_{max} \tag{5}$$

Now, the number of sections of size D_1 per unit area from all possible sizes is given as

$$(N_A)_1 = \Sigma_j (N_A)_{i,j} = (N_A)_{1.1} + (N_A)_{1.2} + (N_A)_{1.3} + (N_A)_{1.4} + (N_A)_{1.5} + \cdots \tag{6}$$

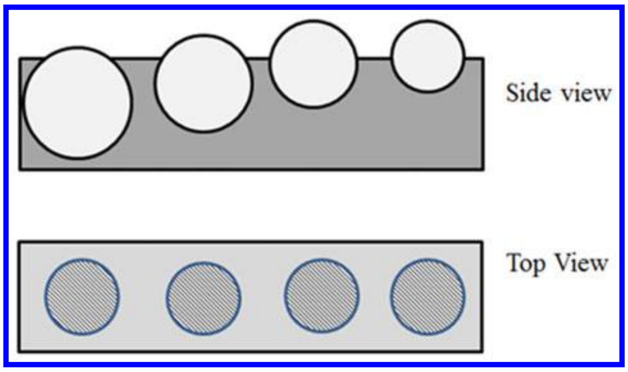

3 Same section size produced by different diameters of cavities intersected by random plane

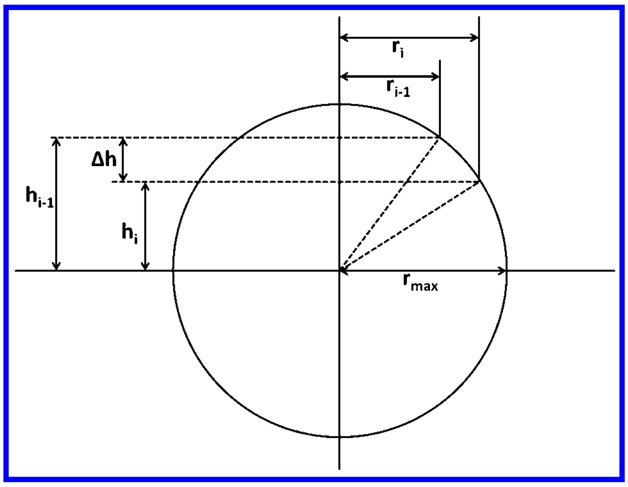

4 Spherical cavity intersected by random plane at two different heights

Therefore, the number of sections of size D_1 produced from the size class 1 is

$$(N_A)_{1.1}=(N_A)_1-(N_A)_{1.2}-(N_A)_{1.3}-(N_A)_{1.4}-(N_A)_{1.5}-\cdots \tag{7}$$

From equations (3) and (7), it follows that the number of cavities per unit volume for the size class 1 is

$$(N_v)_1=[(N_A)_1-(N_A)_{1.2}-(N_A)_{1.3}-(N_A)_{1.4}-(N_A)_{1.5}-\cdots]/P_{1.1}D_1 \tag{8}$$

Hence, from equations (3) and (8) follows

$$(N_v)_1=\frac{[(N_A)1-P_{1,2}D_2(N_v)_2-P_{1,3}D_3(N_v)_3-P_{1,4}D_4(N_v)_4-P_{1,5}D_5(N_v)_5-\cdots]}{P_{1,1}D_1} \tag{9}$$

In this way, the size distribution for each size class was obtained. The volume fraction of the particular size class is calculated as $[V_j\ (N_v)_j]$, where V_j is equal to $[\pi(D_j)^3/6]$ and this gives the total volume fraction of cavities as

$$V=\Sigma_j V_j(N_v)_j \tag{10}$$

Results and discussion

Creep properties

The creep tests carried out on P91 at 650°C under 60 MPa stress were interrupted after 7000 h and after 9000 h of testing. The strain–time plot obtained from these tests is shown in Fig. 5*a*. The strain rate–time plot is also shown in Fig. 5*b*. It can be seen that after 7000 h of creep loading the specimen has started moving towards tertiary creep.

The obtained minimum creep rate was $4{\cdot}8\times10^{-8}$ s^{-1}. This value is higher than the one reported by Kloc *et al.*[24] (1×10^{-9} s^{-1}) for the same equivalent stress and temperature, although using helicoid samples. The stress values used in the Ref. 24 may be compared with the present work by means of simple von-Mises criteria. Furthermore, the minimum creep rate of 9Cr–1Mo steel depends strongly on the heat treatments imposed on the material.[25] No conclusion can be drawn due to the presence of pre-existing pores, since they have not been reported before in the literature. It must be mentioned that acceleration in the creep rate due to the pre-existing pores in powder metallurgy produced materials was discussed by Davies *et al.*[7] in their work.

Pre-existing and creep cavities

Two types of cavities were identified in this research: large pre-existing ones (mean diameter 2·56 μm) already present in the manufactured pipes and cavities formed during creep (diameter <0·6 μm)). Figure 6 shows the microstructure of the as received material obtained by light optical microscopy. Black spots represent a combination of non-distinguishable pre-existing pores, precipitates and inclusions.

Pores were identified using, both back scattered electrons (BSE) and EDX analysis. Figure 7 shows the bright edge contrast of the cavities in BSE mode. EDX analysis and elemental mapping showed the presence of impurities and aluminium within the pores (Figs. 7 and 8).

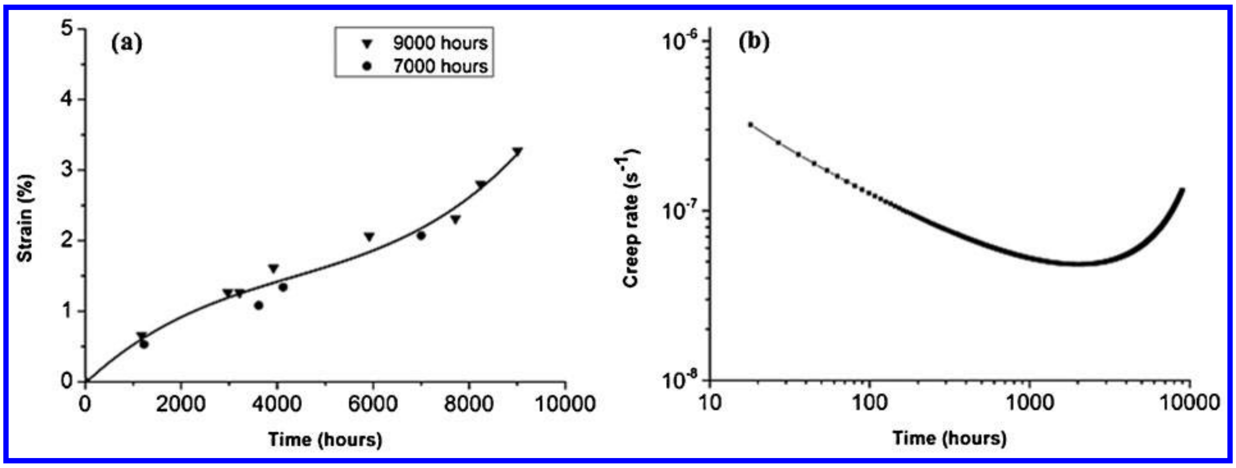

5 *a* creep curve of P91 steel loaded at 650°C and 60 MPa and *b* creep rate as function of time

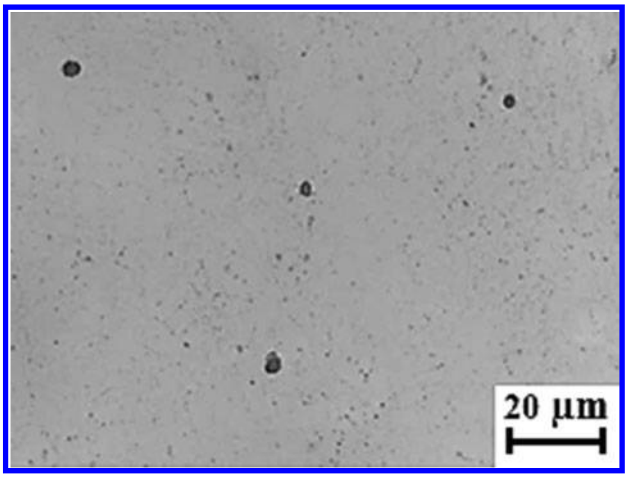

6 LOM micrograph showing pre-existing pores in as received material

Figure 9 shows the SEM micrograph of the as received and creep loaded specimens using the BSE mode. The large, relatively circular, pre-existing cavities from the manufacturing process can be already seen in the as received condition (Fig. 9*a*).

The microstructure of the material after 7000 h of creep loading is shown in Fig. 9*b*. Three types of features could be observed: large pre-existing cavities, small creep cavities and two type of precipitates: light (black) and dense (bright). The presence of new precipitates and small cavities could be seen clearly only in the crept specimen while they are not present in the as-received material. In Fig. 9*b* it is hard to differentiate creep cavities from AlN precipitates, because both appear black and the resolution is limited for any further analysis. The AlN particles are observed in most of the cases associated with a $M_{23}C_6$ (white) precipitate at grain boundaries, as reported for P92 steels in the literature.[26] Figures 10 and 11 depict the EDX analysis of 9000 h creep loaded specimen (gauge). The presence of AlN particles were confirmed in the vicinity of Cr rich precipitates (Fig. 10). Figure 11 shows the EDX analysis of small creep cavity. Remarkable is the same contrast (black) of creep cavities and AlN.

FEG-SEM combined with an In-lens detector could be successfully used to identify the difference between a cavity and a precipitate due to their different edge contrast (Fig. 12). It should be noted that when using this detector, $M_{23}C_6$ particles no longer appeared white, but dark as the AlN.

Creep cavities were found preferentially along the lath boundaries and in the vicinity of second phase particles in the gauge section of 9000 h crept specimen (Fig. 12). It has been reported that in 9Cr steels cavities are prone to nucleate at $M_{23}C_6$ carbides and Laves phase during creep exposure.[10] The creep voids on lath boundaries have been also reported by Sket *et al.* in E911 steel.[11] The mechanism of the cavity nucleation for such materials under creep conditions is a complex phenomenon.[6] The applied stress used in this work for the creep tests was lower than 100 MPa, suggesting viscous creep regime.[24] Thus, nucleation by vacancy condensation is

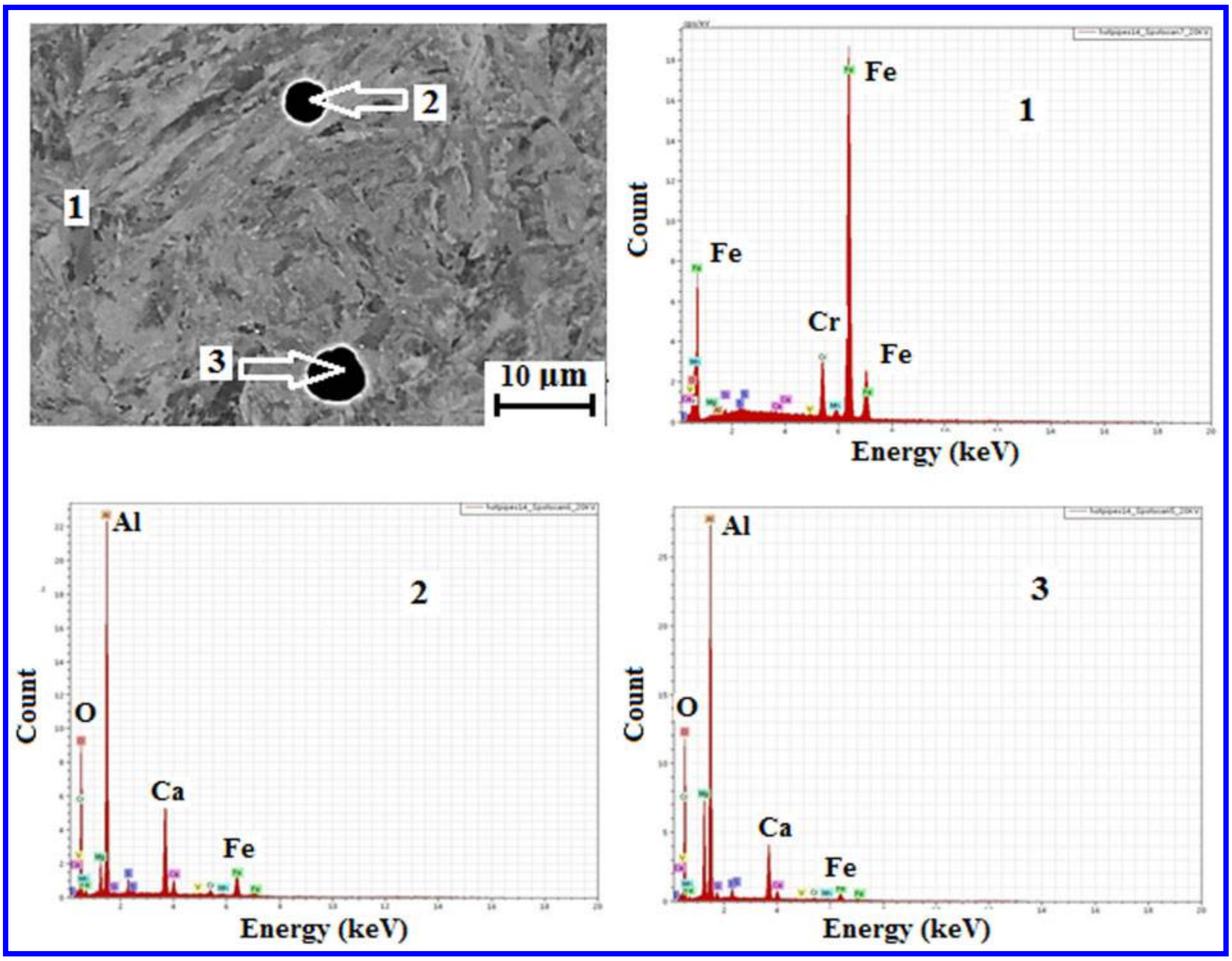

7 EDX analysis of pre-existing pores in as received material

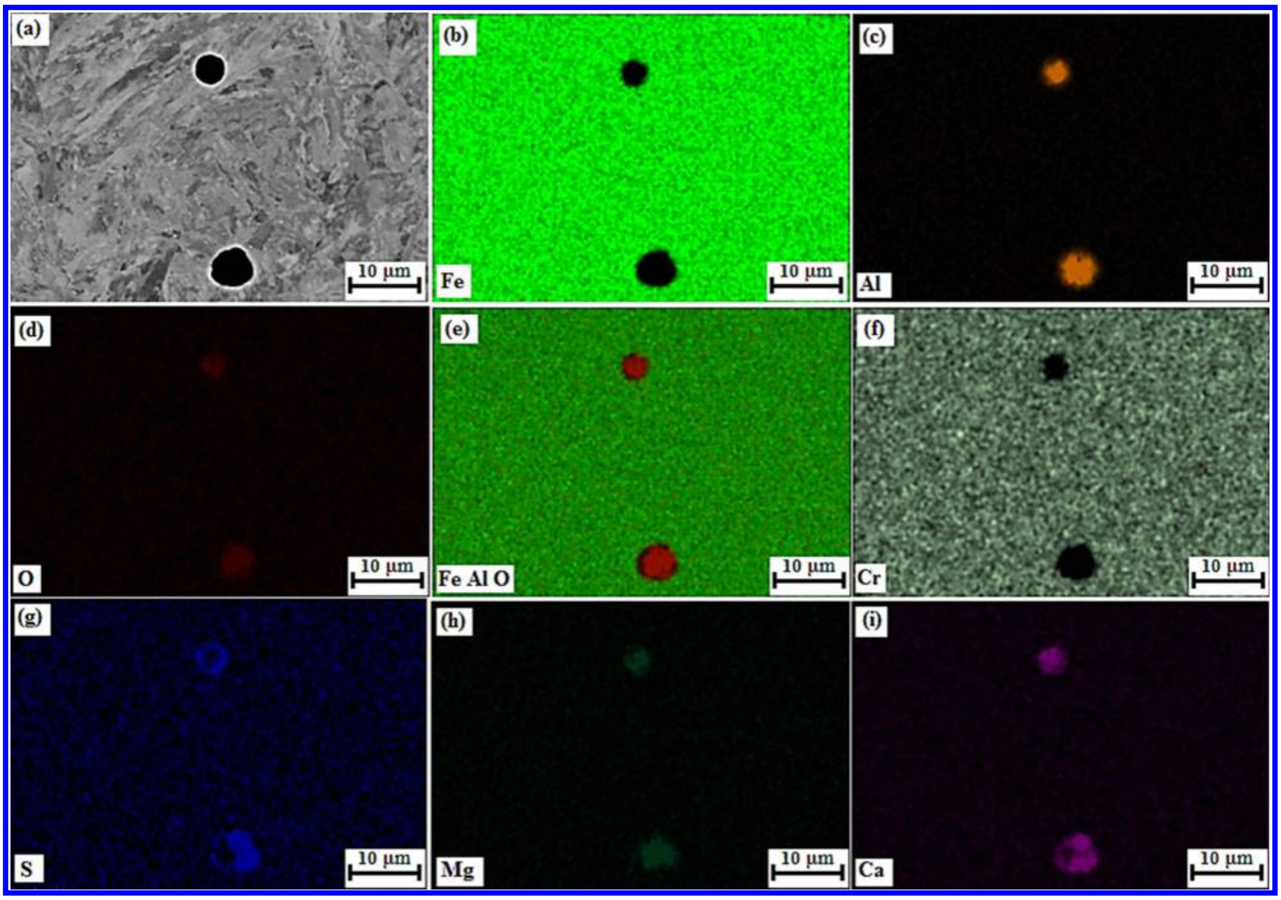

8 SEM micrograph in BSE mode and elemental mapping of as received material *a* micrograph, *b* iron, *c* aluminium, *d* oxygen, *e* aluminium and oxygen; *f* chromium; *g* Sulphur; *h* Magnesium; *i* Calcium

the most probable mechanism, occurring mainly at lath boundaries. The chemical potential of a vacancy is a function of the normal tension across the boundaries.[27] Therefore, these vacancies can agglomerate to form stable cavities.[6] On the other hand, cavitation due to grain boundary sliding (GBS) is less probable, due to the fact that martensitic lath structure, contrary to equiaxed grains, is not convenient for GBS.[11] With respect to plasticity voids it can be said, that the stress is not high enough to produce micro cracks due to large amount of dislocation pile-ups. Furthermore, the specimen has just started to move towards tertiary creep. However, the role of dislocations cannot be ruled out due to the fact that, their accumulation around precipitates raises the

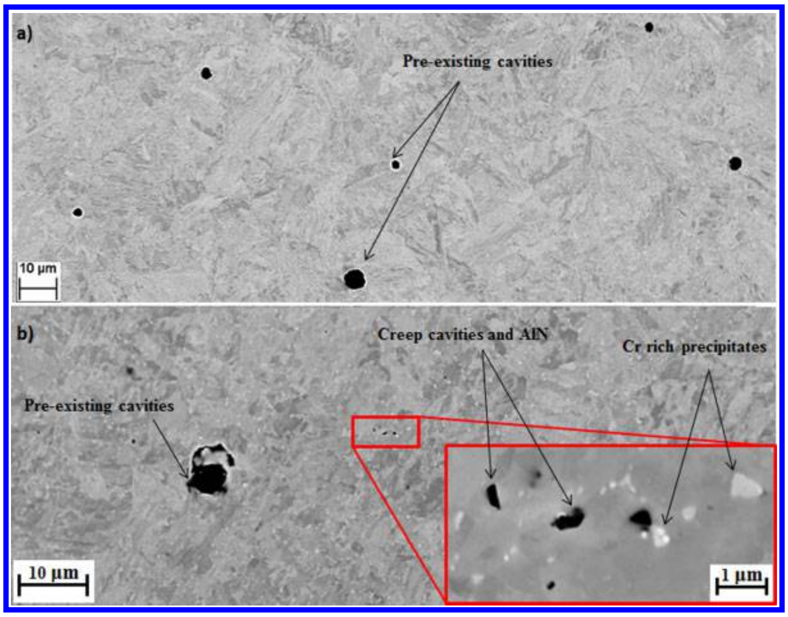

9 SEM micrograph in BSE mode of *a* as received material, *b* specimen (gauge) crept for 7000 h showing big pre-existing cavity as well as small creep cavities and precipitates

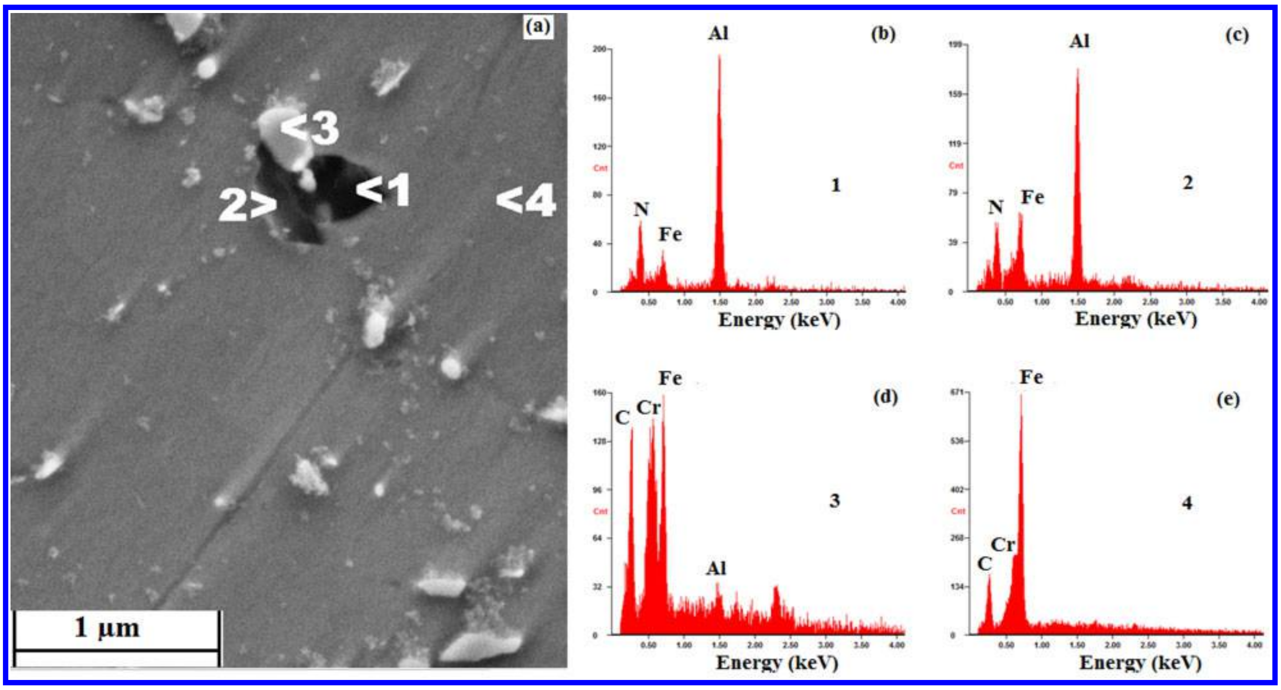

10 FEG-SEM EDX analysis 9000 h crept specimen (gauge) *a* micrograph, *b c* AlN, *d* $M_{23}C_6$ and *e* matrix

local stress level, helping the vacancies to condense and form cavity nuclei.

Large pre-existing cavities

The LOM micrographs of head and gauge sections of 7000 and 9000 h creep loaded specimens are given in Fig. 13. The stress in the gauge section causes the change in shape of the black entities, which, as before, represent pores and inclusions or large precipitates (Fig. 13*b* and *d*). The shape of pores in head section is relatively circular in comparison to the ones in the gauge section (Fig. 13*a* and *c*). Any final conclusion based on optical micrographs could not be done due to the fact that, inclusions and cavities cannot be distinguished easily using LOM. Thus SEM micrographs were used for further investigation.

The SEM micrograph of as received material showed that the initial pre-existing cavities were almost circular and that after creep exposure their shape and size were modified (Fig. 14*a* and *b*). The circularity of cavities was calculated as

$$\text{Circularity} = 4\pi[\text{area}/\text{perimeter}^2] \tag{11}$$

While the mean value of the circularity of pre-existing cavities before creep was 0·86, this value decreased to 0·62 after a creep exposure of 9000 hours (Fig. 14*c*).

The volumetric distributions of big cavities calculated from 2D measurements before and after creep were compared in Fig. 15. The volume fractions of these cavities before and after creep were calculated based on stereological method and shown in Table 2. It was observed that the volume fraction of cavities increased by almost five times after 9000 h of creep exposure. Furthermore, the number of cavities per unit volume

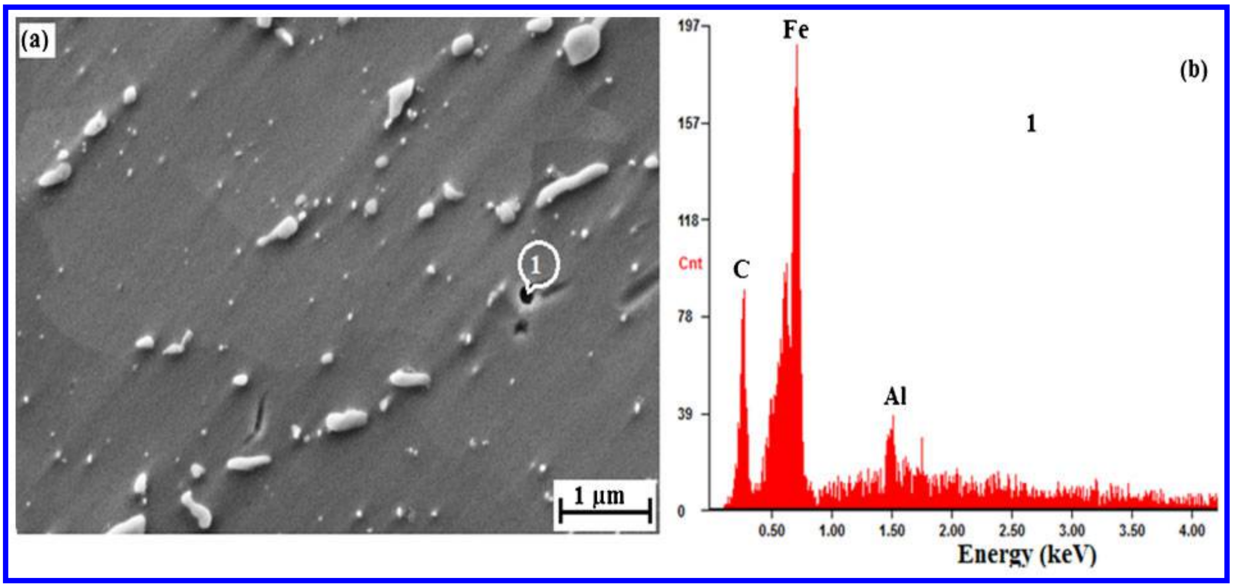

11 FEG-SEM micrograph and EDX analysis of small cavity in 9000 h crept specimen (gauge) *a* micrograph; *b* EDX analysis of cavity

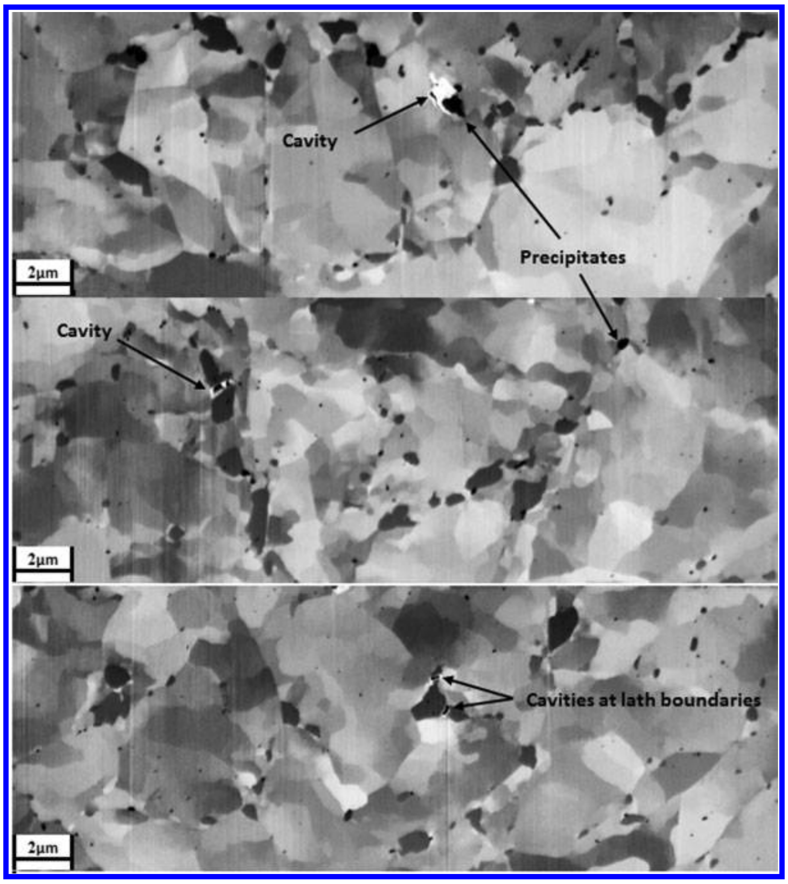

12 FEG-SEM micrograph (In-lens detector) showing creep cavities (black with edge contrast) at lath boundaries and precipitates ($M_{23}C_6$ and AlN, both dark) in 9000 h crept specimen (gauge)

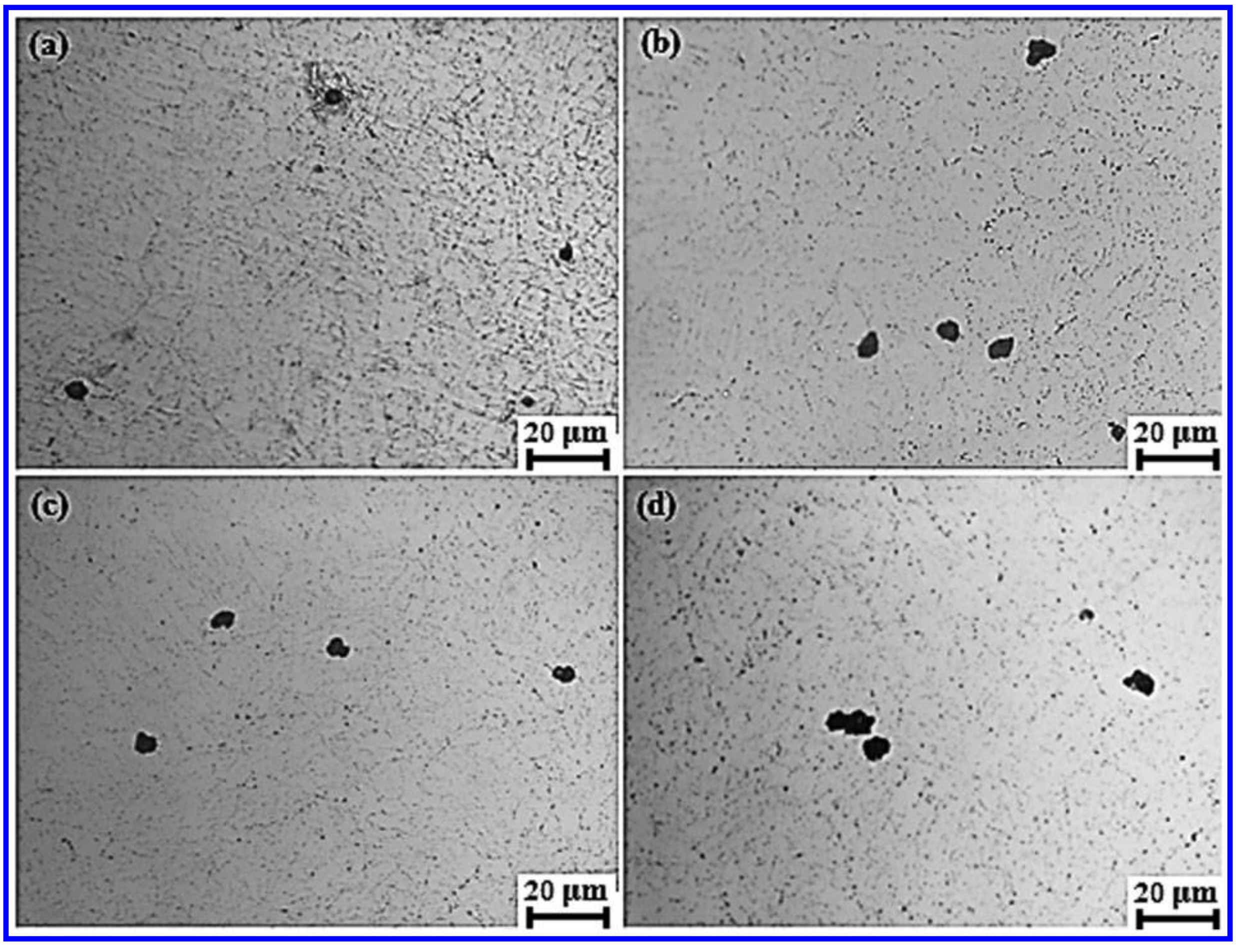

13 LOM micrograph of creep loaded specimens for 7000 h *a* head, *b* gauge; and 9000 h *c* head, *d* gauge

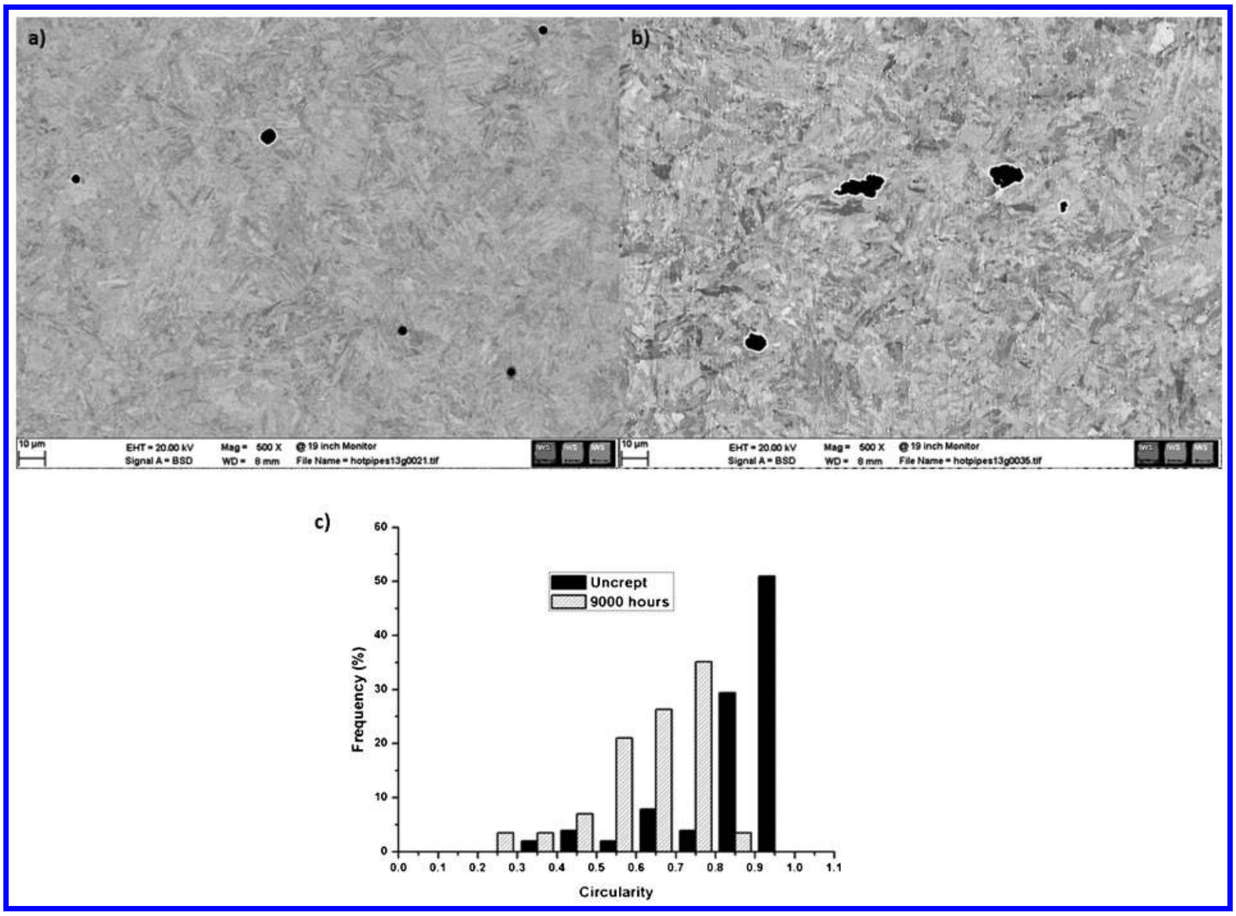

14 SEM micrographs (BSE) of specimen *a* in as received condition, *b* crept for 9000 h and *c* circularity of pre-existing cavities before and after creep loading

decreased while both mean diameter and volume fraction increased with the creep exposure time. Therefore, growth and coalescence of pre-existing cavities is inferred. The growth and coalescence of these pre-existing pores was further studied by the authors.[9]

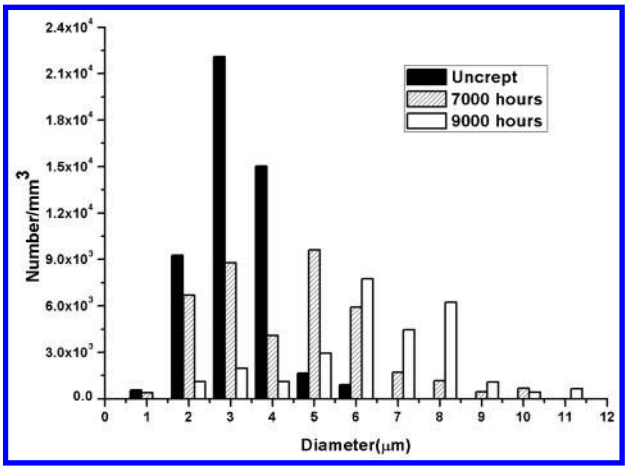

15 Number of big cavities per unit volume for different size classes in as received 7000 and 9000 h creep loaded specimens

Small creep cavities

The three dimensional visualization from the FIB serial sectioned data set of 9000 h crept specimen resulted in a volume of $26{\cdot}4\times17{\cdot}3\times12{\cdot}5$ µm^3. The heterogeneous spatial distribution of creep cavities can be visualised in Fig. 16*a* from the 3D rendered data set. Figure 16*b* shows that most creep cavities presented flake type morphology. The morphology of these cavities was different to that reported for 11 Cr martensitic steel, in which oblate and multi-lobed creep voids at 600°C under the load of 120 MPa were found after fracture.[12] Figure 16*c* is enlarged view of the marked volume in Fig. 16*a*, which showed few cavities in the vicinity of precipitates.

The number density and volume fraction were obtained from the 3D rendered data set. In Fig. 17 and Table 3 these were compared with the data obtained by the stereological method using the measurements of polished surface (2D).

It can be observed that the distribution and volume fraction of creep cavities are overestimated using the stereological method. The calculated volume fraction

Table 2 Pre-existing cavities before and after creep

Specimen	Mean diameter/µm	Volume fraction/%	Total no./mm^3
Uncrept	2·56	0·11	$4{\cdot}95\times10^4$
7000 h	3·99	0·27	$3{\cdot}95\times10^4$
9000 h	5·42	0·47	$2{\cdot}77\times10^4$

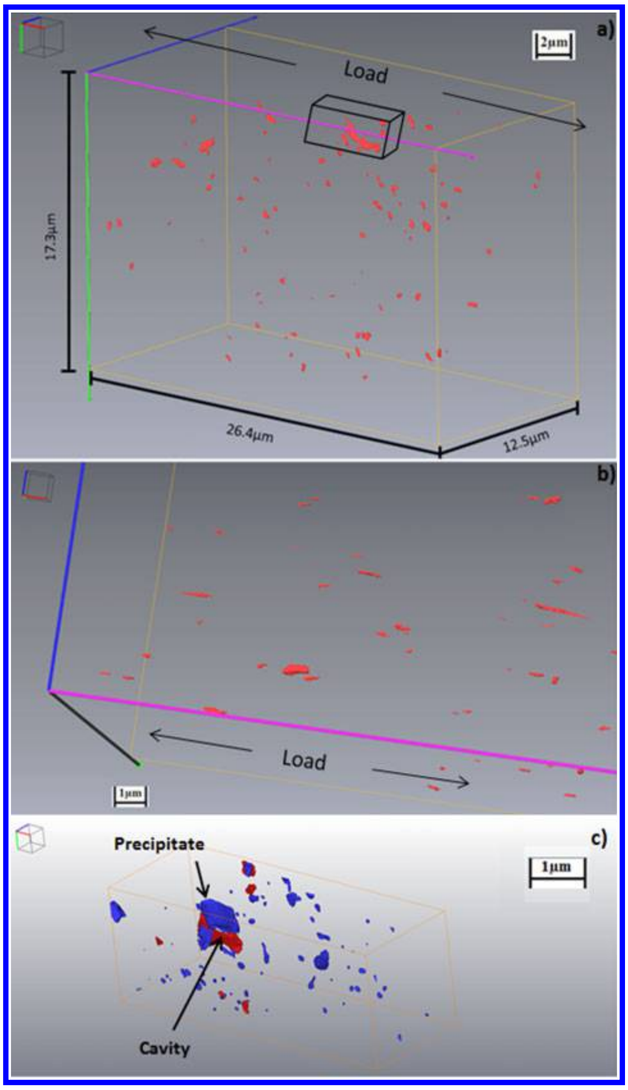

16 **3D reconstructed volume from FIB serial sectioned data set of specimen crept for 9000 h (gauge) *a, b* showing flake type creep cavities; *c* creep cavities (red) in vicinity of precipitates (blue)**

from 2D measurements is nearly four times higher than the actual volume fraction obtained from reconstructed 3D data from FIB serial sectioning. The reason of this difference is that cavities were assumed to be spherical when using stereological calculations, while the three dimensional visualisation of cavities showed complex and flake type shapes (Fig. 16).

Finally, it is noteworthy that the obtained volume fraction from 2D of large pre-existing cavities was almost twelve times higher than that of small creep cavities (see Tables 2 and 3). Thus, in present case the final fracture should be predominately attributed to the growth and coalescence of large pre-existing cavities, and not to the solely nucleation and growth of creep cavities.

Table 3 Volume fraction and number density of creep cavities after 9000 h

Analysis	Total no./mm^3	Volume fraction/%
2D Stereological calculations	$2{\cdot}80\times10^7$	0·038
3D Rendered data	$1{\cdot}54\times10^7$	0·010

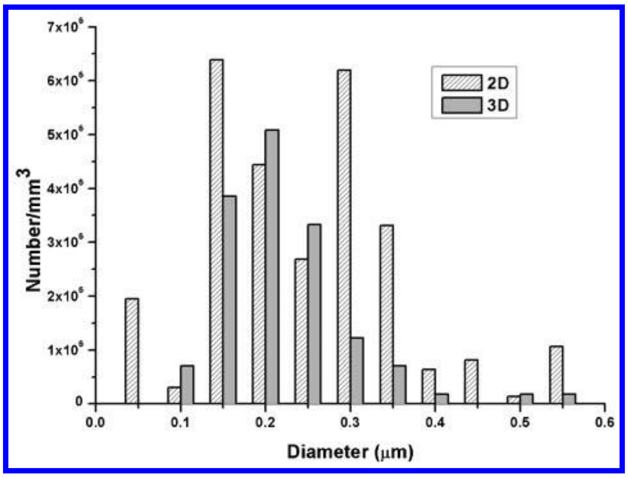

17 **Number of small cavities per unit volume (2D versus 3D) for different size classes in a 9000 h creep loaded specimen**

Conclusions

This work studied the evolution of cavities during the creep of P91 steel for a given creep condition. The following conclusions can be drawn from the investigation.

1. Two categories of cavities were found over the course of the investigation: large pre-existing cavities with an initial mean diameter of 2·56 μm and smaller cavities formed during creep exposure.
2. The growth and coalescence of pre-existing cavities was observed with creep exposure time. The total volume fraction of large pre-existing cavities after 9000 h of creep loading was nearly twelve times higher than the volume fraction of cavities formed during creep.
3. Small cavities were distinguished from precipitates due to their edge effect using an In-lens detector and could be, in this way, be quantified.
4. The 3D visualisation has shown that creep cavities have complex flake type morphology.
5. The overestimation of the number density and volume fraction of creep cavities using the stereological method was attributed to the actual complex shape of cavities, assumed to be spherical in stereological calculations.

It was shown that big cavities are already present in the material, and there growth and coalescence was observed with exposure time. Therefore, pre-existing cavities should be taken into account to predict the final rupture of the sample in the tertiary regime of creep.

Acknowledgements

The experimental work was carried out under the project Hot-Pipes: 826434, ‘Entwicklung eines SHM-Systems für die Überwachung von Hochtemperatur-Rohrleitungen in Kraftwerken’ and the analysis under the project Z-Ultra: 309916, ‘Z phase strengthened steels for ultra-supercritical power plants’. The authors would like to thank the FFG Austrian Research Promotion Agency in Vienna and the European Commission for their financial support.

References

1. C. G. Panait, W. Bendick, A. Fuchsmann, A. F. Gourgues-Lorenzon and J. Besson: ‘Study of the microstructure of the Grade

91 steel after more than 100000 h of creep exposure at 600°C', *Int. J. Press. Vessel. Pip.*, 2010, **87**, 326–335.

2. J. Hald: 'Creep strength and ductility of 9 to 12% chromium steels', *Mater. High Temp.*, 2004, **21**, (1), 41–46.
3. H. Danielsen and J. Hald: 'A thermodynamic model of the Z-phase Cr(V,Nb)N', *Calphad*, 2007, **31**, 505–514.
4. H. K. Danielsen and J. Hald: 'Behaviour of Z phase in 9–12%Cr steels', *Energy Mater.*, 2006, **1**, 49–57.
5. H. T. Yao, F. Z. Xuan, Z. Wang and S. T. Tu: 'A review of creep analysis and design under multi-axial stress states', *Nucl. Eng. Des.*, 2007, **237**, 1969–1986.
6. M. E. Kassner and T. A. Hayes: 'Creep cavitation in metals', *Int. J. Plast.*, 2003, **19**, 1715–1748.
7. A. J. Perry: 'Review cavitation in creep', *J. Mater. Sci.*, 1974, **9**, 1016–1039.
8. V. Sklenicka, K. Kucharova, M. Svoboda, L. Kloc, J. Bursik and A. Kroupa: 'Long-term creep behavior of 9–12%Cr power plant steels', *Mater. Charact.*, 2003, **51**, 35–48.
9. S. D. Yadav, J. Rosc, B. Sartory, R. Brunner, B. Sonderegger, C. Sommitsch and C. Poletti: 'Investigation of pre-existing pores in creep loaded 9Cr steel', Proc. Conf. 2nd Int. Congress on '3D Materials science', Annecy, France, 2014, TMS (The Minerals, Metals & Materials Society), 85–90.
10. J. S. Lee, H. G. Armaki, K. Maruyama, T. Muraki and H. Asahi: 'Causes of breakdown of creep strength in 9Cr-1·8W-0·5Mo-VNb steel', *Mater. Sci. Eng. A*, 2006, **A428**, 270–275.
11. F. Sket, K. Dzieciol, A. Borbély, A. R. Kaysser-Pyzalla, K. Maile and R. Scheck: 'Microtomographic investigation of damage in E911 steel after long term creep', *Mater. Sci. Eng. A*, 2010, **A528**, 103–111.
12. C. Gupta, H. Toda, C. Schlacher, Y. Adachi, P. Mayr, C. Sommitsch, K. Uesugi, Y. Suzuki, A. Takeuchi and M. Kobayashi: 'Study of creep cavitation behavior in tempered martensitic steel using synchrotron micro-tomography and serial sectioning techniques', *Mater. Sci. Eng. A*, 2013, **A564**, 525–538.
13. H. Toda, E. Maire, S. Yamauchi, H. Tsuruta, T. Hiramatsu and M. Kobayashi: 'In situ observation of ductile fracture using X-ray tomography technique', *Act. Mater.*, 2011, **59**, 1995–2008.
14. W. Xu, M. Ferry, N. Mateescu, J. M. Cairney and F. J. Humphreys: 'Techniques for generating 3-D EBSD microstructures by FIB tomography', *Mater. Charact.*, 2007, **58**, 961–967.
15. C. Poletti, G. Requena, D. Tolnai, P. Cloetens and A. Steiger-Thirsfeld: 'Characterization of the microstructure and damage mechanisms in a Ti6Al4V alloy modified with 1 wt.% B', *Int. J. Mat. Res.*, 2007, **55**, 3875–3882.
16. F. Lasagni, A. Lasagni, E. Marks, C. Holzapfel, F. Mücklich and H. P. Degischer: 'Three-dimensional characterization of 'as-cast' and solution-treated AlSi12(Sr) alloys by high-resolution FIB tomography', *Act. Mater.*, 2010, **101**, 1151–1157.
17. A. R. Ragab: 'Creep rupture due to material damage by cavitation', *J. Eng. Mater. Technol.*, 2002, **124**, 199–205.
18. G. Dimmler, W. Schalk, P. Weinert, H. Gruber, S. Wieser and H. Cerjak: 'Sample preparation for high-resolution damage examinations in SEM', *Prak. Metallogr.*, 2002, **39**, 619–633.
19. http://imagej.nih.gov/ij/download.html
20. N. Viveta, S. Chupina, E. Estradea, A. Richardb, S. Bonnamyc, D. Rochaisa and E. Brunetona: 'Effect of Ni content in SOFC Ni-YSZ cermets: A three-dimensional study by FIB-SEM tomography', *J. Power Sources*, 2011, **196**, 9989–9997.
21. E. E. Underwood: 'Quantitative stereology', 2nd edn, 109–113; 1970, Reading, MA, Addison-Wesley Publishing Company.
22. H. A. Schwartz: 'The metallographic determination of the size distribution of temper carbon nodules', *Met. Alloy.*, 1934, **5**, (6), 139–140.
23. S. A. Saltykov: 'Stereometric metallography', 2nd edn; 1958, Moscow, Metallurgizdat.
24. L. Kloc and V. Sklenicka: 'Transition from power-law to viscous creep behaviour of P-91', *Mater. Sci. Eng.*, 1997, **A234**–**A236**, 962–965.
25. B. K. Choudhary: 'Tertiary creep behaviour of 9Cr–1Mo ferritic steel', *Mater. Sci. Eng. A*, 2013, **A585**, 1–9.
26. H. Naoi, M. Ohgami, X. Kiu and T. Fujita: 'Effect of aluminum content on the mechanical properties of a 9Cr-0·5Mo-1·8W steel', *Metall. Mater. Trans. A*, 1997, **28A**, 1195–1203.
27. D. Hull and D. E. Rimmer: 'The growth of grain-boundary voids under stress', *Philos. Mag.*, 1959, **4**, (42), 673–687.

Materials Science & Engineering A 662 (2016) 330–341

Contents lists available at ScienceDirect

Materials Science & Engineering A

journal homepage: www.elsevier.com/locate/msea

Modelling the creep behaviour of tempered martensitic steel based on a hybrid approach

Surya Deo Yadav [a,*], Bernhard Sonderegger [a], Muhammad Stracey [b], Cecilia Poletti [a]

[a] Institute of Materials Science and Welding, Graz University of Technology, Kopernikusgasse 24, A-8010 Graz, Austria
[b] Centre for Materials Engineering, Department of Mechanical Engineering, University of Cape Town, Cape Town, South Africa

ARTICLE INFO

Article history:
Received 16 January 2016
Received in revised form
14 March 2016
Accepted 15 March 2016
Available online 16 March 2016

Keywords:
Creep
P92
Physically based modelling
Dislocations
Precipitates
Damage

ABSTRACT

In this work, we present a novel hybrid approach to describe and model the creep behaviour of tempered martensitic steels. The hybrid approach couples a physically based model with a continuum damage mechanics (CDM) model. The creep strain is modelled describing the motions of three categories of dislocations: mobile, dipole and boundary. The initial precipitate state is simulated using the thermodynamic software tool MatCalc. The particle radii and number densities are incorporated into the creep model in terms of Zener drag pressure. The Orowan's equation for creep strain rate is modified to account for tertiary creep using softening parameters related to precipitate coarsening and cavitation. For the first time the evolution of internal variables such as dislocation densities, glide velocities, effective stresses on dislocations, internal stress from the microstructure, subgrain size, pressure on subgrain boundaries and softening parameters is discussed in detail. The model is validated with experimental data of P92 steel reported in the literature.

1. Introduction

9–12% Cr steels are suitable candidates for fossil-fuel power plants. Due to the low procurement costs and favourable properties at high temperatures, they are used extensively in superheater tubes and boiler parts [1–6]. In order to fulfil the demand of power and the environmental safety requirements, the efficiency of power plants has to be increased as well. The efficiency of fossil-fuel power plants can be increased by raising the temperature and the pressure of the steam. Typically, power plant components are designed to operate longer than 10 years. Recently developed 9% Cr steels are suitable for temperatures up to 600 °C and pressures in the range of 30 MPa [7,8]. These operation parameters result in a reduction of 30% of CO_2 emissions when compared to subcritical power plants (540 °C/18 MPa). Current developments aim to increase the temperature and pressure limits up to 650 °C and 32.5 MPa, respectively [7,8] with a consequent reduction in the production of greenhouse gases.

In addition to creep deformation, oxidation of the material must be taken into account. The oxidation at temperatures up to 650 °C is kept low by increasing the Cr level from 9 to 12%. During recent decades, many attempts have been made to increase the Cr content and develop 11–12% Cr steels. These steels have offered excellent short-term creep strength, but failed dramatically during long-term tests, generally after 10,000 h, due to microstructural degradation caused by the formation of modified Z-phase [7,8].

Due to the difficulties inherent in increasing the creep and oxidation resistance of these materials, gaining a detailed understanding of the underlying phenomena is of utmost importance. One step in this direction is to obtain a physical description of creep based on the microstructural evolution [9]. Several successful attempts have been made to model the creep behaviour of tempered martensitic steels. Ghoniem et al. [10] used a physically based approach including internal variables such as dislocation densities, subgrain size and precipitation state to model the creep behaviour of HT-9 martensitic steel. In other studies, the model was also used to predict the microstructure evolution of tool steel, during service [11–13]. Barkar et al. [9] used an approach whereby hard and soft regions in the microstructure were defined to describe the creep behaviour of 9–12% Cr steels. Magnusson et al. [14] used two different approaches to predict the primary and tertiary stages of creep to model the complete creep curve. Apart from these physically based models, the continuum damage mechanics (CDM) approaches have also been extensively used to model creep behaviour in these types of steels [15–18]. Basirat et al. [19] coupled the physically based model with the CDM approach to model the creep curves without taking into account the behaviour of subgrains.

All these modelling studies, which address the creep curve, have made significant contributions to this research field.

---

[*] Corresponding author.
E-mail addresses: surya.yadav@tugraz.at (S.D. Yadav), bernhard.sonderegger@tugraz.at (B. Sonderegger), strmuh001@myuct.ac.za (M. Stracey), cecilia.poletti@tugraz.at (C. Poletti).

http://dx.doi.org/10.1016/j.msea.2016.03.071
0921-5093/

However, there exists a lack of focus on the specific influence of internal variables involved in the modelling of creep behaviour [9–13,19,20]. For this reason, we developed a hybrid model to describe the creep behaviour using internal variables, and their evolution is analysed together with the creep curves. The coupling of physical based model with CDM is necessary to account for softening and describe tertiary creep.

In this paper, we model the creep behaviour of a steel grade P92 used in [21] applying an approach similar to that reported by Basirat et al. [19] combining a physically based model with CDM. The evolution of the variables included in the model, such as the dislocation densities, glide velocity, effective stress on dislocation, internal stress from the microstructure, subgrain size, pressure on the subgrain boundaries and softening parameters is deeply analysed.

2. Experimental data and methods

The experimental data of steel grade P92 was selected for the purpose of modelling. Creep curves, dislocation densities, subgrain size and precipitation state (type, mean radius) were discussed in the work of Ennis et al. [21] and used in our work.

Additionally, we determined the number density (m^{-3}) of precipitates, not included in [21], simulating the heat treatment for the given chemical composition with the MatCalc software. MatCalc simulates the precipitation evolution based on a Wagner-Kampmann-type model, including (i) classical nucleation theory and (ii) growth/shrinkage/coarsening/composition change based on maximum energy dissipation [22–24]. The parameters used for the MatCalc simulation are given in Table 1. The precipitates considered for the MatCalc simulation were $M_{23}C_6$ carbides, $MX_{Austenite}$ (carbonitrides formed in austenitic matrix) and $MX_{Martensite}$ (carbonitrides formed in martensitic matrix). Laves phase and modified Z-phase were not considered for the simulation because they have not been found experimentally in as received condition [21]. We assumed that the as received condition did not change during creep, although in the literature it is reported that both phases form in P92 only during ageing or creep exposure [24]. Laves phase precipitates form after 100 h and a considerable amount of Z-phase forms after 100,000 h [24].

The numerical simulations to model the creep strain (Eq. (9)) were carried out using Matlab software. The mean radius and number density of $M_{23}C_6$ obtained from MatCalc were taken as input parameters for accounting the Zener drag pressure (see Eqs. (6) and (7)). The constants and the model parameters used for the numerical simulations are provided in Appendix A.

Table 1
Parameters used for the MatCalc simulation.

Thermodynamic database	mc_fe_v2.016.tdb
Mobility database	mc_fe_v2.001.ddb
Grain diameter of austenite	60×10^{-6} (m)
Subgrain diameter of martensitic	0.4×10^{-6} (m)
Dislocation density in austenite	1×10^{11} (m^{-2})
Dislocation density in martensite	0.7×10^{15} (m^{-2})
Nucleation sites for $M_{23}C_6$	Grain boundaries, subgrain boundaries
Nucleation sites for $MX_{Austenite}$	Grain boundaries
Nucleation sites for $MX_{Martensite}$	Dislocations, grain boundaries, subgrain boundaries

3. Model formulation

3.1. Description of the microstructure

P92 is a complex 9% Cr steel in which $M_{23}C_6$ (M=Cr and Fe) carbides are decorated along the prior austenitic grain boundaries, packet, block and subgrain boundaries. Additionally, MX-type (M=V, Nb and X=C, N) fine carbonitrides are spread throughout the matrix. Fig. 1 illustrates the microstructure of grade P92 steel in tempered condition, where different boundaries and precipitates are shown. The arrangement of different dislocations is assumed to be as shown in Fig. 1(c). The total dislocation density in the martensitic steels was therefore divided into three categories: (1) mobile dislocations ρ_m, which are free to glide under the application of a load; (2) dipole dislocations ρ_{dip}, which form dipolar or multipolar bundles; and (3) boundary dislocations ρ_b forming subgrain boundaries arranged in low energy configurations. Corresponding details can be found in the literature [10–13,19].

When materials are loaded at high temperatures with an applied stress σ_{app}, the microstructure evolves due to diffusional and relaxation processes. The glide and climb of the dislocations play important roles in the relaxation processes that occur during the dislocation creep. The microstructural evolution can be described by means of interactions such as: (a) multiplication of dislocations (Frank-Read sources), (b) immobilization of dislocations at subgrain boundaries, (c) annihilation of dislocations and (d) subgrain growth. These mechanisms were taken into account for the modelling.

The initial dislocation densities were set to $\rho_m = 7 \times 10^{14}$, $\rho_{dip} = 1 \times 10^{14}$ and $\rho_b = 2 \times 10^{14}\ m^{-2}$, while a subgrain radius of 0.2 μm was chosen for the numerical simulation [21]. The partitioning of different dislocation densities was based on results reported in the literature for tempered martensite [19,25]. The fraction of dipole dislocations that are close to the subgrain boundary and transform to boundary dislocations was assumed to be 7 times less than the mobile dislocation density for simulation purposes.

3.2. Glide velocity, effective stress and internal stress

Once an external load is applied to a material at high temperature, the mobile dislocations start to move. According to Ghoniem et al. [10], the average glide velocity v_g of the mobile dislocations can be expressed as:

$$v_g = a_1 \cdot \exp[-Q/kT][\Omega/kT]\sigma_{eff} \tag{1}$$

where Q is the activation energy for dislocation glide, k the Boltzmann constant, T the temperature, Ω the atomic volume, a_1 an adjustable parameter and σ_{eff} the effective stress. The effective stress is defined as the remaining amount of the applied stress σ_{app} available for the creep deformation and responsible for the movement of mobile dislocations over thermal barriers [9]. The expression is given as:

$$\sigma_{eff} = \sigma_{app} - \sigma_i \tag{2}$$

where σ_i describes the long-range internal stress provided by the microstructure that acts against the applied stress [26]. The internal stress has been considered differently by various researchers in the creep community. Salazar et al. [27] and Ghoniem et al. [10] used the contribution of dipoles and precipitates to describe the internal stress. Barkar et al. [9] used the mobile dislocations and precipitates to simulate internal stress in the soft region of the material. Basirat et al. [19] took into account the

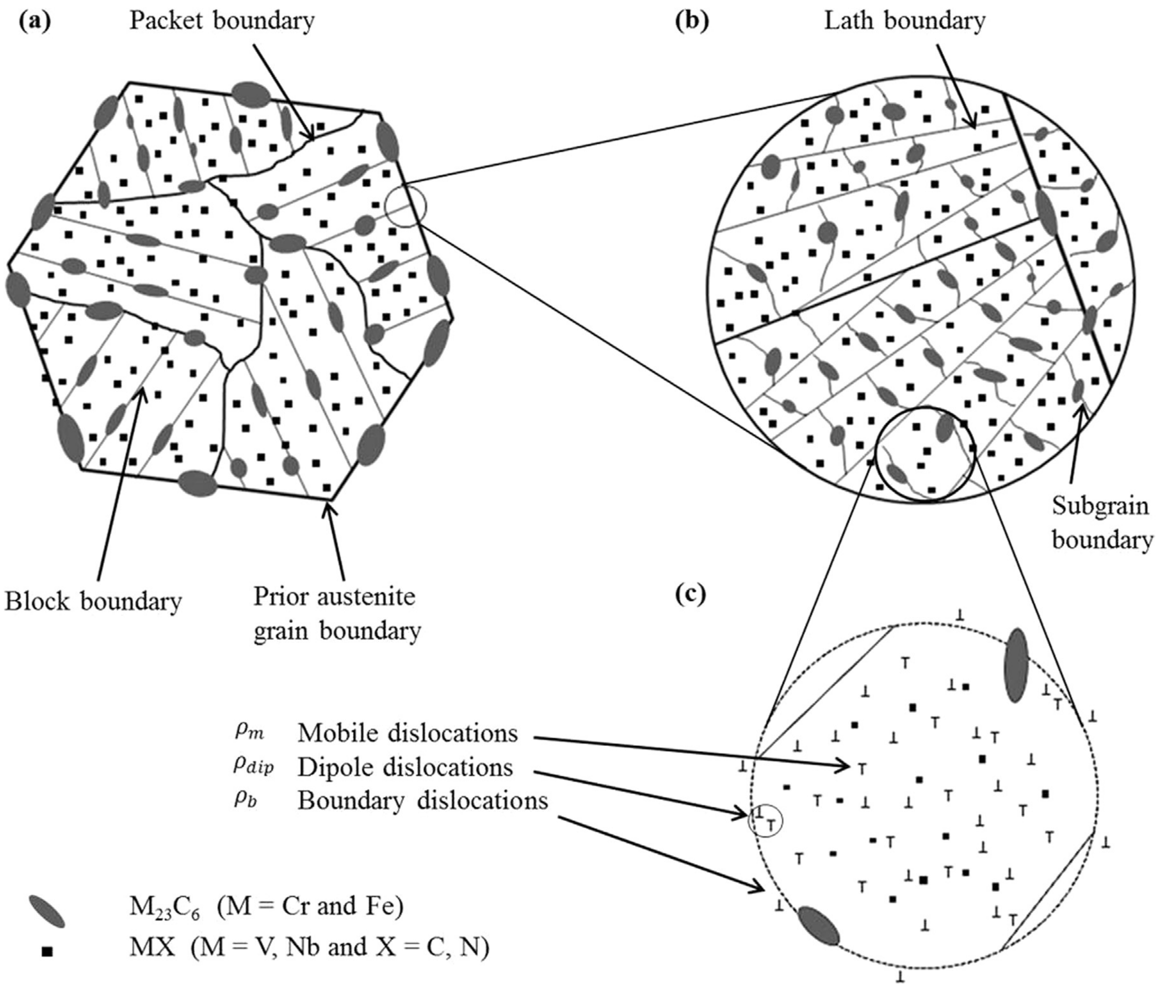

Fig. 1. Sketch of the microstructure of grade P92 steel after tempering, illustrating the different types of boundaries and precipitates (a) (b); and arrangement of dislocations in a subgrain (c).

contribution of the mobile dislocations as well as dipoles, to model internal stress. Using the same approach as in [19], the expression to describe counteracting internal stress evolving from the microstructure, which opposes the creep deformation, is given as:

$$\sigma_i = \alpha \mathrm{MGb}\sqrt{\rho_m + c_{\mathrm{dip}}\,\rho_{\mathrm{dip}}} \tag{3}$$

where α is a constant, M the Taylor factor, b the burgers vector, c_{dip} in our interpretation refers to stress fields of dipoles that is only 30% of the stress field of mobile dislocations while Basirat et al. [19] mentioned it as a weight factor and G the shear modulus of the material. The boundary dislocations have negligible contribution to the internal stress since they are configured into low energy positions [10].

3.3. Dislocation density evolution

The rate of change of mobile dislocation density during creep is described as a production term due to the multiplication of mobile dislocations minus consumption terms due to immobilization at subgrain walls, climb recovery and dynamic recovery [10–13]:

$$\frac{d\rho_m}{dt} = \left[\frac{v_g}{h_m}\cdot\rho_m\right] - \left[\frac{v_g}{2R_{sbg}}\cdot\rho_m\right] - \left[8{\rho_m}^{3/2}v_c\right] - \left[d_{anh}\cdot(\rho_m + \rho_{dip})\cdot\rho_m\cdot v_g\right] \tag{4}$$

In Eq. (4), R_{sbg} is the mean subgrain radius, h_m the dislocation spacing of mobile dislocations and considered to be equal to $1/(\rho_m)^{0.5}$ [3], v_c the climb velocity of dislocation [10] and d_{anh} the length parameter for spontaneous annihilation [10–13]. Based on literature our first approach was presented in ECCC 2014 [20], simplifying some parameters. In present model we did not take into account the term related to the emission of dislocations from the subgrain wall because it is negligible.

Similarly, the rate of change of the dipole dislocation density can be expressed as a production term, due to the immobilization of mobile dislocations close to subgrain walls minus two annihilation terms that describe the transformation of the dipole dislocations into boundary dislocations and the annihilation by dynamic recovery when a mobile dislocation with opposite sign approaches [10–13]:

$$\frac{d\rho_{dip}}{dt} = \left[\frac{v_g}{2R_{sbg}}\cdot\rho_m\right] - 8\left[\frac{v_c}{h_b}\cdot\rho_{dip}\right] - \left[d_{anh}\cdot\rho_{dip}\cdot\rho_m\cdot v_g\right] \tag{5}$$

The dislocation spacing within the subgrain walls h_b can be correlated with the dislocation densities as $h_b = 1/[(\rho_{dip}+\rho_b)R_{sbg}]$ [10].

The evolution rate of boundary dislocation density can be described by the transformation of dipole dislocations into boundary dislocation minus two annihilation terms due to the loss of dipoles while transforming into boundary dislocations, and the formation of new subgrain surfaces [10–13]:

$$\frac{d\rho_b}{dt} = 8\left[\frac{v_c}{h_b}\cdot\rho_{dip}\right] - \zeta\left[\frac{v_c}{h_b}\cdot\rho_{dip}\right] - M_{sb}\cdot\left[P_{sb} - 2\pi\cdot\left(\sum_{i=1}^{n} r^2_{mean,i}\cdot N_{v,i}\right)\cdot\gamma\right]_{sb}\frac{\rho_b}{R_{sbg}} \tag{6}$$

In the formation of new subgrain surface due to subgrain growth we took into account the mobility of this subgrain M_{sb}, its pressure $P_{sb}=4Gb^2\rho_b/3$, and the Zenner drag effect of precipitates on the boundaries. Therefore, $i=1, 2, 3..n$ refers to the type of precipitates, $\zeta=0.25$ is a constant that accounts for the fraction of dipoles that annihilate when transforming to boundary dislocations, r_{mean} is the mean radius of precipitates, N_v the number density of the precipitates and $\gamma_{sb}=Gb^2\rho_b R_{sbg}/3$ the surface energy of the subgrain boundary [10].

3.4. Subgrain growth

In martensitic steels, the formation of dislocation cells and subgrains takes place during high temperature deformation [10,26,28]. The dislocation dynamics simulation performed by Amodeo et al. [29] showed that subgrains form to minimize the elastic energy of the system [29,30]. Thus, the subgrains evolution is incorporated in the model. Considering the Zener drag caused by the presence of precipitates, the growth rate of subgrains is expressed as [10–13]:

$$\frac{dR_{sbg}}{dt} = M_{sb}\left[P_{sb} - 2\pi\cdot\left(\sum_{i=1}^{n} r^2_{mean,i}\cdot N_{v,i}\right)\cdot\gamma_{sb}\right] \tag{7}$$

The term that is related to shrinkage by subgrain nucleation is not considered because it is negligible.

3.5. Creep strain

The macroscopic creep strain rate can be defined using Orowan's equation, in terms of mobile dislocation density and average glide velocity of mobile dislocations [10–13,19,20]:

$$\frac{d\varepsilon}{dt} = \frac{b}{M}\cdot\rho_m\cdot v_g \tag{8}$$

The creep rate increases due to the depletion of solid solution elements, coarsening of precipitates and cavitation [19]. Once the precipitation of the Laves phase begins, it consumes Mo, W, or both from the respective matrix [6], although this effect has been reported to be small in grade P92. On the other hand, laves phase can also contribute to precipitate hardening. Since there is a balance between strength lost due to solid solution depletion and strength gained due to the precipitation hardening of laves phase in the beginning [31], the softening due to solid solution depletion is ignored. Considering the softening caused by the coarsening of the precipitates ($M_{23}C_6$ and MX) and cavitation, Orowan's equation can be modified through softening parameters. Using the CDM approach [19], the modified Orowan's equation can be written as,

$$\frac{d\varepsilon}{dt} = \frac{b\cdot\rho_m\cdot v_g}{M\cdot(1-D_{ppt})\cdot(1-D_{cav})} \tag{9}$$

where D_{ppt} is a softening parameter related to the coarsening of $M_{23}C_6$ and MX precipitates and D_{cav} is a softening parameter based on the cavitation damage. The values of both softening parameters lie between zero and one. The value of softening parameter is zero for no softening and one when the material fractures. This coupling of a physical model (Eqs. (1)–(8)) with CDM resulted in Eq. (9) and that allows modelling the creep curve up to the onset of tertiary creep.

3.5.1. Softening due to coarsening of precipitates

The $M_{23}C_6$ precipitates are known for their pinning effect on subgrain boundaries [4]. On the other hand, fine MX carbonitrides impede the movement of dislocations inside the subgrain. In general, the number density of precipitates decreases during creep due to their coarsening, thus provoking softening of materials during creep [4,9,32]. Considering the primary coarsening mechanisms, namely, the volume diffusion in the case of $M_{23}C_6$ carbides and pipe diffusion in the case of MX carbonitrides, the softening parameter rate [17–19,33] based on coarsening of i_{th} precipitate can be described by:

$$\dot{D}_{(ppt),i} = \frac{k_p}{(l-1)}\cdot\left(1-D_{(ppt),i}\right)^l \tag{10}$$

For MX-type precipitates $l=6$ and for $M_{23}C_6$ $l=4$, k_p is a constant normalized with $(l\text{-}1)^{th}$ power of initial size of the precipitates that depends on the type of precipitates, temperature and stress [32,33].

The total softening produced due to the coarsening of all type of precipitates $i=1, 2, 3\ldots n$ inside the material is then defined as:

$$D_{ppt} = \sum_{i=1}^{n}\left(D_{(ppt),i}\right) \tag{11}$$

In our work both $M_{23}C_6$ and MX precipitates were taken into account to calculate the coarsening damage parameter.

3.5.2. Cavitation softening

It has been shown both experimentally and theoretically by many researchers that grain boundaries are prone to cavitation. The combination of precipitates (Laves phase and $M_{23}C_6$ carbides) and grain boundaries make the cavitation more pronounced [34–37]. Thus, a fair assumption for the model is that cavities nucleate along high angle grain boundaries. The approach used by several researchers [16,17,19] to define the softening parameter for cavitation is also used here:

$$\dot{D}_{cav} = (A\cdot\varepsilon\cdot\dot{\varepsilon}) \tag{12}$$

where A is a parameter that depends on the material, temperature and stress.

4. Results and discussions

The results obtained from the MatCalc simulation such as number densities and mean radii of the precipitates $M_{23}C_6$, $MX_{Austenite}$ and $MX_{Martensite}$ in the starting condition are given in Table 2. The results have shown good agreement with the data reported by Ennis [21] in terms of mean radius and with [24] in terms of the mean radius and number density. The mean radius and number density of $M_{23}C_6$ were used in Eqs. (6) and (7) for accounting the Zener drag pressure.

4.1. Creep strain and the evolution of dislocation densities

Figs. 2a, c and e and 3a and c depict the experimental and simulated creep curves at 650 °C and 600 °C, respectively. The modelled creep curves show good agreement with the experimental curves up to the onset of the tertiary creep stage. The evolution of dislocation densities associated to a particular creep

Table 2
Information about precipitates in tempered grade P92 steel obtained from MatCalc© calculations.

Precipitates	Mean radius (nm)	Number density (m^{-3})
$MX_{Martensite}$	6	3.0×10^{21}
$MX_{Austenite}$	22	1.2×10^{16}
$M_{23}C_6$	40	6.0×10^{19}

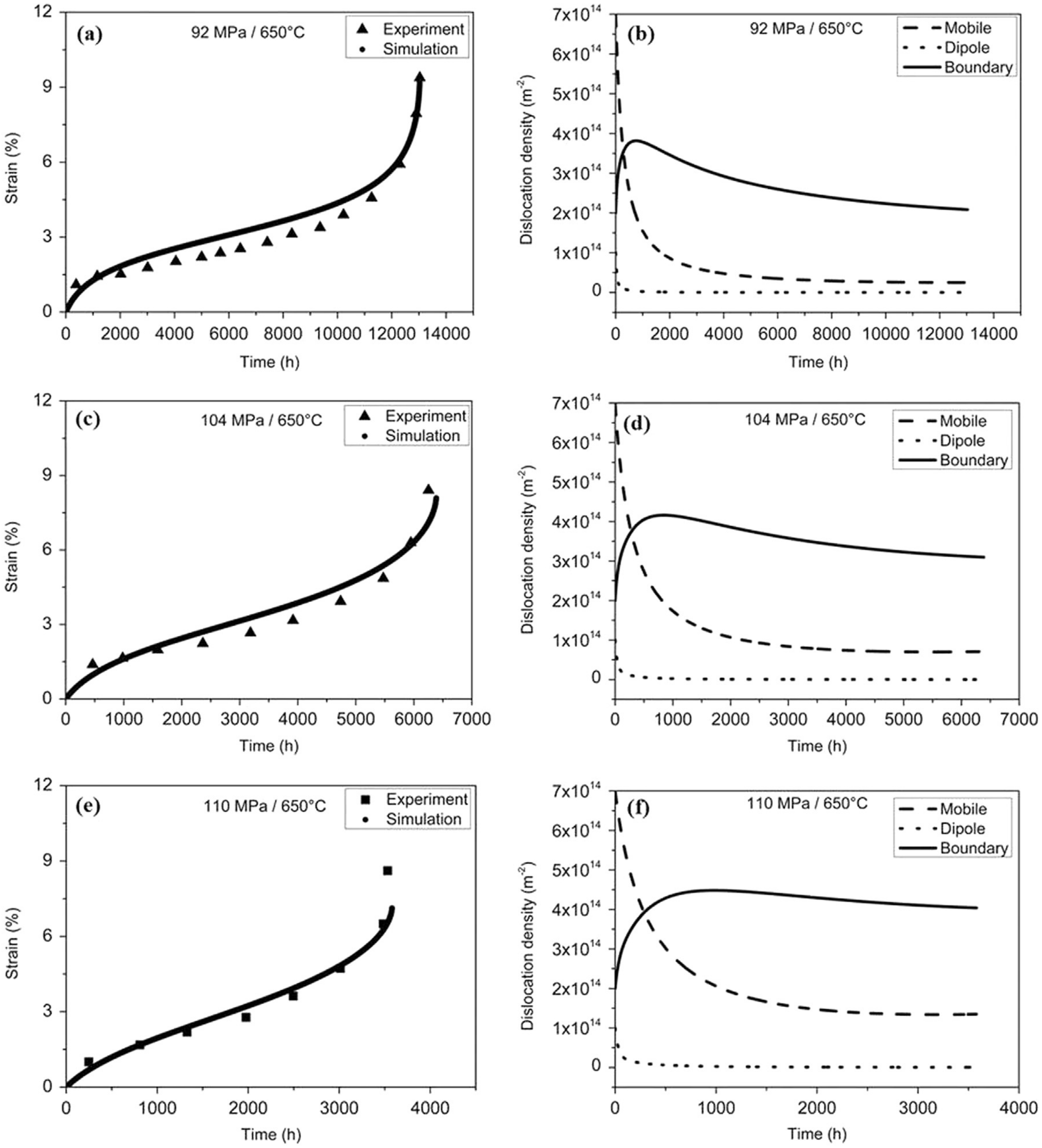

Fig. 2. Modelled vs. experimental creep curves at 650 °C and three different stress levels (a) (c) (e); and the corresponding evolution of the three types of dislocation densities (b) (d) (f).

curve is plotted besides each creep curve. Figs. 2b, d and f and 3b and d depict the simulation results, showing the evolution of mobile, dipole and boundary dislocation densities as a function of time at 650 °C and 600 °C, respectively.

The initial mobile dislocation density is high in all the cases and decreases with exposure time due to the annihilation and formation of dipoles. These newly produced dipoles and the pre-existing dipoles are annihilated as well as transformed into boundary dislocations during the creep exposure. Thus, the boundary dislocation density increases at the beginning as dipoles are formed at the boundaries and are transformed to boundary dislocations. By increasing the strain, the boundary dislocation density decreases due to subgrain growth [9]. A steady state is nearly achieved for the three dislocation density types under all conditions after some time (see Figs. 3b, d and f and 4b and d). The production rates of dislocations are high at higher stresses, thus resulting in higher dislocation densities [32]. The evolution behaviour is similar for both temperatures (650 °C and 600 °C) and the differences in magnitude are due to the different loading conditions.

Experimental observations have shown that the initial mobile dislocation density is high in the case of tempered martensitic/ferritic steels. The mobile dislocation density decreases very rapidly during the primary creep [18,38]. This density of mobile dislocation has been reported to be ten times lower as compared to the as received condition, dropping from the order of 10^{14} to $10^{13}\,m^{-2}$ [18]. The initial increment in boundary dislocation densities has been also reported in the literature [14]. A plateau is nearly achieved when the production rate of dislocations approaches the value of the recovery rate [25,38]. Our results indicate that the recovery rate is high at the beginning of creep and slows down with time.

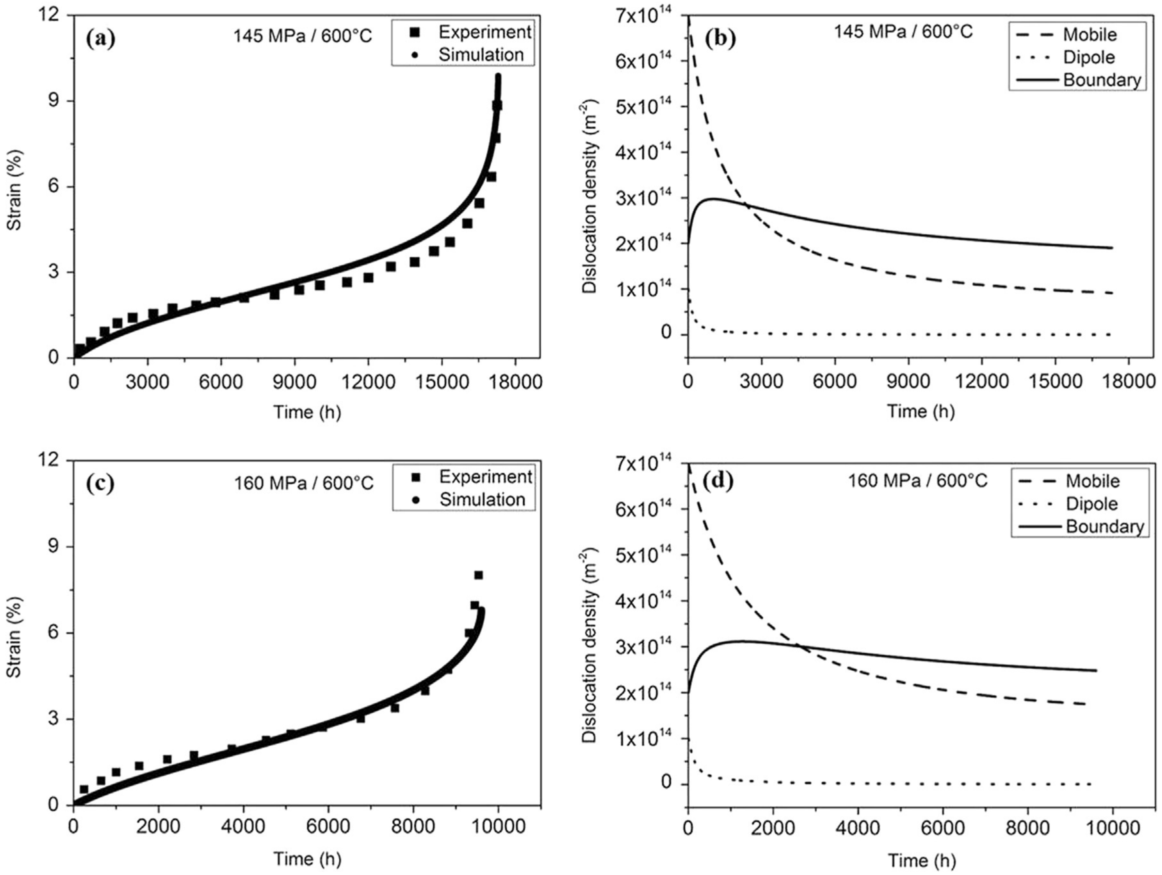

Fig. 3. Modelled vs. experimental creep curves at 600 °C and two different stress levels (a) (c); and the corresponding evolution of the three types of dislocation densities (b) (d).

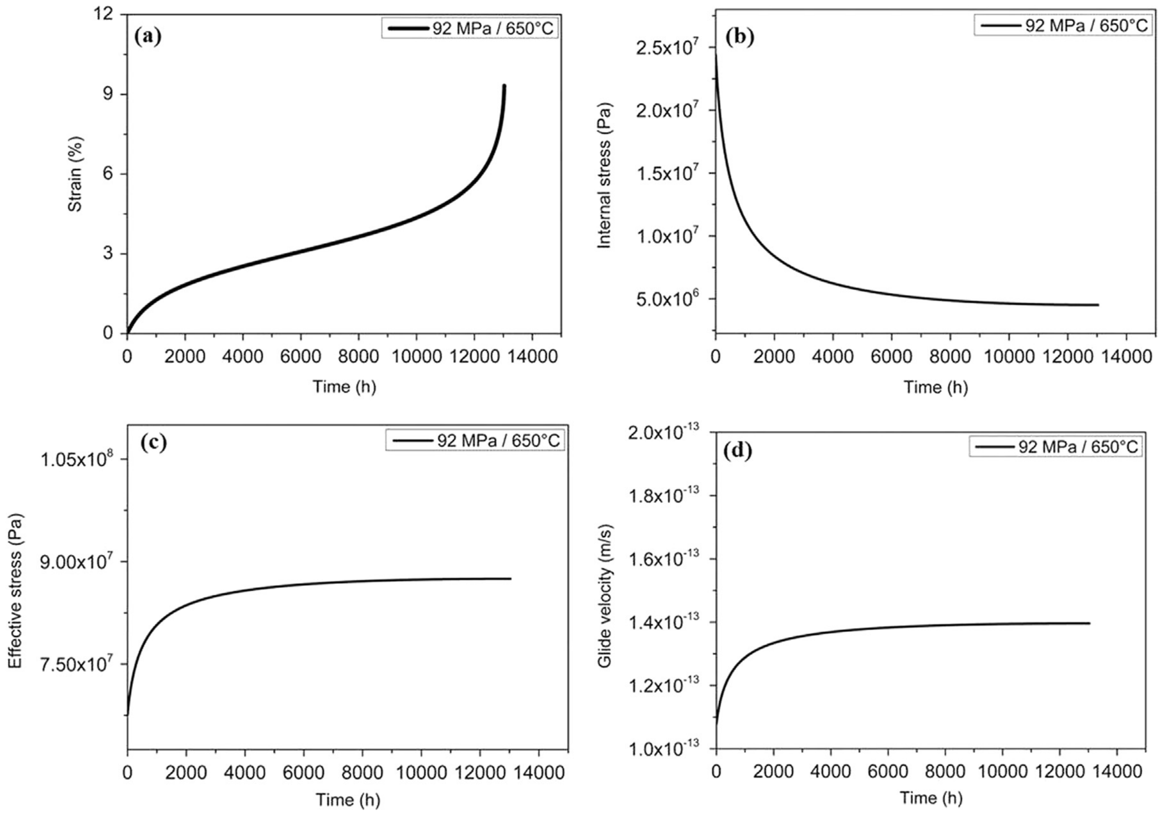

Fig. 4. Simulated creep strain (a); σ_i (b); σ_{eff} (c); ν_g (d); at 650 °C/92 MPa.

4.2. Internal stress, effective stress and glide velocity

The evolution of internal stress, effective stress and glide velocity are depicted in Fig. 4 with reference to the creep curve at 650 °C. The internal stress due to the microstructure depends on the mobile and dipole dislocation densities (Eq. (3)). Initially, the mobile and dipole dislocation densities are high, resulting in high levels of internal stress. Both dislocation densities decrease as the creep deformation proceeds and the internal stresses nearly reaches a steady state (see Figs. 2b, d and f and 3b and d). Thus, the internal stress that opposes the motion of dislocations is high in the beginning and drops as creep continues (see Fig. 4b). Since in creep conditions the applied stress is constant, the effective stress increases up to a certain level where steady state takes place (see Fig. 4c). Finally, from Eq. (1), it can be seen that the average glide velocity of the mobile dislocations is directly proportional to the effective stress, and therefore it increases with the same tendency as the effective stress (see Fig. 4d).

The calculated glide velocity based on minimum creep rate at 600 °C/80 MPa in similar kind of a steel grade P91, is reported to 2×10^{-15} m/s [39]. In another study conducted at 738 °C/5.3 MPa, the mean glide velocity was evaluated by in-situ TEM in a Fe-Mo alloy and was reported 2.3×10^{-8} m/s [40]. The difference in the glide velocity is due to differences in chemical composition, testing temperatures and the levels of applied stresses [39]. Our model predicts the glide velocity on an order of 10^{-13} to 10^{-14} m/s at 650 °C and 600 °C, respectively. Our results also show that the glide velocity does not remain constant during the creep exposure, in agreement with observations made on solid solution alloys [41]. This means that with the progressive creep strain, the materials become softer and effective stress on the mobile dislocations as well as average glide velocity of the mobile dislocations increases. The glide velocity has significant role in evaluation of creep rate (Eq. 9) and its evolution during creep can be determined from the model.

The effect of applied stress on variables such as internal stress, effective stress and glide velocity is depicted in Fig. 5 at two different temperatures (650 °C and 600 °C). All the three variables

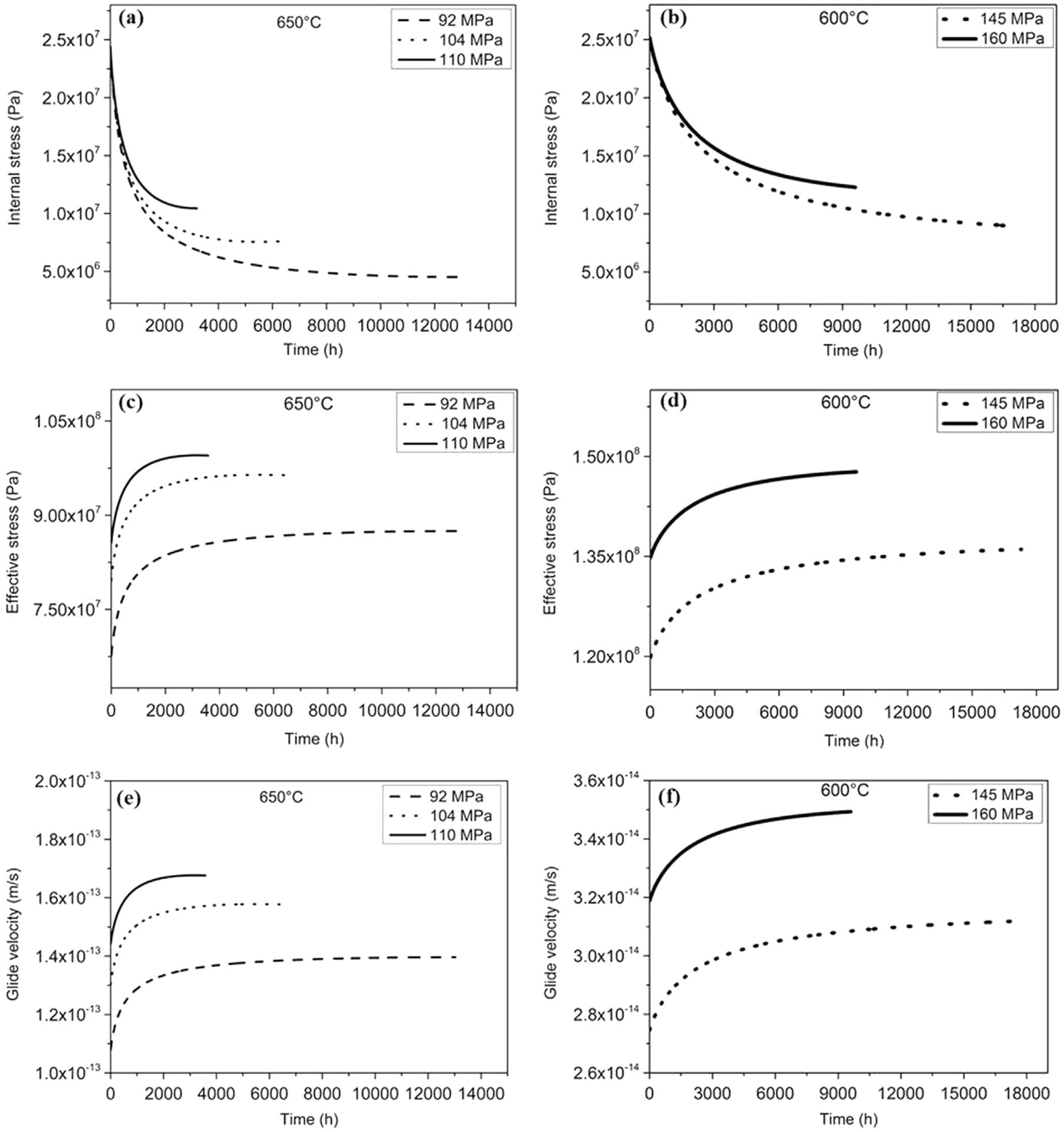

Fig. 5. Evolution of σ_i, σ_{eff} and v_g as a function of σ_{app} at 650 °C and 600 °C.

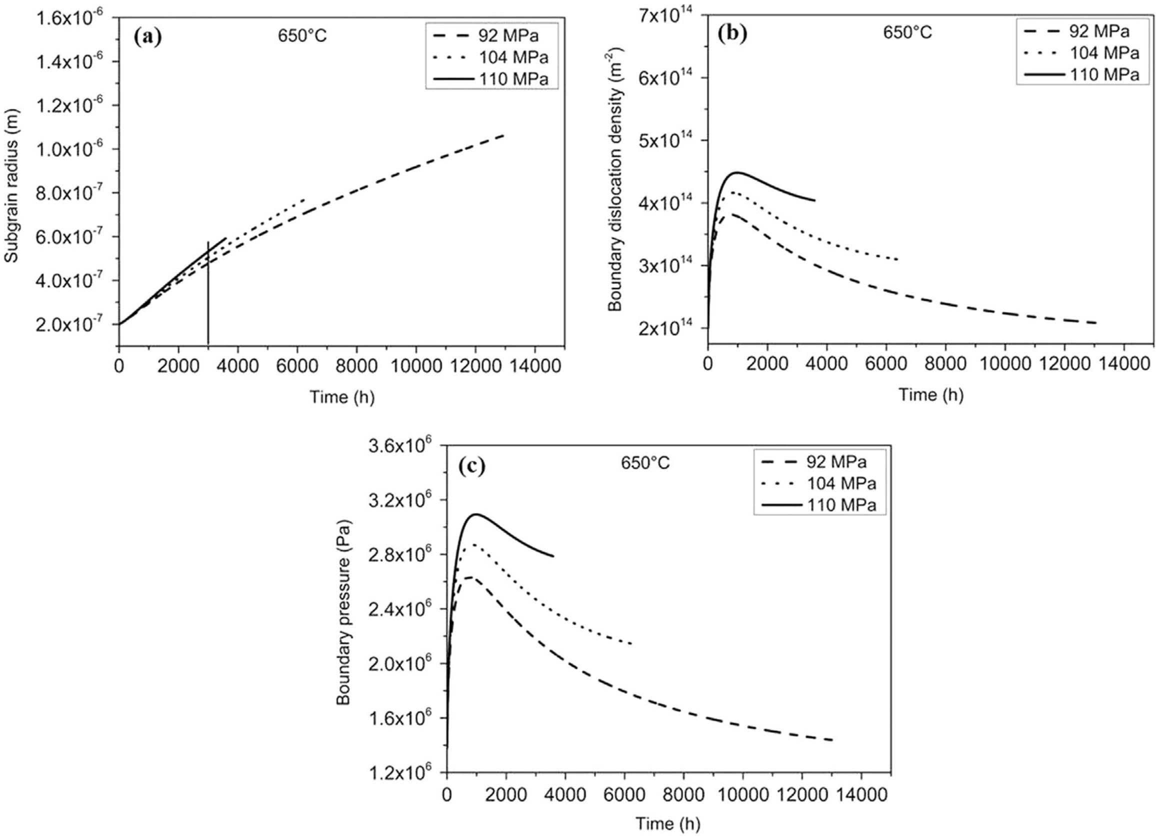

Fig. 6. Simulation results showing the effect of applied stress on subgrain size (a); boundary dislocation density (b); boundary pressure (c) at 650 °C.

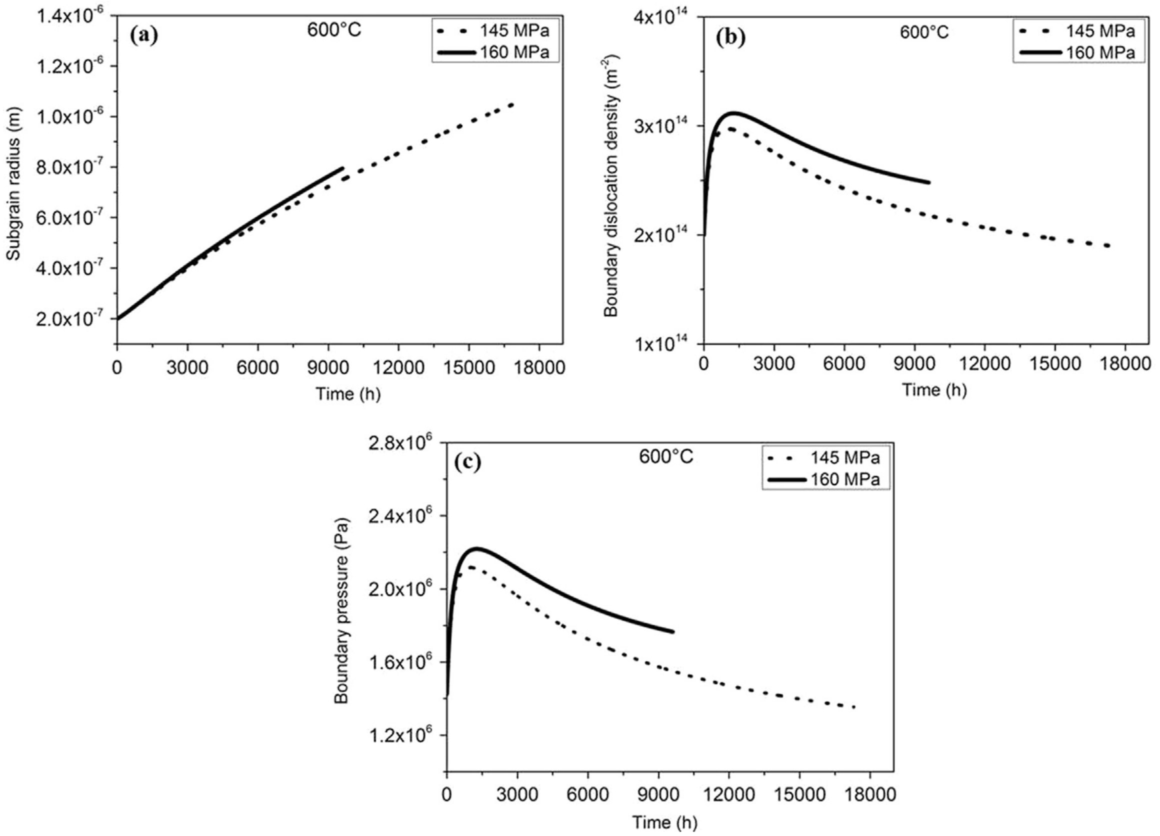

Fig. 7. Simulation results showing the effect of applied stress on subgrain size (a); boundary dislocation density (b); boundary pressure (c) at 600 °C.

show higher values at higher applied stress levels at both temperatures (see Figs. 5a, c and e for 650 °C and Figs. 5b, d and f for 600 °C). The production rates of the dislocations are high at higher stress levels resulting in high internal stresses as well. Since the effective stress and the glide velocity are directly influenced by the applied stress, they also show high values at higher stress levels.

4.3. Effect of applied stress on subgrain size and boundary dislocations

The effects of applied stress on subgrain size, boundary pressure and boundary dislocation density are shown in Figs. 6 and 7, for 650 °C and 600 °C, respectively. Fig. 6a illustrate that subgrains are the largest at 110 MPa, when comparing at a constant time (i.e 3000 h, marked with vertical line in Fig. 6a).

This finding agrees with the empirical relationships described for subgrains [32,42,43]. This means that the growth rate of subgrains is high at higher stress levels due to higher creep rates. The specimens fail early at higher stress levels due to localised damage, and the remaining subgrain size in a broken sample is smaller at higher stress levels as compared to that of fractured samples tested under lower stress levels. The production rates of dislocations are high at high stress levels. Therefore, at a given creep time, the boundary dislocation density has larger values, resulting in higher boundary pressure. The observations at 600 °C also reveal similar evolution behaviour of these variables under different stress conditions (see Fig. 7). The differences in magnitude are due to the different loading conditions.

The results from our simulations are compared with the experimental data from [21], as shown in Tables 3 and 4 at 650 °C and 600 °C. The model predicts lower values of mobile dislocation densities and high values of subgrain radii at both temperatures as compared to the reported experimental data (see Tables 3 and 4). Although the calculated values are within the experimental order of magnitude, some underestimation of the mobile dislocation density and overestimation of the subgrain size is done by our model since interactions between fine $MX_{\mathrm{Martensite}}$ precipitates and mobile dislocations have not been considered. These fine $MX_{\mathrm{Martensite}}$ precipitates impede the dislocation movements and reduce the recovery rate. Thus, disregarding them will increase the recovery rate in the model predictions (as sketched in Fig. 8).

4.4. Softening parameters

The evolution of both softening parameters, cavitation D_{cav} and precipitate coarsening D_{ppt}, are depicted in Fig. 9 at different temperatures and stresses. In general, the specimen reaches ultimate state of the damage when the softening parameter due to cavitation reaches a value of 1, meaning that the specimen is broken.

The parameters (a_1, k_p and A) were adjusted to achieve a value 0.95 for the cavitation softening parameter, which is very close to that of a fracture. Experimentally it has been shown that k_p depends on the applied stress [43]. Considering the starting values of k_p from literature [18,43] and following the Basirat's approach [19], values were adjusted for different conditions. The starting values of A were taken from the work of Basirat et al. [19] and then adjusted for different creep conditions. From Fig. 9a and c, it can be observed that the cavitation softening parameter reaches higher values more quickly at higher stress levels at both temperature 650 °C and 600 °C.

At constant temperature the specimens exposed to higher stresses failed early compare to low stresses. Although the coarsening rate is high at high stress, due to early failure of specimen, the precipitates remain smaller compare to low stress tested specimens. Thus, the precipitates are coarser in specimens that have been exposed for longer periods of time at lower stresses. The softening rate is also high at higher stresses due to high coarsening rate, but the specimens fail early due to localised damage at higher stresses and final values of this softening parameter remains smaller compare to low stresses. Fig. 9b and d depict that the softening parameter due to precipitate coarsening has a larger value in specimens that have been exposed for longer periods of time (i.e., at low stress levels) at both temperatures 650 °C and 600 °C. This parameter has the lowest value at the highest stress level and shortest exposure time.

The combination of softening parameters due to cavitation and precipitation allows modelling the creep curves of P92 up to the onset of tertiary creep regime in different loading conditions.

Table 3
Subgrain size and mobile dislocation density at 650 °C.

Stress (MPa)	Simulation			Experiment [21]
	92	104	110	104
Mobile dislocation density (m^{-2})	0.25×10^{14}	0.71×10^{14}	1.35×10^{14}	3.3×10^{14}
Subgrain radius (m)	1.07×10^{-6}	0.78×10^{-6}	0.59×10^{-6}	0.6×10^{-6}

Table 4
Subgrain size and mobile dislocation density at 600 °C.

Stress (MPa)	Simulation		Experiment [21]
	145	160	160
Mobile dislocation density (m^{-2})	0.91×10^{14}	1.74×10^{14}	2.5×10^{14}
Subgrain radius (m)	1.1×10^{-6}	0.8×10^{-6}	0.7×10^{-6}

5. Conclusions

Creep curves of grade P92 steel were modelled up to the onset of tertiary creep stage using a hybrid approach. In this approach, a physical model based on dislocation interactions and subgrain evolution was developed and coupled with CDM approach. Unlike merely fitting the creep curves, the model also predicted the evolutions of dislocation densities, effective stress on dislocations, internal stress, glide velocity, subgrain size and pressure on subgrain boundaries during the creep. The comparison with experimental data shows good agreement in terms of creep curves, mobile dislocation density and subgrain size after creep. The evolution behaviour of mobile dislocation density and subgrain size predicted from the model is in agreement with empirical relationships reported in the literatures [32,42,43].

We conclude that:

- The recovery rate is high at the beginning of creep and slows down with time.
- With on-going creep, material becomes softer and effective stress and glide velocity increases up reaching near steady state.
- The effective stress and the glide velocity increases with increasing the stress levels.
- The production rates of dislocations are high at higher stress levels resulting in higher internal stresses and boundary pressures.
- The higher applied stress, the faster growth rate of subgrains. However, due to the early failures at higher stresses, subgrain sizes of broken samples are smaller compared to that obtained in samples fractured after low stresses.

In the present form our model can be applied to 9–12% Cr

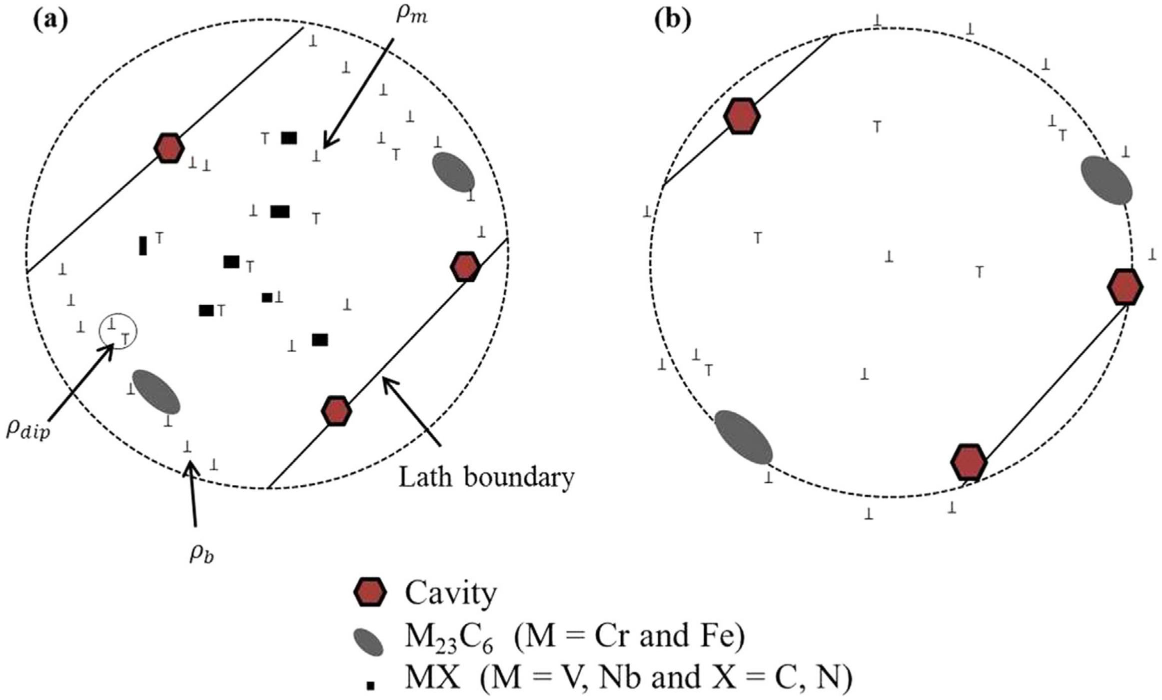

Fig. 8. Sketch illustrating the microstructure after creep (a) real situation; (b) model prediction: underestimation of mobile dislocation density and overestimation of subgrain size.

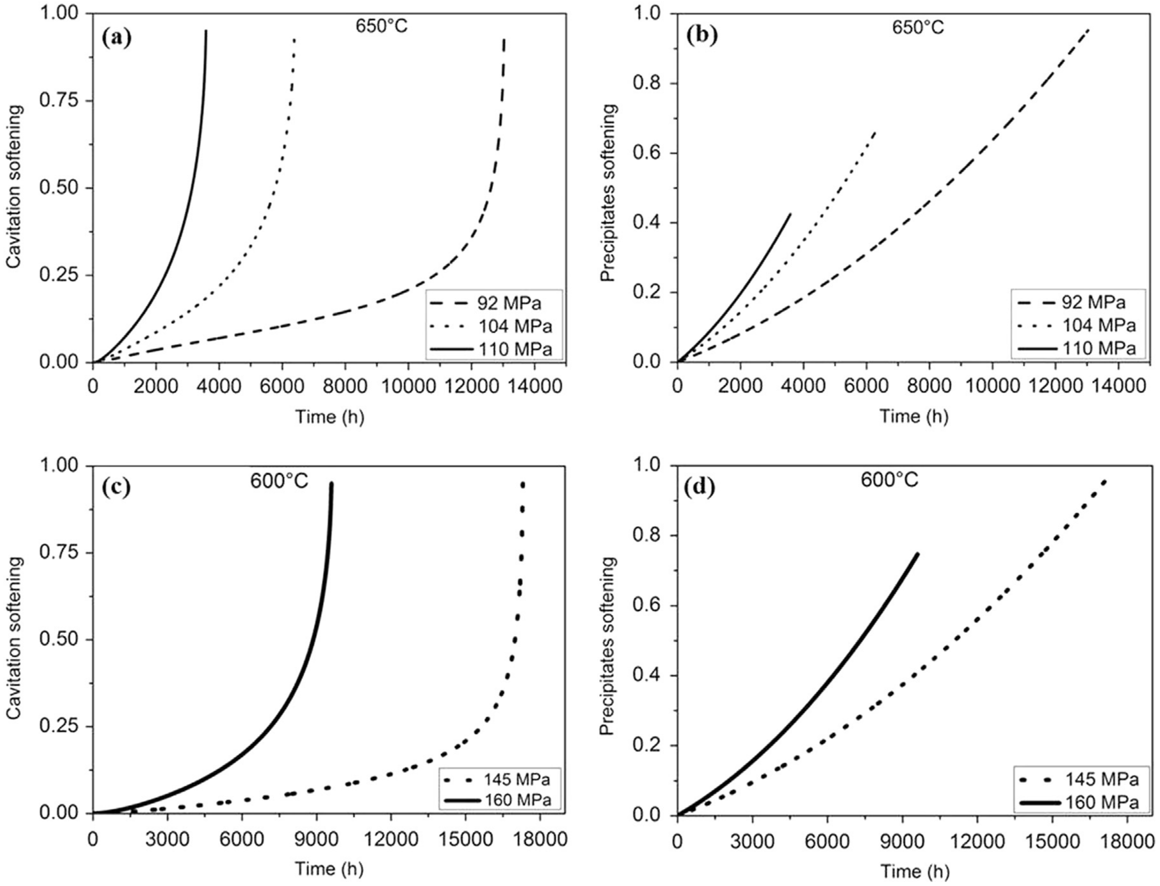

Fig. 9. Simulation results showing the evolution of softening parameters at 650 °C cavitation (a); precipitate coarsening (b); and at 600 °C cavitation (c); precipitate coarsening (d).

martensitic ferritic steels. The model is pedigree to the earlier hybrid models where the behaviour of subgrains was not included and merely creep curves were fitted. Together with creep curves the model is capable to determine the evolution of internal variables:

- Mobile and dipole dislocation densities decrease and subgrains coarsen during creep.
- Boundary dislocation density increases at the beginning of the creep and decreases afterwards due to subgrain growth.

The future work is going to couple the model with the precipitate kinetic simulations during creep to get rid of the softening parameter based on precipitates coarsening.

Acknowledgments

This research work was carried out within the project Z-Ultra: 309916, “Z phase strengthened steels for ultra-supercritical power plants”. The authors thank the European commission for the financial support. Special thanks to Romain Bureau for his valuable discussions.

Appendix A

Material parameters from theory/experiments.

$G=63\times10^{9}$ at 650 °C	Shear modulus [Pa]	Ref. [44]
$G=65\times10^{9}$ at 600 °C		
$b=2.866\times10^{-10}$	Burgers vector [m]	Ref. [12]
$M=3$	Taylor's factor	Ref. [19]
$k=1.3806504\times10^{-23}$	Boltzmann constant [J/K]	Ref. [12]
$\Omega=1.149404032\times10^{-29}$	Atomic volume [m^3]	Ref. [12]
$d_{anh}=3\times10^{-9}$	Length parameter [m]	Ref. [19]
$M_{sb}=1.16\times10^{-20}$ at 650 °C	Mobility of subgrain boundaries [mP a^{-1} s^{-1}]	Ref. [10]
$M_{sb}=0.9\times10^{-20}$ at 600 °C		
$c_{dip}=0.3$	Weight factor	Ref. [19]

Adjustable model parameters at 600 °C.

Parameters		Stress (MPa)		Starting values from literature for 600 °C and 650 °C
		145	160	
k_p	$M_{23}C_6$	2.270×10^{-8}	3.440×10^{-8}	4.840×10^{-7} Ref. [43]
	MX	1.510×10^{-10}	2.320×10^{-10}	2.22×10^{-8} Ref. [18]
a_1		0.650×10^{2}	0.671×10^{2}	0.87×10^{2} Ref. [20]
A		1.930×10^{2}	4.252×10^{2}	1.45×10^{2} Ref. [19]

Adjustable model parameters at 650 °C.

Parameters		Stress (MPa)		
		92	104	110
k_p	$M_{23}C_6$	2.970×10^{-8}	4.840×10^{-8}	6.250×10^{-8}
	MX	1.960×10^{-10}	2.720×10^{-10}	3.020×10^{-10}
a_1		0.791×10^{2}	0.811×10^{2}	0.835×10^{2}
A		2.193×10^{2}	2.924×10^{2}	3.811×10^{2}

References

[1] Z. Ye, P. Wang, D. Li, Y. Zhang, Y. Li, Effect of carbon and niobium on the microstructure and impact toughness of a high silicon 12% Cr ferritic/martensitic heat resistant steel, Mater. Sci. Eng. A 616 (2014) 12–19.

[2] A. Chatterjee, D. Chakrabarti, A. Moitra, R. Mitra, A.K. Bhaduri, Effect of deformation temperature on the ductile-brittle transition behavior of a modified 9Cr–1Mo steel, Mater. Sci. Eng. A 630 (2015) 58–70.

[3] S.D. Yadav, J. Rosc, B. Sartory, R. Brunner, B. Sonderegger, C. Sommitsch, C. Poletti, Investigation of pre-existing pores in creep loaded 9Cr steel, in: D. Bernard, J.-Y. Buffière, T. Pollock, H. F. Poulsen, A. Rollett, M. Uchic (Eds.), Proceedings of the 2nd International Congress on 3D Materials Science, John Wiley and Sons, Inc., Hoboken, NJ, USA, 2014, http://dx.doi.org/10.1002/9781118990278.ch14.

[4] N. Dudova, A. Plotnikova, D. Molodov, A. Belyakov, R. Kaibyshev, Structural changes of tempered martensitic 9%Cr-2%W-3%Co steel during creep at 650 °C, Mater. Sci. Eng. A 534 (2012) 632–639.

[5] S.S. Wang, L. Chang, L. Wang, T. Wang, Y.D. Wu, J.J. Si, J. Zhu, M.X. Zhang, X. D. Hui, Microstructural stability and short-term creep properties of 12Cr-W-Mo-Co steel, Mater. Sci. Eng. A 622 (2015) 204–211.

[6] A. Kipelova, A. Belyakov, R. Kaibyshev, Laves phase evolution in a modified P911 heat resistant steel during creep at 923 K, Mater. Sci. Eng. A 532 (2012)

71–77.
[7] H.K. Danielsen, J. Hald, Behaviour of Z phase in 9–12% Cr steels, Energy Mater. 1 (2006) 49–57.
[8] H.K. Danielsen, P.E.D. Nunzio, J. Hald, Kinetics of Z-phase precipitation in 9–12% Cr steels, Metall. Mater. Trans. A 44A (2013) 2445–2452.
[9] T. Barkar, J. Ågren, Creep simulation of 9–12% Cr steels using the composite model with thermodynamically calculated input, Mater. Sci. Eng. A 395 (2005) 110–115.
[10] N. Ghoniem, J. Matthews, R. Amodeo, A dislocation model for creep in engineering materials, Res. Mech. 29 (1990) 197–219.
[11] F. Krumphals, T. Wlanis, C. Sommitsch, I. Holzer, B. Sonderegger, V. Wieser, Modelling of microstructure evolution in hot work tool steels during service, Comput. Methods Mater. Sci. 9 (2) (2009) 228–233.
[12] F. Krumphals, Physical Based Modelling of Creep Fatigue in Hot Work Tool Steels (Ph.D. thesis), Graz University of Technology, Austria, 2014.
[13] F. Krumphals, B. Reggiani, L. Donati, T. Wlanis, C. Sommitsch, Deformation behaviour of a ferritic hot-work tool steel with respect to the microstructure, Comput. Mater. Sci. 52 (2012) 40–45.
[14] H. Magnusson, R. Sandström, Creep strain modeling of 9–12% Cr steels based on microstructure evolution, Metall. Mater. Trans. A 38A (2007) 2033–2039.
[15] M. McLean, B.F. Dyson, Modeling the effects of damage and microstructural evolution on the creep behavior of engineering alloys, J. Eng. Mater. Technol. 122 (2000) 273–278.
[16] Y.F. Yin, R.G. Faulkner, Continuum damage mechanics modelling based on simulations of microstructural evolution kinetics, Mater. Sci. Technol. 22 (8) (2006) 929–936.
[17] S. Nandi, K.S.N. Vikrant, P. Ahv, K. Singh, R.N. Ghosh, Creep modelling of P91 steel for high temperature power plant applications, Procedia Eng. 55 (2013) 751–755.
[18] H. Semba, B. Dyson and the late M. McLean: microstructure-based creep modelling of a 9% Cr martensitic steel, Mater. High. Temp. 25 (3) (2008) 131–137.
[19] M. Basirat, T. Shrestha, G.P. Potirniche, I. Charit, K. Rink, A study of the creep behavior of modified 9Cr-1Mo steel using continuum-damage modelling, Int. J. Plast. 37 (2012) 95–107.
[20] S.D. Yadav, M. Schuler, C. Sommitsch, C. Poletti, Physical based creep strain modelling of 9Cr martensitic steel, in: Proceedings of ECCC, Rome, Italy, 2014.
[21] P.J. Ennis, A. Zielinska-Lipiec, O. Wachter, A. Czyrska-Filemonowicz, Microstructural stability and creep rupture strength of the martensitic steel P92 for advanced power plant, Acta Mater. 45 (12) (1997) 4901–4907.
[22] E. Kozeschnik, J. Svoboda, P. Fratzl, F.D. Fischer, Modelling of kinetics in multi-component multi-phase systems with spherical precipitates: II: numerical solution and application, Mater. Sci. Eng. A 385 (2004) 157–165.
[23] 〈http://matcalc.tuwien.ac.at/〉.
[24] B.S. Srinivas Prasad, V.B. Rajkumar, K.C. Hari Kumar, Numerical simulation of precipitate evolution in ferritic-martensitic power plant steels, Calphad 36 (2012) 1–7.
[25] J. Pesicka, A. Dronhofer, G. Eggeler, Free dislocations and boundary dislocations in tempered martensite ferritic steels, Mater. Sci. Eng. A 387-389 (2004) 176–180.
[26] R.J. Amodeo, N.M. Ghoniem, Dislocation dynamics I. A proposed methodology for deformation micromechanics, Phys. Rev. B 41 (10) (1990) 6958–6967.
[27] J.M. Salazar, O. Politano, D. Walgraef, On the dynamics of dislocation patterning, Mater. Sci. Eng. A 234–236 (1997) 397–400.
[28] R.J. Amodeo, N.M. Ghoniem, A review of experimental observations and theoretical models of dislocation cells and subgrains, Res. Mech. 23 (1988) 137–160.
[29] R.J. Amodeo, Dynamic Simulation of Dislocation Pattern Formation in Metal During High Temperature Monotonic and Cyclic Deformation (Ph.D. thesis), University of California at Los Angeles, CA, 1988.
[30] S. Takeuchi, A.S. Argon, Steady state creep of single-phase crystalline matter at high temperature, J. Mater. Sci. 11 (1976) 1542–1566.
[31] J. Hald, Microstructure and long-term creep properties of 9–12% Cr steels, Int. J. Press. Vessels Pip. 85 (2008) 30–37.
[32] K. Maruyama, K. Sawada, J. Koike, Strengthening mechanisms of creep resistant tempered martensitic steel, ISIJ Int. 41 (6) (2001) 641–653.
[33] Y. Kadoya, N. Nishimura, B.F. Dyson, M. McLean, Origins of tertiary creep in high chromium steels, in: J.C. Earthman, F.A. Mohamed (Eds.), Creep & Fracture of Engineering Materials & Structures, TMS, War-rendale, USA, 1997, pp. 343–352.
[34] S.D. Yadav, B. Sonderegger, B. Sartory, C. Sommitsch, C. Poletti, Characterisation and quantification of cavities in 9Cr martensitic steel for power plants, Mater. Sci. Technol. 31 (5) (2015) 554–564.
[35] J.S. Lee, H.G. Armaki, K. Maruyama, T. Muraki, H. Asahi, Causes of breakdown of creep strength in 9Cr-1.8W-0.5Mo-VNb steel, Mater. Sci. Eng. A 428 (2006) 270–275.
[36] F. Sket, K. Dzieciol, A. Borbély, A.R. Kaysser-Pyzalla, K. Maile, R. Scheck, Microtomographic investigation of damage in E911 steel after long term creep, Mater. Sci. Eng. A 528 (2010) 103–111.
[37] X. Zhou, Y. Liu, C. Liu, B. Ning, Evolution of creep damage in a modified ferritic heat resistant steel with excellent short-term creep performance and its oxide layer characteristic, Mater. Sci. Eng. A 608 (2014) 46–52.
[38] J. Pesicka, A. Aghajani, Ch Somsen, A. Hartmaier, G. Eggeler, How dislocation substructures evolve during long-term creep of a 12% Cr tempered martensitic ferritic steel, Scr. Mater. 62 (2010) 353–356.
[39] C.G. Panait, A. Zielinska-Lipiec, T. Koziel, A. Czyrska-Filemonowicz, A. Gourgues-Lorenzon, W. Bendick, Evolution of dislocation density, size of subgrains and MX-type precipitates in a P91 steel during creep and during thermal ageing at 600 °C for more than 100,000 h, Mater. Sci. Eng. A 527 (2010) 4062–4069.
[40] D. Terada, F. Yoshida, H. Nakashima, H. Abe, Y. Kadoya, In-situ observation of dislocation motion and its mobility in Fe-Mo and Fe-W solid solutions at high temperatures, ISIJ Int. 42 (2002) 1546–1552.
[41] W. Blum, P. Eisenlohr, F. Breutinger, Understanding creep – a review, Metall. Mater. Trans. A 33A (2002) 291–303.
[42] B. Sonderegger, S. Mitsche, H. Cerjak, Microstructural analysis on a creep resistant martensitic 9–12% Cr steel using the EBSD method, Mater. Sci. Eng. A 481–482 (2008) 466–470.
[43] A. Orlova, J. Bursik, K. Kucharova, V. Sklenicka, Microstructural development during high temperature creep of 9% Cr steel, Mater. Sci. Eng. A 245 (1998) 39–48.
[44] Y. Hasegawa, Grade 92 creep-strength-enhanced ferritic steel, in: A. Shibli (Ed.), Coal Power Plant Materials and Life Assessment, Developments and Applications, 2014, pp. 52–86.

Materials Characterization 115 (2016) 23–31

Contents lists available at ScienceDirect

Materials Characterization

journal homepage: www.elsevier.com/locate/matchar

Evolution of the substructure of a novel 12% Cr steel under creep conditions

Surya Deo Yadav [a,*], Szilvia Kalácska [b], Mária Dománková [c], David Canelo Yubero [a], Roland Resel [d], István Groma [b], Coline Beal [a], Bernhard Sonderegger [a], Christof Sommitsch [a], Cecilia Poletti [a]

[a] *Institute of Materials Science and Welding, Graz University of Technology, Graz, Austria*
[b] *Department of Materials Physics, Eötvös Loránd University, Budapest, Hungary*
[c] *Institute of Materials Science of MTF STU, Trnava, Slovakia*
[d] *Institute of Solid State Physics, Graz University of Technology, Graz, Austria*

ARTICLE INFO

Article history:
Received 26 December 2015
Received in revised form 3 March 2016
Accepted 16 March 2016
Available online 19 March 2016

Keywords:
TEM
XRD
EBSD
Dislocations
Rietveld refinement
Creep

ABSTRACT

In this work we study the microstruture evolution of a newly developed 12% Cr martensitic/ferritic steel in as-received condition and after creep at 650 °C under 130 MPa and 80 MPa. The microstructure is described as consisting of mobile dislocations, dipole dislocations, boundary dislocations, precipitates, lath boundaries, block boundaries, packet boundaries and prior austenitic grain boundaries. The material is characterized employing light optical microscopy (LOM), scanning electron microscopy (SEM), transmission electron microscopy (TEM), X-ray diffraction (XRD) and electron backscatter diffraction (EBSD). TEM is used to characterize the dislocations (mobile + dipole) inside the subgrains and XRD measurements are used to the characterize mobile dislocations. Based on the subgrain boundary misorientations obtained from EBSD measurements, the boundary dislocation density is estimated. The total dislocation density is estimated for the as-received and crept conditions adding the mobile, boundary and dipole dislocation densities. Additionally, the subgrain size is estimated from the EBSD measurements. In this publication we propose the use of three characterization techniques TEM, XRD and EBSD as necessary to characterize all type of dislocations and quantify the total dislocation densty in martensitic/ferritic steels.

1. Introduction

9–12% Cr steels are suitable candidates for power plant applications due to their good creep properties and low procurement cost [1–4]. Available 9% Cr steels do not have enough corrosion resistance at 650 °C, therefore the amount of Cr in these steels is raised up to ~12%, targeting 650 °C and 32.5 bar steam conditions [5–7]. The development of new steels with higher creep and corrosion resistance is a need to improve the efficiency of the power plants and thus, decrease CO_2 emissions. The recent call from European Commission (EC), RFCS-2015 (Research Fund for Coal and Steel) is an example of the interest in the development of such steels [8].

Nowadays, it is not sufficient to support the development of new steel variants for high temperature applications by phenomenological models, where large amounts of parameters are unknown and can only be adapted by long creep experiments [9–10]. More promising approaches are physical models where the microstructural evolution and its link to the creep deformation rate are considered. In this context, relevant input and output variables are: dislocation densities, subgrain sizes and precipitation state. Many developed physical models based on the evolution of dislocation creep distinguish among different types of dislocation densities, such as mobile, dipole and boundary. Additional required microstructural features are subgrain size and information related to strengthening particles (i.e. mean radius and number density) as discussed in [11–12]. A reliable and complete set of data and physical interpretation of the phenomena are a prerequisite for the development of a comprehensive physical model. Thus, the characterization of the substructure in terms of different types of dislocation densities and subgrain size in as-received and crept conditions, is of utmost importance to support modelling and hence, further material development.

Researchers have characterized the substructure of materials in as-received and after creep exposure by means of different techniques. The most frequently used technique for the characterization of dislocations within subgrains is transmission electron microscopy (TEM) [1,13–16]. In some cases TEM results are compared with X-ray diffraction (XRD) measurements [1,14]. There are several methods based on X-ray

---

* Corresponding author.
E-mail addresses: surya.yadav@tugraz.at (S.D. Yadav), kalacska@metal.elte.hu (S. Kalácska), maria.domankova@stuba.sk (M. Dománková), david.caneloyubero@tugraz.at (D.C. Yubero), roland.resel@tugraz.at (R. Resel), groma@metal.elte.hu (I. Groma), coline.beal@tugraz.at (C. Beal), bernhard.sonderegger@tugraz.at (B. Sonderegger), christof.sommitsch@tugraz.at (C. Sommitsch), cecilia.poletti@tugraz.at (C. Poletti).

http://dx.doi.org/10.1016/j.matchar.2016.03.015

diffraction analysis to evaluate the dislocation density [1,17–20]. The method suggested by Groma and Székely [17] is independent of the localization of the dislocations and it is used to evaluate the total dislocation density by analysing the asymptotic part of the peaks in the XRD profile. In this method the correct measurement of the tail of the pattern is necessary, i.e. for the asymptotic part intensity/$\text{intensity}_{\max}$ ratio should be at least 0.001. An alternative method suggested by Ungár et. al. [18–19] is used for the evaluation of the mobile dislocation density. This approach is based on the analysis of Fourier coefficient of the line profile of a Bragg reflection. Rietveld refinement has also been used to estimate the mobile dislocation density in steel specimens [20]. On the other hand, the boundary dislocation density has been estimated from electron backscatter diffraction (EBSD), e.g. [15,21–22]. Pešička et. al. [15] used an approach similar to [23] based on the fraction of subgrain boundaries and their misorientation to estimate the boundary dislocation density in a 12% Cr steel. Calcagnotto et. al. [24] suggested a method to evaluate the boundary dislocation density based on Nye's tensor from the 3D EBSD measurements.

Each technique discussed above has the limitation that only some of the dislocations are characterized at a time. For a reliable estimation of each type of dislocation density and of the total dislocation density (mobile + dipole + boundary), the characterization techniques must be combined.

In this paper we present the creep properties and the microstructure development of a new 12% Cr steel containing Ta. To achieve this, a unique combination of experimental techniques is used and clear distinction of dislocation type is for the first time discussed. In the new developed alloy, Ta is added to increase the precipitation kinetics of Z-phase, as discussed in [25–26].

2. Experiments and methods

2.1. Material and creep tests

The chemical composition of the studied 12% Cr martensitic/ferritic steel is given in Table 1. The material was produced by Saarschmiede GmbH, Germany. The heat treatment consisted of a solution treatment at 1150 °C for 1 h, air cooling, an intermediate tempering of 6 h at 650 °C and a final tempering of 6 h at 740 °C. The creep specimens were machined from the block with an aspect ratio (length/diameter) of five and creep loaded at 650 °C with three different initial tensile stresses of 150, 130 and 80 MPa. Interrupted strain measurement technique was employed to measure the elongation at 80 MPa, while a continuous strain measurement was used for the stress levels of 150 and 130 MPa. The interrupted creep tests were carried out by taking the specimens out of the furnaces at regular intervals. After each interval, the sample was cooled down and the elongation was measured to obtain a strain point in the strain vs. time curve. The sample was positioned inside the creep furnace after each measurement. In continuous strain measurement, the elongation was measured continuously using strain gauges. Short term creep tests were carried out using the continuous method, while long term creep tests were performed in the interrupted testing machines. The maximal measured temperature gradient was ±4 °C from top to bottom inside the creep furnaces. All creep tests were carried out under tension in uniaxial creep testing machines according to the EN ISO 204:2009 standard [27].

2.2. Techniques to characterize the microstructure

The investigated specimens were machined from the as-received block as well as from the gauge area (outside of the necking region) of crept samples. Specimens were first ground with silicon carbide paper up to P4000 grit size. A subsequent polishing with 1 μm diamond paste using a Tegrapol-31 polishing machine was applied. Finally, a neutral OP-AN solution (0.02 μm alumina particles) was used to produce a scratch free surface with the help of vibratory polisher VIBROMET 2. The polished specimens were etched with Vilella's reagent for light optical microscopy (LOM) investigations. The light optical micrographs were taken using a ZEISS-AXIO observer.Z1m microscope. A LEO-SEM scanning electron microscope equipped with an energy dispersive X-ray analysis (EDX) system was used to characterize large precipitates along the prior austenitic grain boundaries.

For EBSD measurements, the specimens were further polished for 24 h on a vibrational polishing machine using a neutral OP-AN suspension. Afterwards, a high energy (10 keV) Argon (Ar) ion milling machine SC-1000 SEMPrep was used for the final surface preparation. Samples' surfaces were prepared using the parameters optimized in [28–29], i.e. 10 keV Ar ion beam, 7° incident angle and 25 min of milling time. EBSD measurements were performed on a FEI Quanta 3D FEG-SEM equipped with EDAX EBSD. The area of measurement was $60 \times 60\ \mu m^2$ with a step size of 0.15 μm. TSL OIM™ 7 software was used to analyse the EBSD data. Applying the grain dilation method, grains having a size of less than 10 pixels were removed from all the measurements for reliable statistics. Orientation map, grain boundary map and histograms were generated accordingly. Boundaries with misoriention angle less than 4° were considered as low angle boundaries (subgrain boundaries) [15]. The subgrain size (D_{subg}) was evaluated using a partition threshold of minimum grain tolerance angle 0.5° and grain size larger than 4 pixels.

Thin foils for TEM observations were prepared from the samples in both conditions, as-received and after creep. Discs of 3 mm in diameter and ~0.1 mm thickness were jet electro-polished in an electrolyte $HNO_3 : CH_3OH = 3:7$ at 0 °C and 15 V to obtain transparent areas for electrons near to the central hole. TEM observations were performed using microscopes JEOL 200CX operating at 200 kV and Philips CM 300 operating at 300 kV. Double beam condition was used for dislocation images, selecting six random regions within the thin foils. Electron diffraction was used for the phase identification.

The specimens characterized using XRD were polished for 24 h using OP-AN solution. XRD patterns were collected on a laboratory diffractometer (PANalytical Empyrean). The setup was equipped with an X-ray mirror at the primary side to monochromatize and parallelize the primary Cu radiation ($\lambda_{CuK\alpha1} = 1.541 \times 10^{-10}$ m and $\lambda_{CuK\alpha2} = 1.544 \times 10^{-10}$ m). The scattered beam was detected via a Soller slit with a one-dimensional solid state detector (PIXcel^{3D}) operating in scanning line mode. Specular scans were carried out within the 2θ range of 36° to 145°, with step size of 0.02°. A standard reference specimen (NIST Standard SRM660) of LaB_6 was used to measure the instrumental broadening. MAUD software was used for evaluation of lattice microstrain due to isolated dislocations within grains, identified as mobile dislocations, employing least square Rietveld refinement [30–32]. Fourth order polynomial was used to fit the background and pseudo-Voigt functions to fit the peak shape. The quality of refinement was based on weighted pattern values R_w and R_{wnb} (without the background), to assess the quality of Rietveld refinement [33].

Table 1
Alloying elements in the investigated 12% Cr steel, balance is Fe.

Elements	C	Si	Mn	W	Co	Cu	Cr	Mo	Ni	Al	Ta	B	N
wt.%	0.06	0.31	0.21	2.47	3.50	1.95	12.1	0.01	0.19	0.002	0.36	0.006	0.06

2.3. Dislocation density measurement

The mean linear intercept method was applied on TEM micrographs to estimate the dislocation density inside the subgrains. The expression for the dislocation density can be given as [34]:

$$\rho_{int} = \left(\frac{2 \cdot \sum N_i}{e \cdot \sum L_i}\right) \tag{1}$$

where ρ_{int} accounts for the sum of mobile dislocation and dipole dislocation densities, e is the thickness of the thin foil, N_i is the number of intersections between grid and dislocations and L_i is the length of the grid.

In general dislocations also provoke an elastic strain that produces a broadening in the XRD line profile [18,35]. The broadening is associated with long range stress fields of dislocations inside the subgrains. The boundary dislocations have short range stress fields associated, because they are configured themselves in low energy positions and hence, they do not contribute in to the peak broadening. The stress fields of dipoles are relatively low in comparison to stress fields produced by mobile dislocations. Hence the, contribution of dipoles to the peak broadening is considered to be negligible [14]. The lattice microstrain produced by the mobile dislocations inside the subgrains is related as [32,35–36]:

$$\rho_m = \frac{k e^2_{\mathrm{RMS}}}{F b^2} \tag{2}$$

where b is the Burger's vector, e^2_{RMS} is the root mean square lattice microstrain, and $k = 14.4$ and $F = 1$ for a bcc crystal structure [35]. The lattice microstrain was evaluated with MAUD software using the Popa model [37] and dislocation density was estimated from Eq. (2). The crystallite size was found to be 0.12 μm in as-received condition and 0.13 μm after creep at 130 MPa/650 °C.

The low angle grain boundaries are the direct manifestation of boundary dislocations and are responsible for the misorientation between two neighbouring subgrains. Thus, the dislocations stored in a particular boundary i can be estimated from the expression [15,21–23]:

$$\rho_{bi} = \frac{\Theta_i f_i}{2b} r_{AV} \tag{3}$$

where Θ_i is the misorientation of the boundary, f_i is the fraction of the boundary i and r_{AV} is the ratio of subgrain surface area to subgrain volume. The total boundary dislocation density can be evaluated using EBSD data as $\rho_b = \Sigma \rho_{bi}$.

3. Results

3.1. As-received microstructure and creep properties

Fig. 1 shows the microstructural details of the material in the as-received condition. The material shows a martensitic/ferritic structure with prior austenite grain boundaries, block and lath boundaries (see Fig. 1a, b and c). The EDX analysis along the marked arrow in Fig. 1b is depicted in Fig. 1d in terms of elements. It can be observed that the prior austenite grain boundaries are decorated with $M_{23}C_6$ carbides and Laves phases.

Fig. 1c shows the TEM image of the as-received material, revealing the presence of martensitic laths with a high dislocation density. The lath boundaries are pinned by the Laves phase particles.

The creep curves are depicted in Fig. 2. Fig. 2a shows the creep curves from continuous strain measurements at higher stresses, i.e. 150 and 130 MPa. Fig. 2b shows the creep curve for 80 MPa obtained from the interrupted strain measurements and fitted with a B-spline function. Minimum creep rates and rupture times at different stresses are given in Table 2. The longest rupture time was 5793 h for the sample

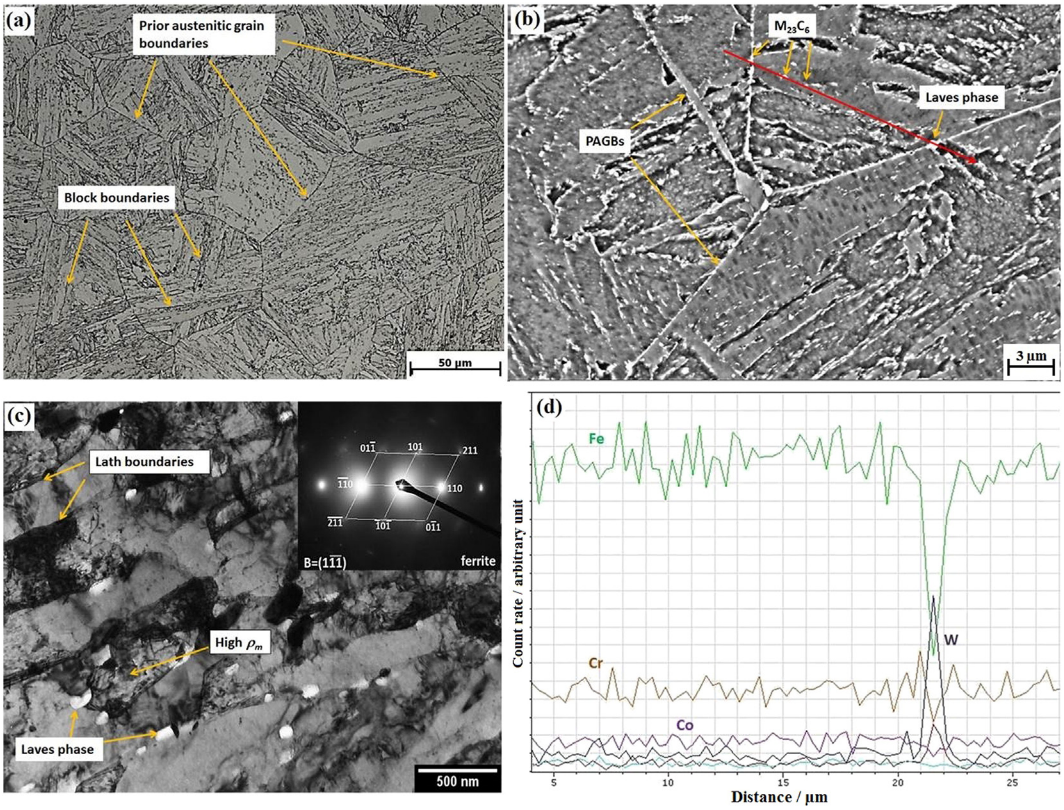

Fig. 1. Microstructure of as-received material: a) LOM image; b) SEM image; c) TEM image; and d) EDX analysis of line scan indicated with an arrow in image (b).

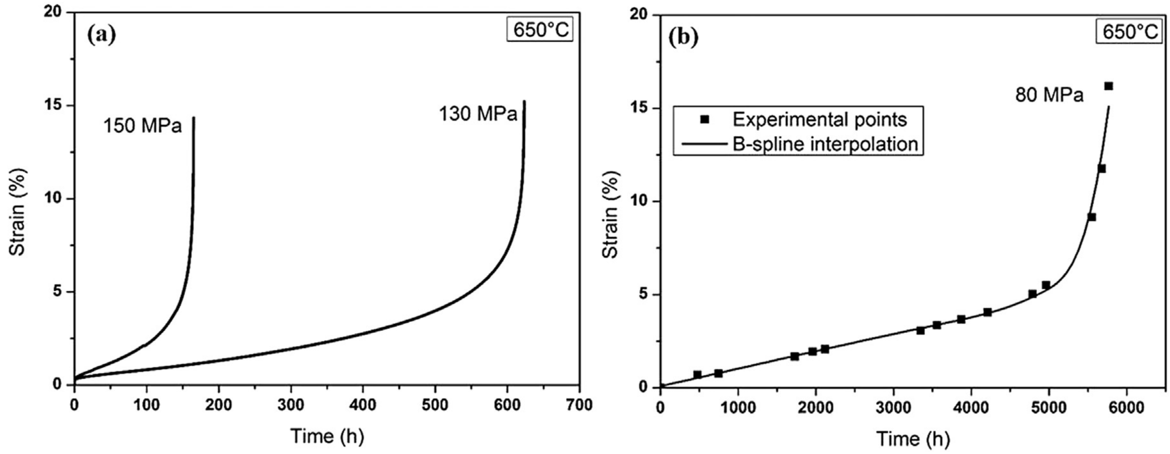

Fig. 2. Creep curves at 650 °C for external loads of a) 150 MPa and 130 MPa; and b) 80 MPa.

subjected to 80 MPa. The exponent n was evaluated following the equation:

$$n = (\partial \ln \dot{\varepsilon}_{\min} / \partial \ln \sigma)_T. \quad (4)$$

A value of $n = 4.08$ was found, which can be correlated to dislocation creep as the main creep mechanism [38–40]. The creep rupture strength (80 MPa/650 °C, 5793 h) of the studied steel is comparable with the data published on P92 (90 MPa/650 °C, 5043.6 h) [38].

3.2. TEM analysis

TEM images revealed the dislocations inside the subgrains in different conditions, as shown in Fig. 3. A higher dislocation population was observed in as-received material (Fig. 3a). The dislocation population was lower in the crept materials loaded at 130 and 80 MPa at 650 °C (Fig. 3b and c, respectively).

The dislocation density was calculated using Eq. (1) (see results in Table 4). The dislocation density of the as-received material decreased almost 4 times after creep exposure under 130 MPa/650 °C, and 12 times under 80 MPa/650 °C.

3.3. Rietveld analysis of XRD measurements

The Rietveld plot of the as-received material is shown in Fig. 4. The crystallographic planes were identified in accordance with the martensitic/ferritic steels [14]. The experimental data are shown with points and the refinement as a continuous line.

The lattice microstrains and the ρ_m calculated using the Rietveld refinement and Eq. (2) are summarized in Table 3. Rietveld refinement resulted in R_w and R_{wnb} (no background) values smaller than 5% in all refinements (see Table 3).

3.4. EBSD analysis

Orientation maps (left) and grain boundary maps (right) are shown in Fig. 5 for as-received condition (a, b), and after creep at 130 MPa/650 °C (c, d) and 80 MPa/650 °C (e, f). The typical martensitic/ferritic microstructure can be seen in Fig. 5a. The subgrain size increased and

Table 2
Minimum creep rates and rupture times at 650 °C.

Stress (MPa)	Min creep rate (s^{-1})	Rupture time (h)
150	3.70×10^{-8}	165
130	1.19×10^{-8}	623
80	0.24×10^{-8}	5793

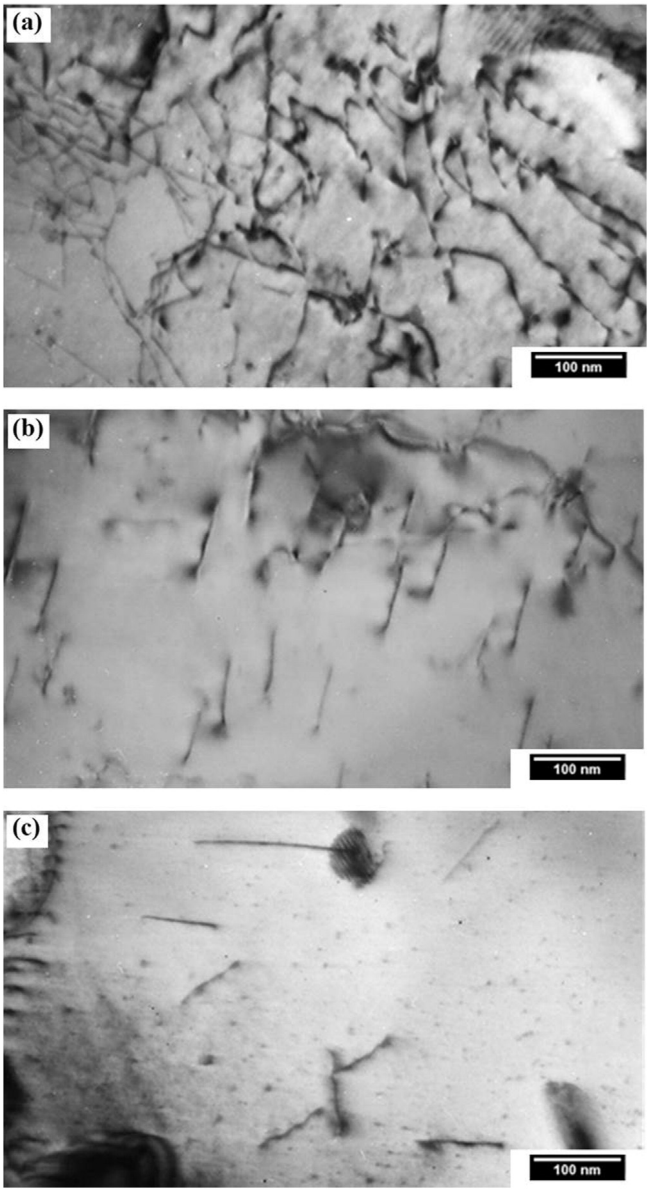

Fig. 3. Bright-field TEM images showing dislocations inside the subgrains in a) as-received condition, and after creep at 650 °C b) 130 MPa; and c) 80 MPa.

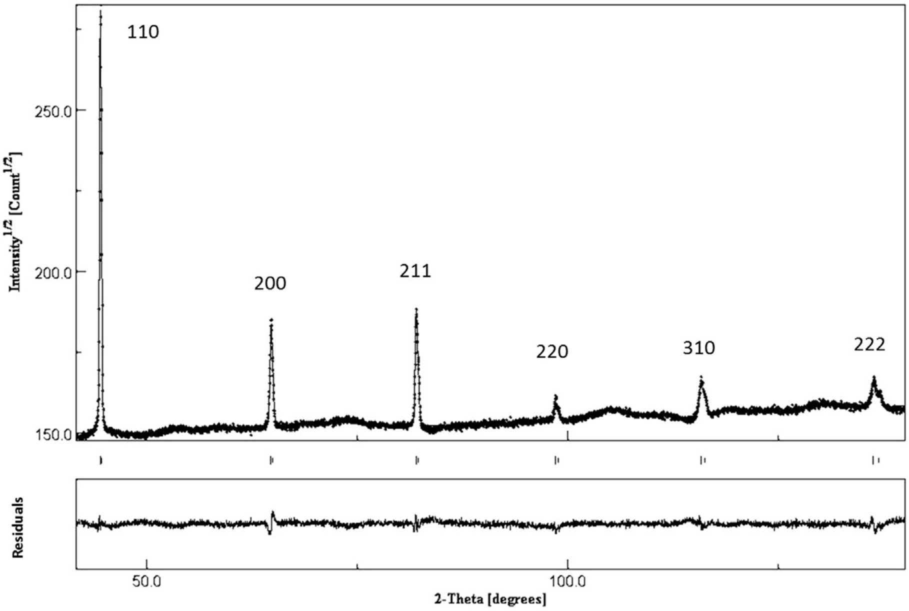

Fig. 4. Rietveld plot of the as-received material showing the refinement as a continuous line and experimental data as points. Residuals are also indicated in the bottom plot.

the fraction of low angle grain boundaries decreased after creep, as can be observed from Fig. 5c, d, e and f. Qualitatively, more polygonized subgrains were observed after 5793 h of creep exposure under 80 MPa/650 °C. The subgrain size was increased from 0.52 μm in as-received condition to 0.9 μm and 1.5 μm after creep loading at 130 MPa/650 °C and 80 MPa/650 °C, respectively.

Histograms of misorientation angles up to 12° are shown in Fig. 6 for different material conditions. It was observed that the frequency of low angle grain boundaries decreased after creep.

The boundary dislocation densities were calculated using subgrain boundaries having a misorientation angle between 1 and 4° with Eq. (3), and the results are summarized in Table 4.

4. Discussion

The results on dislocation densities and creep behavior are analysed from the methodology and the material behavior points of view.

4.1. Measurement of dislocation density

The reliable estimation of different dislocation densities is essential for the modelling of creep behavior of materials exposed to high temperatures during long periods. In this way development of new creep resistance steels can be supported by validated physical models. The dislocation density can be classified into different groups. Previous developed models assume the following arrangement of dislocations: mobile and dipole dislocations in the interior of subgrains, and boundary dislocations at subgrain boundaries [11,12]. Therefore, the total dislocation density (ρ_{tot}) is calculated as the sum of mobile (ρ_m), boundary (ρ_b) and dipole (ρ_{dip}) dislocation densities,

$$\rho_{tot} = \rho_m + \rho_b + \rho_{dip}. \tag{5}$$

Table 3
Lattice microstrains, mobile dislocation densities and quality factors from the Rietveld refinements.

Specimens	e^2_{RMS}	ρ_m (m^{-2})	R_w (%)	R_{wnb} (%)
As-received	7.7×10^{-4}	1.0×10^{14}	0.9	1.3
130 MPa/650 °C	4.1×10^{-4}	0.3×10^{14}	1.1	3.6

The measurement techniques (TEM, XRD and EBSD) employed in this research are usually the most preferred to characterize the dislocation density evolution in metallic materials. However, all three techniques have the limitations that only some of the dislocations can be characterized at a time using one technique (see Fig. 7). For example, XRD is preferred to characterize the mobile dislocation density and EBSD to characterize the boundary dislocation density. On the other hand TEM allows estimating all dislocations located at the interior of the subgrains:

$$\rho_{int} = \rho_m + \rho_{dip}. \tag{6}$$

The probabilities of uncertainties in measurements using these techniques are pointed out in [41]. The possible sources of error in TEM measurements are: narrow areas of investigation, dislocations that are not visible, modification of substructure during sample preparation and inaccurate thin foil thickness measurement [41]. Rietveld refinement of collected XRD pattern is used to evaluate the mobile dislocation density based on lattice microstrain. The refinement should be carried out carefully until the R_w values become less than 5% to obtain accurate results [33]. With this method, it is assumed that other types of dislocations are arranged in a more stable configuration, producing negligible strain field with respect to mobile dislocations. The dipole dislocation density was estimated in this work from Eq. (6), subtracting the ρ_m (XRD) from ρ_{int} (TEM). The estimation of boundary dislocation was based on EBSD measurements using Eq. (3). It is important to point out that the evaluation of the boundary dislocation density is based on the assumption that subgrains have a spherical shape that subgrains are sharp, and the misorientations that define subgrains are situated between 1 and 4°.

The results obtained in different conditions are summarized in Table 4, showing the recovery of the microstructure through the annihilation of dislocations and the growth of subgrains after creep condition.

In grade X20 martensitic steel (a similar 12% Cr steel) [14,15] the dislocation density obtained from TEM was ~3 times higher than from XRD measurement, i.e., in the same order of magnitude that results revealed here. The reason of this difference is that the measurements are not comparable, since TEM measurements include mobile dislocations as well as dipole dislocations, while the broadening is caused almost only by mobile dislocations. The mobile dislocation density in X20 was reported to be 0.3×10^{14} m^{-2} after loading under 120 MPa/650 °C [15],

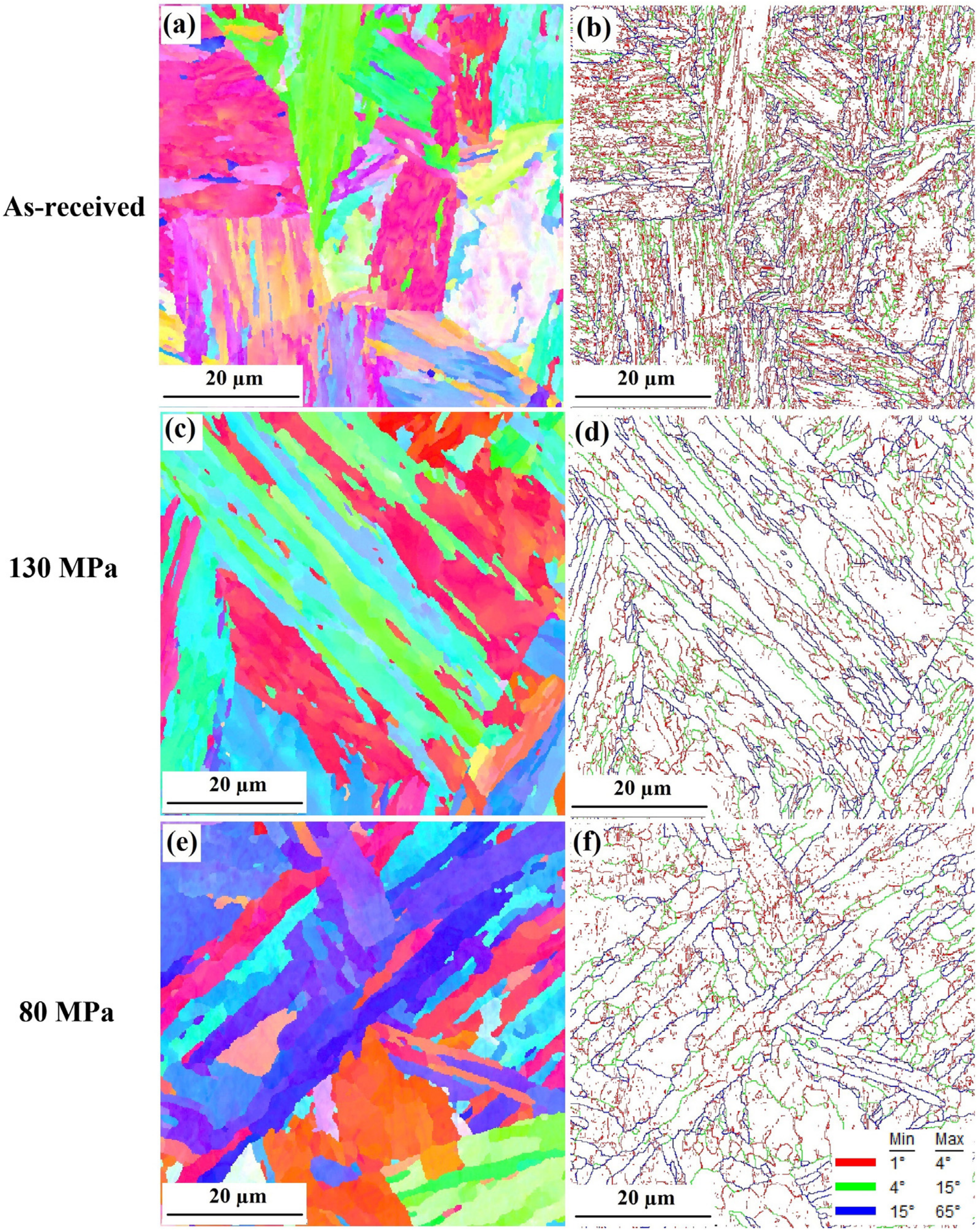

Fig. 5. Orientation maps (left) and grain boundary maps (right) of the as-received (a, b); crept specimens at 650 °C under 130 MPa (c, d) and 80 MPa (e, f). For the orientation maps, arbitrary colours were used. (For interpretation of the references to colour in this figure legend, the reader is referred to the web version of this article.)

a value comparable with the one measured in this work at 130 MPa/ 650 °C.

In the as-received condition, boundary dislocation density in X20 was reported to be $4.1 \times 10^{14}\ \mathrm{m}^{-2}$ [15], while in the present study it is $5.2 \times 10^{14}\ \mathrm{m}^{-2}$. After loading under 120 MPa/650 °C boundary dislocation density in X20 decreased to $2 \times 10^{14}\ \mathrm{m}^{-2}$ [15] compared to $2.3 \times 10^{14}\ \mathrm{m}^{-2}$ in the present case under 130 MPa/650 °C. These differences in the dislocation densities can be ascribed to variations in chemical compositions, heat treatments and loading conditions of two steels, although the order of magnitude and evolution behavior of both martensitic steels are similar.

In our work we demonstrated that the measurement of the total dislocation density is possible only using the combination of EBSD and TEM. The distinction between dipole and mobile dislocations can be done using both, TEM and XRD measurements.

4.2. Input data for the models

The development of physical models for creep requires both: the identification of the governing creep mechanism (i.e. dislocation creep or diffusion creep), and the evolution of microstructural variables. Dislocation creep behavior was identified after the Norton's exponent $n = 4.08$ [38–40]. The microstructural variables for modelling dislocation creep (ρ_m, ρ_b, ρ_{dip} and D_{subg}) were characterized and quantified employing TEM, XRD and EBSD.

Another important parameter for physical based modelling is the glide velocity of mobile dislocations [11,12]. Since the creep rate depends on the average glide velocity, a good estimation of glide velocity is needed to calibrate the models. The measurement of glide velocity is difficult via experiments, but it can be easily estimated based on minimum creep rate and mobile dislocation density. The Orowan's equation

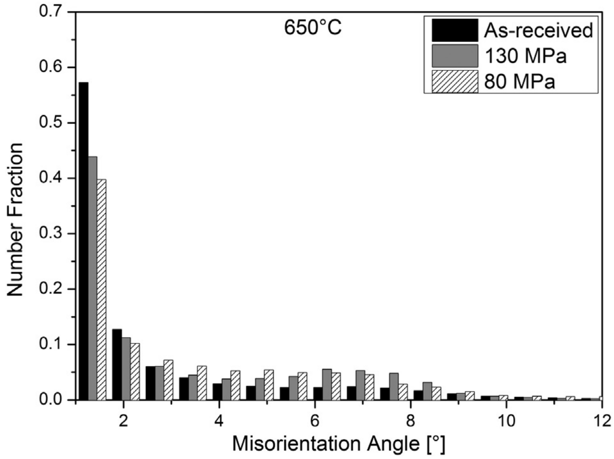

Fig. 6. Histograms of misorientation angles in as-received condition and after creep under 130 MPa/650 °C and 80 MPa/650 °C.

relates the mobile dislocation density and the average glide velocity (v_g) through the minimum creep rate ($\dot{\varepsilon}_{\min}$):

$$\dot{\varepsilon}_{\min} = b\rho_m v_g / M \tag{7}$$

where, ρ_m is the mobile dislocation density at the gauge part, far from the necking region of the broken specimen. In the present study, the estimated glide velocity was 4.15×10^{-12} m/s under 130 MPa/650 °C. Panait et. al. [42] reported a glide velocity of 2×10^{-15} m/s in a P91 steel under a loading condition of 80 MPa/600 °C.

The combination of results reported in this study such as governing creep mechanism and quantitatively microstructural information given by ρ_m, ρ_b, ρ_{dip}, D_{subg} and v_g provide valuable data to support physical based models. While the data of the as-received material provides input data, the values of the crept samples will allow the validation of microstructural and creep models.

4.3. Microstructural evolution during creep

When materials are loaded at high temperatures, the microstructure evolves due to diffusional and relaxation processes. While all quantifications done in this paper are based on mean values of dislocation densities, the real situation is a heterogeneous microstructure, as shown in Fig. 8 for the material in the as-received condition.

The material in as-received condition has shown high dislocation density (see Fig. 3a). The total dislocation density was decreased from 7.52×10^{14} m^{-2} to 1.70×10^{14} m^{-2} under 80 MPa/650 °C (see Table 4). Under the application of an external load, the mobile dislocations start to move and interact with other dislocations in several ways [11]. It can be observed that the annihilation of dipole dislocations is larger than the annihilation of mobile dislocations (see Table 4). The annihilation of all dislocations dominates over their production after the primary creep. The reduction of boundary dislocation density is observed as the growth of subgrains, that increased from 0.52 μm to 1.5 μm after 5793 h of creep exposure at 80 MPa/650 °C by the recombination and migration of subgrain boundaries [43]. Fig. 9 shows the bright-field image of a well polygonized subgrain after creep under 80 MPa/650 °C.

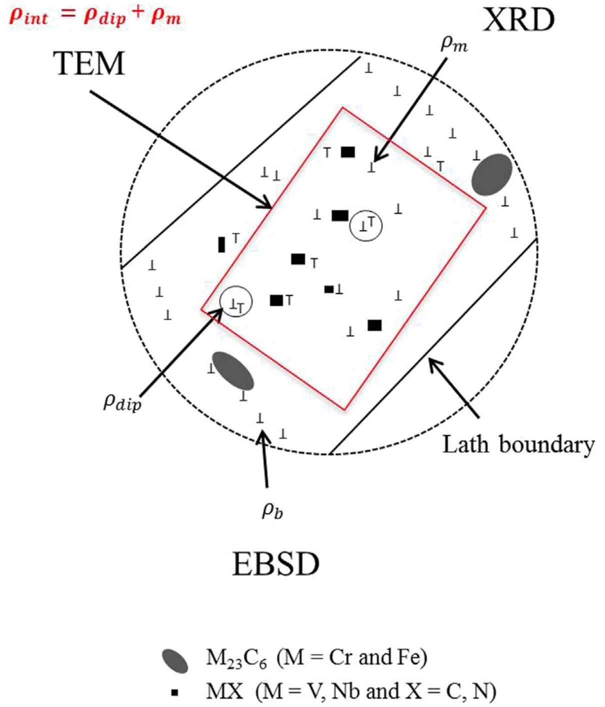

Fig. 7. Schematic showing the applicability of different characterization techniques.

The dislocation densities have maximum values at highest stress and similar evolution behavior is reported in [34], while the subgrain size is smaller at higher stresses. Other researchers have also found an inverse relationship between applied stress and subgrain size in martensitic/ferritic steels [44–45].

Some other aspects with respect to microstructural evolution usually not taken into account in continuous modelling are: a) heterogeneous distribution of dislocations (see Fig. 8) and b) high angle grain boundary migration, observed as serration of the boundaries in Fig. 5f. Since these aspects are not considered so far in the revised creep models, the prediction power of these models is limited.

5. Summary and conclusions

In this research, creep behavior and substructure evolution of a newly developed 12% Cr steel were studied. The deformation mechanism was identified as dislocation creep. The dislocations were characterized by three different techniques: TEM, XRD and EBSD. The mobile dislocation density was measured from XRD. TEM was employed to measure the mobile and dipole dislocations inside the subgrains. The boundary dislocation density was evaluated from the EBSD data. The total dislocation density was estimated from the addition of mobile, dipole and boundary dislocation density. The total dislocation density was decreased 4.5 times and subgrain size was increased from 0.52 μm to 1.5 μm after 5793 h of creep loading at 650 °C. Moreover, more polygonized subgrains were observed after creep. The creep rupture strength of the new steel is comparable with the data published on P92 [38]. It would be too early at this stage to predict the very long term creep behavior, thus the creep experiments of more than

Table 4
Dislocation densities ($\times 10^{14}$ m^{-2}) and subgrain size (μm).

Method	TEM	XRD	EBSD	TEM − XRD	TEM + EBSD	EBSD
Specimen	$\rho_{int} = \rho_m + \rho_{dip}$	ρ_m	ρ_b	$\rho_{dip} = \rho_{int} - \rho_m$	$\rho_{tot} = \rho_m + \rho_b + \rho_{dip}$	D_{subg}
As-received	2.33 ± 0.63	1.0	5.2	1.33	7.52	0.52
130 MPa	0.62 ± 0.19	0.3	2.3	0.32	2.92	0.90
80 MPa	0.20 ± 0.06	–	1.5	–	1.70	1.50

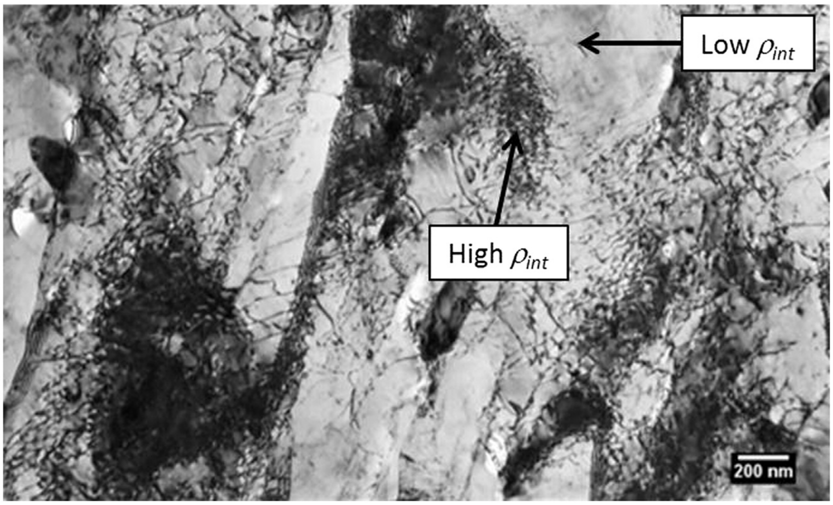

Fig. 8. TEM image showing a heterogeneous microstructure in as-received condition with regions of high and low dislocation densities.

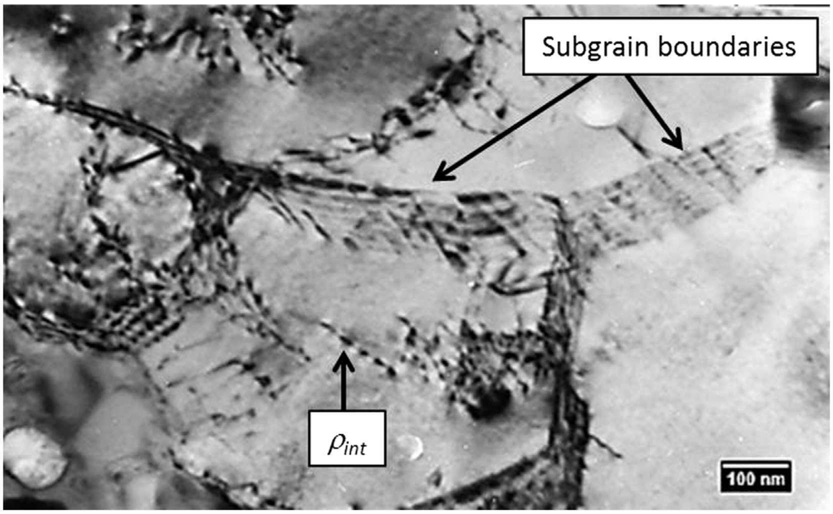

Fig. 9. TEM image of the crept sample under 80 MPa/650 °C showing polygonized subgrain.

10,000 h should be carried out in order to evaluate the long run performance.

We conclude that all three techniques together (TEM + XRD + EBSD) are necessary for the distinction of dislocations in metallic materials. Combining these techniques, a realistic estimation of the evolution of the dislocation density can be achieved. Rietveld refinement is a strong tool to estimate the mobile dislocation density since the peak broadening is produced by the mobile dislocations. TEM measurements provide the dislocation density within subgrains, meaning dipole and mobile dislocations.

A good estimation of the glide velocity can be achieved from the combination of the minimum creep rate and mobile dislocation density of the broken specimens (outside of the necking region). A combination of the presented microstructural analysis with the predicted glide velocity will improve the development of physical models and hence the development of new creep resistant steels.

Acknowledgments

The authors would like to thank Prof. J Hald, DTU (Denmark) for the material development and Bernhard Donth, Saarschmiede GmbH in Germany for supplying the material as well as the European Commision for funding project Z-Ultra: 309916.

References

[1] Z. Cong, Y. Murata, Dislocation density of lath martensite in 10Cr–5W heat-resistant steels, Mater. Trans. 52 (12) (2011) 2151–2154.
[2] K. Sawada, M. Takeda, K. Maruyama, R. Ishii, M. Yamada, Y. Nagae, R. Komine, Effect of W on recovery of lath structure during creep of high chromium martensitic steels, Mater. Sci. Eng. A 267 (1) (1999) 19–25.
[3] Y. Xu, X. Zhang, Y. Tian, C. Chen, Y. Nan, H. He, M. Wang, Study on the nucleation and growth of $M_{23}C_6$ carbides in a 10% Cr martensite ferritic steel after long-term aging, Mater. Charact. 111 (2016) 122–127.
[4] B. Sonderegger, S. Mitsche, H. Cerjak, Martensite laths in creep resistant martensitic 9–12% Cr steels — calculation and measurement of misorientations, Mater. Charact. 58 (2007) 874–882.
[5] H.K. Danielsen, J. Hald, Behaviour of Z phase in 9–12%Cr steels, Energy Mater. 1 (2006) 49–57.
[6] H.K. Danielsen, P.E.D. Nunzio, J. Hald, Kinetics of Z-phase precipitation in 9–12% Cr steels, Metall. Mater. Trans. A 44A (2013) 2445–2452.
[7] H.C. Furtado, L.H. de Almeida, I. Le May, Precipitation in 9Cr–1Mo steel after creep deformation, Mater. Charact. 58 (2007) 72–77.
[8] http://ec.europa.eu/research/participants/portal/desktop/en/opportunities/rfcs/topics/53-rfcs-02-2015.html
[9] M. McLean, B.F. Dyson, Modeling the effects of damage and microstructural evolution on the creep behavior of engineering alloys, J. Eng. Mater. Technol. 122 (2000) 273–278.
[10] Y.F. Yin, R.G. Faulkner, Continuum damage mechanics modelling based on simulations of microstructural evolution kinetics, Mater. Sci. Technol. 22 (8) (2006) 929–936.
[11] N.M. Ghoniem, J.R. Matthews, R.J. Amodeo, A dislocation model for creep in engineering materials, Res. Mech. 29 (1990) 197–219.

[12] M. Basirat, T. Shrestha, G.P. Potirniche, I. Charit, K. Rink, A study of the creep behaviour of modified 9Cr–1Mo steel using continuum-damage modelling, Int. J. Plast. 37 (2012) 95–107.

[13] A. Aghajani, Ch. Somsen, G. Eggeler, On the effect of long-term creep on the microstructure of a 12% chromium tempered martensite ferritic steel, Acta Mater. 57 (2009) 5093–5106.

[14] J. Pešička, R. Kužel, A. Dronhofer, G. Eggeler, The evolution of dislocation density during heat treatment and creep of tempered martensite ferritic steels, Acta Mater. 51 (2003) 4847–4862.

[15] J. Pešička, A. Dronhofer, G. Eggeler, Free dislocations and boundary dislocations in tempered martensite ferritic steels, Mater. Sci. Eng. A 387-389 (2004) 176–180.

[16] J. Pešička, A. Aghajani, Ch. Somsen, A. Hartmaier, G. Eggeler, How dislocation substructures evolve during long-term creep of a 12% Cr tempered martensitic ferritic steel, Scr. Mater. 62 (2010) 353–356.

[17] I. Groma, F. Székely, Analysis of the asymptotic properties of X-ray line broadening caused by dislocations, J. Appl. Crystallogr. 33 (6) (2000) 1329–1334.

[18] T. Ungár, Dislocation densities, arrangements and character from X-ray diffraction experiments, Mater. Sci. Eng. A 309-310 (2001) 14–22.

[19] B.E. Warren, B.L. Averbach, The effect of cold-work distortion on X-ray patterns, J. Appl. Phys. 21 (1950) 595–599.

[20] S. Murugesan, P. Kuppusami, E. Mohandas, M. Vijayalakshmi, X-ray diffraction Rietveld analysis of cold worked austenitic stainless steel, Mater. Lett. 67 (1) (2012) 173–176.

[21] Niels Hansen, Hall–Petch relation and boundary strengthening, Scr. Mater. 51 (2004) 801–806.

[22] G.S. Dyakonov, E. Zemtsova, S. Mironov, I.P. Semenova, R.Z. Valiev, S.L. Semiatin, An EBSD investigation of ultrafine-grain titanium for biomedical applications, Mater. Sci. Eng. A 648 (2015) 305–310.

[23] F.J. Humphreys, M. Hatherly, Recrystallization and Related Annealing Phenomena, second ed., 2004.

[24] M. Calcagnotto, D. Ponge, E. Demir, D. Raabe, Orientation gradients and geometrically necessary dislocations in ultrafine grained dual-phase steels studied by 2D and 3D EBSD, Mater. Sci. Eng. A 527 (2010) 2738–2746.

[25] F. Liu, M. Rashidi, L. Johansson, J. Hald, H. Andrén, A new 12% chromium steel strengthened by Z-phase precipitates, Scr. Mater. 113 (2016) 93–96.

[26] K. Lee, S. Hong, J. Shim, J. Suh, J. Huh, W. Jung, Effect of Nb addition on Z-phase formation and creep strength in high-Cr martensitic heat-resistant steels, Mater. Charact. 102 (2015) 79–84.

[27] S.D. Yadav, B. Sonderegger, B. Sartory, C. Sommitsch, C. Poletti, Characterisation and quantification of cavities in 9Cr martensitic steel for power plants, Mater. Sci. Technol. 31 (5) (2015) 554–564.

[28] T. Berecz, S. Kalácska, G. Varga, Z. Dankházi, K. Havancsák, Effect of high energy Ar-ion milling on surface of quenched low-carbon low-alloyed steel, Mater. Sci. Forum 812 (2015) 285–290.

[29] Z. Dankházi, S. Kalácska, A. Baris, G. Varga, Z. Radi, K. Havancsák, EBSD sample preparation: high energy Ar ion milling, Mater. Sci. Forum 812 (2015) 309–314.

[30] M. Ferrari, L. Lutterotti, Method for the simultaneous determination of anisotropic residual stresses and texture by X-ray diffraction, J. Appl. Phys. 76 (1994) 7246–7255.

[31] L. Lutterotti, S. Gialanella, X-ray diffraction characterization of heavily deformed metallic specimens, Acta Mater. 46 (1998) 101–110.

[32] Y. Chen, N. Gao, G. Sha, S.P. Ringer, M.J. Starink, Strengthening of an Al–Cu–Mg alloy processed by high-pressure torsion due to clusters, defects and defect-cluster complexes, Mater. Sci. Eng. A 627 (2015) 10–20.

[33] B.H. Toby, R factors in Rietveld analysis: how good is good enough? Powder Diffract. 21 (1) (2006) 67–70.

[34] R. Lagneborg, Dislocation density and dislocation arrangement during creep of 20% Cr–35% Ni stainless steels, Met. Sci. J. 3 (1969) 18–23.

[35] G.K. Williamson, R.E. Smallman, III. Dislocation densities in some annealed and cold-worked metals from measurements on the X-ray Debye–Scherrer spectrum, Philos. Mag. 1 (1) (1956) 34–46.

[36] A.L. Ortiz, J.W. Tian, J.C. Villegas, L.L. Shaw, P.K. Liaw, Interrogation of the microstructure and residual stress of a nickel-base alloy subjected to surface severe plastic deformation, Acta Mater. 56 (2008) 413–426.

[37] N.C. Popa, The (*hkl*) dependence of diffraction-line broadening caused by strain and size for all laue groups in Rietveld refinement, J. Appl. Crystallogr. 31 (2) (1998) 176–180.

[38] V. Sklenička, K. Kuchařová, P. Král, M. Kvapilová, M. Svobodová, J. Čmakal, The effect of hot bending and thermal ageing on creep and microstructure evolution in thick-walled P92 steel pipe, Mater. Sci. Eng. A 644 (2015) 297–309.

[39] K. Kucharova, V. Sklenicka, M. Kvapilovaa, M.K. Svoboda, Creep and microstructural processes in a low-alloy 2.25%Cr1.6%W steel (ASTM Grade 23), Mater. Charact. 109 (2015) 1–8.

[40] V. Sklenička, K. Kuchařová, M. Svoboda, L. Kloc, J. Buršık, A. Kroupa, Long-term creep behavior of 9–12%Cr power plant steels, Mater. Charact. 51 (2003) 35–48.

[41] M. Li, L. Wang, J.D. Almer, Dislocation evolution during tensile deformation in ferritic–martensitic steels revealed by high-energy X-rays, Acta Mater. 76 (2014) 381–393.

[42] C.G. Panait, A. Zielinska-Lipiec, T. Koziel, A. Czyrska-Filemonowicz, A. Gourgues-Lorenzon, W. Bendick, Evolution of dislocation density, size of subgrains and MX-type precipitates in a P91 steel during creep and during thermal ageing at 600 °C for more than 100,000 h, Mater. Sci. Eng. A 527 (2010) 4062–4069.

[43] M.M. El Rayes, E.A. El-Danaf, A.A. Almajid, Characterization and correlation of mechanical, microstructural and ultrasonic properties of power plant steel, Mater. Charact. 100 (2015) 120–134.

[44] A. Orlová, J. Buršık, K. Kuchařová, V. Sklenička, Microstructural development during high temperature creep of 9% Cr steel, Mater. Sci. Eng. A 245 (1998) 39–48.

[45] B. Sonderegger, S. Mitsche, H. Cerjak, Microstructural analysis on a creep resistant martensitic 9–12% Cr steel using the EBSD method, Mater. Sci. Eng. A 481-482 (2008) 466–470.

Annex 2: Other research papers published during the study period

[I] K. K. Saxena, **S. D. Yadav**, S. Sonkar, V. Pancholi, G. P. Chaudhari, D. Srivastava, G. K. Dey, S. K. Jha and N. Saibaba: Effect of Temperature and Strain Rate on Deformation Behavior of Zirconium Alloy: Zr-2.5Nb, Procedia Materials Science, 6, (2014), 278–283

[II] **S. D. Yadav**, M. Schuler, C. Sommitsch and C. Poletti: Physical based creep strain modelling of 9Cr martensitic steel, Proceedings ECCC (2014), Rome, Italy

[III] **S. D. Yadav**, P. P. Bhingole, G. P. Chaudhari, S. K. Nath and C. Sommitsch: Hybrid Processing of AZ91 Magnesium Alloy/Nano-Al_2O_3 Composites: Key Engineering Materials, 651-653, (2015), 783-788

Available online at www.sciencedirect.com

ScienceDirect

Procedia Materials Science 6 (2014) 278 – 283

Procedia Materials Science

www.elsevier.com/locate/procedia

3rd International Conference on Materials Processing and Characterisation (ICMPC 2014)

Effect of Temperature and Strain Rate on Deformation Behavior of Zirconium Alloy: Zr-2.5Nb

K. K. Saxena[a], S. D. Yadav[b], S. Sonkar[a], V. Pancholi[a*], G. P. Chaudhari[a], D. Srivastava[c], G. K. Dey[c], S. K. Jha[d], N. Saibaba[d]

[a]*Department of Metallurgical and Materials Engineering, Indian Institute of technology, Roorkee-247667,Uttarakhand, India*
[b]*Institute for Materials Science and Welding, TU Graz, Austria*
[c]*Materials Science Division, Bhabha Atomic Research Center, Mumbai-40085, India*
[d]*Nuclear Fuel Complex Limited, Hyderabad-501301, India*

Abstract

The characterization of hot deformation of Zr-2.5Nb in the strain rate range of 0.01 – 10s^{-1} and in the temperature range of 700-925°C has been studied using hot compression testing on Gleeble-3800. For this study, processing maps approach has been adopted and their interpretation done using the Dynamic Material Model (DMM). The power dissipation maps of Zr-2.5Nb with in (α+β) phase field exhibits a domain of dynamic recrystallization, with a peak efficiency of 54-60% at about 750°C and strain rate is 0.01s^{-1}. A second domain that occurs in β-phase field, having peak efficiency 49-54% at about 925°C and 0.01s^{-1} strain rate, which may be optimum condition for the hot working, while a domain at about 725°C and strain rate 0.1s^{-1} shows the instability region where flow will not be stable. Effect of strain on peak efficiency of power dissipation and instability is also studied.

Selection and peer review under responsibility of the Gokaraju Rangaraju Institute of Engineering and Technology (GRIET)

Keywords: Hot deformation; Processing Maps, Zr-2.5Nb

---

1. Introduction

Zirconium and its alloys are extensively used in the nuclear industry. These alloys have low neutron cross-section, good corrosion resistance at higher temperatures and excellent mechanical properties [Bruschi S., Poggio S., Quadrini F., Tata M.E., 2004]. Zr-2.5Nb has good strength, better creep properties, corrosion resistance, superior irradiation performance and less hydrogen uptake as compared to Zircaloy-2 in same working condition. This alloy is used in form of thin tube in nuclear reactors. Thermo-mechanical processing to get final product involve: hot

---

* Corresponding author.
E-mail address: vivekfmt@iitr.ac.in

Selection and peer review under responsibility of the Gokaraju Rangaraju Institute of Engineering and Technology (GRIET)
doi:10.1016/j.mspro.2014.07.035

working of cast material, few cold working steps, annealing, and finally cold working to get desired strength, microstructure and dimensional tolerance. In high temperature processing forging and extrusion are important processes to get desired microstructure for further processing after breaking the cast structure [Chakravartty J.K., Dey G.K., Banerjee S., Prasad Y.V.R.K., 1995, Chakravartti J.K., Prasad Y.V.R.K., and Asundi M.K., 1991, Dayong Cai, Liangyin Xiong, Wenchang Liu, Guidong Sun, Mei Yao, 2007].

Forming of complex shape is difficult due to poor formability of this alloy, on account of limited temperature range of forging. The hot workability of alloy is also limited due to formation of various defects which may lead to gross failure [Ding R., Guo Z.X., Wilson A., 2002]. Therefore, characterization of deformation behavior is essential for the optimization of hot working parameters. The effect of thermo-mechanical parameters like strain, strain rate and temperature, on the final microstructure of Zr alloys have been widely studied on the basis of simulations and/ or experiments [D. Padmavardhani and Y.V.R.K. Prasad, 1991, Hurst D.G., 1997, Kapoor R., Chakravartty J.K., Gupta C.C., Wadekar S.L., 2005, Kapoor R., Chakravartty J. K., 2002].

The Dynamic Material Model is a powerful tool to develop the processing maps that helps in identifying stable or unstable hot working condition. Several unstable mechanisms were found to be related to processes such as adiabatic shear band formation, flow localization and dislocation-solute interaction (DSA); the final product with these defects shows poor mechanical properties. Thus the unstable domain should be avoided during hot working process. The safe domain observed in the processing map is usually associated with dynamic recrystallization (DRX) which is favored since DRX enhances intrinsic workability [Kartika Ika, Li Yunping, Matsumoto Hiroaki and Chiba Akihiko, 2009]. Domains can be classified on the basis of efficiency of power dissipation as superplasticity, DRX, dynamic recovery and internal fracture. DRX has been reported with peak efficiency of 50% at temperature of 750°C and strain rate of $1\times10^{-3}s^{-1}$ during the hot deformation of β-quenched Zr-2.5Nb-0.5Cu alloy [Chakravartti J.K., Prasad Y.V.R.K., and Asundi M.K., 1991], while in α-zirconium, optimum hot working parameter containing DRX mechanism obtained at 800°C and $0.1s^{-1}$ with 40% efficiency of power dissipation [Lei L., Huang X., Wang M., Wang L., Qin J., Lu S., 2011]. β quenched Zr-1Nb alloy showed dynamic recovery at temperature of 950°C and strain rate of $0.1s^{-1}$ with peak efficiency of 22%, whereas at temperature of 730°C and strain rate of $1\times10^{-3}s^{-1}$ it showed DRX with peak efficiency of 24% [Malinov S., Sha W., McKeown J.J., 2001].

The aim of this research is to find a safe and optimum workability window for forged and β-quenched Zr-2.5Nb alloy using processing maps and instability map and to bring out effect of strain.

2. Experimental Procedure

As-received Zr-2.5Nb alloy was obtained in the β quenched condition after forging of as-cast material. Hot compression test were performed on cylindrical specimens with 10 mm diameter and 15 mm height. A 1 mm chamfer of 45^0 was given to the edge of the face to avoid fold over in the initial stages of compression. Concentric grooves of 0.5 mm depth were machined at the both faces of samples to hold the lubricant properly. Graphite foil (5mil) was used to reduce the friction and avoid barreling.

Hot compression tests were conducted at the temperatures of 700, 750, 815, 850 and 925°C and at the constant true strain rates of 0.01, 0.1, 1, 5 and $10s^{-1}$ with the help of Gleeble-3800 Thermo Mechanical Simulator. The specimens were deformed up to true strain of about 0.69 and load-stroke data were recorded. Load-stroke data were converted to true stress-true plastic strain curves using standard equations. The flow stress values were obtained as a function of temperature, strain rate, and strain. The deformed specimens were sectioned along the compression axis and the cut surface was prepared by standard procedure for microstructural examination.

3. Results and Analysis

Power dissipation or efficiency maps: The domains in processing maps are generally determined by two methods; one is correlating the efficiency variation with respect to strain rate and temperature, and the other one is, the ductility and the microstructure changes that occur in the deformed specimens. As per the atomistic processing map of Raj [Raj R., 1981], the domain may correspond to any one of the following processes; superplasticity, DRX or dynamic recovery. For fine grain Zr-2.5Nb alloy, superplasticity occurs when the efficiency of power dissipation is greater than 60% and in some cases it is reported to be 90%. For the DRX, the efficiency is lower than superplasticity and may vary depending upon material and constituent phases. For dynamic recovery, the efficiency is less than DRX [Chakravartti J.K., Prasad Y.V.R.K., and Asundi M.K., 1991, Semiatin S.L., Seetharaman V., Weiss I.,1998].

Power dissipation maps obtained at two different strains (0.2 and 0.5) are shown in Fig. 1 and Fig. 2 respectively. The efficiency of power dissipation is represented in form of contours. The maps exhibit three different domains:

- Two domains with their peak efficiency of 54-60% and 49-54% are obtained in power dissipation map at 0.2 strain. First one is around 750°C and $1\times10^{-2}\,s^{-1}$ strain rate and other is around 925°C and $1\times10^{-2}\,s^{-1}$ strain rate. The domain around temperature of 750°C lies in ($\alpha+\beta$) phase field.
- A domain with its peak efficiency 44-50% at about 750°C and strain rate of $1\times10^{-2}\,s^{-1}$ obtained in power dissipation map of strain 0.5.

Comparison of power dissipation maps at strain of 0.2 and 0.5 brings out that the peak efficiency is decreasing from 0.6 to 0.5 with increase in strain. Higher efficiency of power dissipation is usually associated with DRX [Chakravartti J.K., Prasad Y.V.R.K., and Asundi M.K., 1991, Lei L., Huang X., Wang M., Wang L., Qin J., Lu S., 2011]. It appears that recrystallization is dominating during early part of deformation and in later part recovery is dominating.

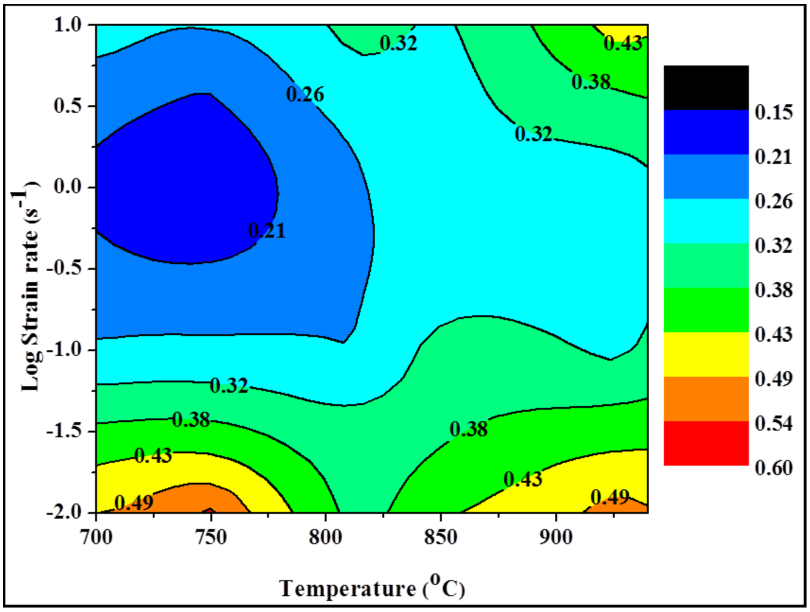

Fig.1: Power dissipation map at 0.2 strain, red colour indicate peak efficiency whereas blue colour indicate low efficiency of power dissipation.

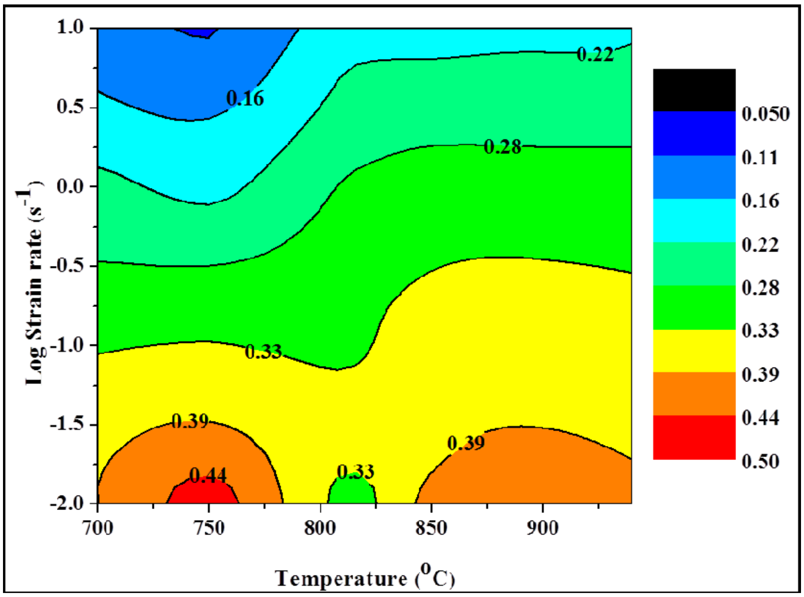

Fig.2: Power dissipation map at 0.5 strain, red colour indicate peak efficiency whereas blue colour indicate low efficiency of power dissipation.

The domains at temperature of 750°C and strain rate of 1×10^{-2} s^{-1} having the peak efficiency lies in two phase field, thus hot deformation characteristics of both phases have to be considered. However, in a recent study, it is reported that the harder phase dominates the controlling mechanism for hot deformation of a two phase alloy [Malinov S., Sha W., McKeown J.J., 2001]. According to Raj [Sarkar A., Chakravartty J.K., 2013], superplasticity occurs at higher efficiency i.e. more than 60%, but the domain of 750°C and strain rate 1×10^{-2} s^{-1} has maximum efficiency of 60%, which may indicate dynamic recrystallization (DRX) only. Therefore we can say that the hot working at temperature of 750°C and strain rate of 1×10^{-2} s^{-1} will be optimum condition for forged, β-quenched Zr-2.5Nb alloy. While Kapoor and Chakravartty [Chakravartty J.K., Dey G.K., Banerjee S., Prasad Y.V.R.K., 1995], reported optimum hot working condition for extruded Zr-2.5Nb at temperature of 1102°C and strain rate of 2×10^{-3} s^{-1}.

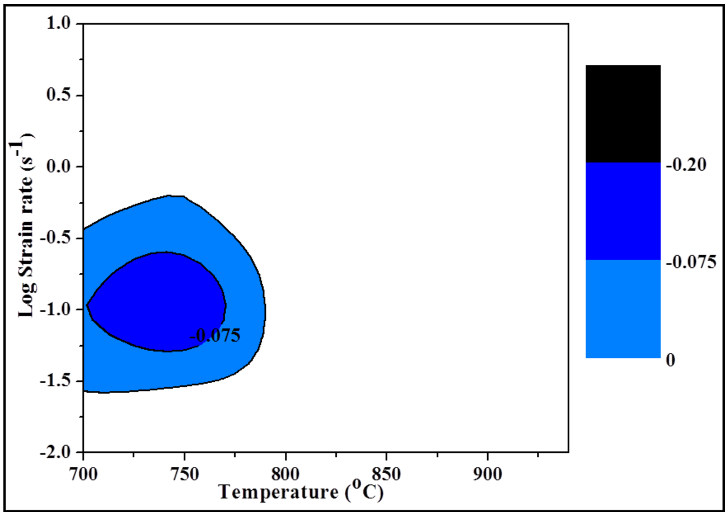

Fig.3: Instability map at 0.2 strain, blue colour domain shows instability as its efficiency is negative at temperature about 725°C and strain rate $0.1s^{-1}$.

The instability maps i.e. the variation of ξwith respect to strain rate and temperature at strains of 0.2 and 0.5 are shown in Figs. 3 and 4 respectively. According to Gegel's flow instability theory, $\xi \leq 0$ represents unstable state or flow instability in the material. The domain will be stable and material will deform uniformly, if the ξ value is greater than zero. If the ξ value lies between -1 to 0, the domain will be mixture of stable and unstable deformation: called as metastable regime. If the ξ value is lower than -1, deformation will be unstable. In the unstable domain, material normally exhibits instabilities in terms of flow localization, adiabatic shear band formation, and dislocation-solute interaction (DSA). During degradation in mechanical properties and shaping, these instabilities affect the formability of materials [Chakravartti J.K., Prasad Y.V.R.K., and Asundi M.K., 1991].

At strain 0.2, instability region lie at temperature of about 725°C and strain rate of 3×10^{-2} to 3×10^{-1} s^{-1}, which is in (α+β) phase field. While at strain 0.5, this instability region lies at temperature range of 700-925°C and strain rate range of 3×10^{-1} to $10s^{-1}$, which is in (α+β) and β-phase field. Thus, this material exhibits flow instabilities in (α+β) and β- phase field. Investigation reveals that unstable region is shifting towards higher strain rates and wide range of temperature with increase in strain.

4. Conclusion

The hot deformation characteristics of forged and β-quenched Zr-2.5Nb alloy was studied using hot compression testing in temperature range of 700-925°C and constant true strain rate range of 1×10^{-2} to 1×10^{1} s^{-1}. Power dissipation and instability maps are drawn on the basis of data generated and interpreted with the help of Dynamic Material Model. The results of this study are summarized as follows.

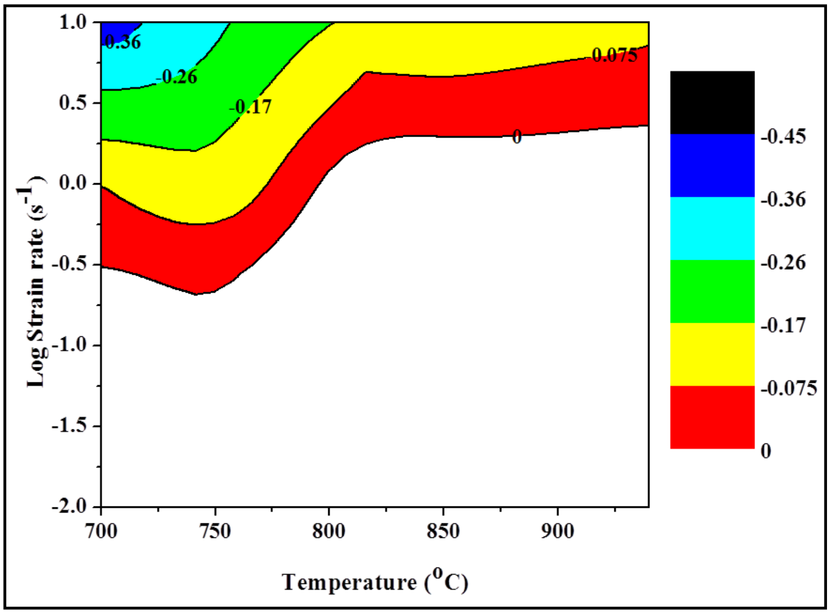

Fig.4: Instability map at 0.5 strain, blue colour domain shows highest instability zone as its efficiency is much negative at temperature about 700°C and strain rate $10s^{-1}$.

- The power dissipation map of strain 0.2 exhibits two domains with their peak efficiency of 54-60% and 49-54%, one is at about 750°C and strain rate of 1×10^{-2} s^{-1}, which lies is in (α+β) phase field, while other domain at about 925°C and strain rate of 1×10^{-2} s^{-1}, which lies in β phase field. But in power dissipation map of strain 0.5, domain with its peak efficiency of 44-50% exhibits at about 750°C and $1\times10^{-2}s^{-1}$ strain rate, which also lies in (α+β) phase field. These are the optimum condition for hot working.

- The instability map of strain 0.2 shows the instable domain at temperatures 725°C and strain rates of 3×10^{-2} to 3×10^{-1} s^{-1}, which is in (α+β) phase field, While at strain of 0.5, the instability parameter is negative in the domain of temperature at about 700-925°C and strain rate of 3×10^{-1} to 10 s^{-1}. These two domains are shows unstable flow during hot working. This region should be avoided during hot working.
- Peak efficiency of power dissipation decreases with increase in strain whereas area of instable region increases.

Acknowledgements

The author wish to acknowledge the financial support from the BRNS, Department of Atomic Energy, India.

References

Bruschi S., Poggio S., Quadrini F., Tata M.E., 2004. Workability of Ti–6Al–4V alloy at high temperatures and strain rates. Materials Letters 58, 3622-3629.

Chakravartty J.K., Dey G.K., Banerjee S., Prasad Y.V.R.K., 1995. Characterization of hot deformation behaviour of Zr-2.5Nb-0.5Cu using processing maps. Journal of Nuclear Materials 218, 247-255.

Chakravartti J.K., Prasad Y.V.R.K., and Asundi M.K., 1991. Processing map for hot working of alpha-zirconium. Metallurgical Transactions A 22, 829-836.

Dayong Cai, Liangyin Xiong, Wenchang Liu, Guidong Sun, Mei Yao, 2007. Development of processing maps for a Ni-based superalloy. Materials Characterization 58, 941-946.

Ding R., Guo Z.X., Wilson A., 2002. Microstructural evolution of a Ti–6Al–4V alloy during thermomechanical processing. Materials Science & Engineering A, 327, 233-245.

D. Padmavardhani and Y.V.R.K. Prasad, 1991. Characterization of hot deformation behavior of brasses using processing maps: Part II. β Brass and α-β brass. Metallurgical Transactions 22A, 2993-3001

Hurst D.G., 1997. Canada Enters the Nuclear Age: A Technical History of Atomic Energy of Canada Limited as Seen from Its Research Laboratories: McGill-Queen's University Press.

Kapoor R., Chakravartty J.K., Gupta C.C., Wadekar S.L., 2005.Characterization of superplastic behaviour in the (α + β) phase field of Zr–2.5 wt.%Nb alloy**.**Materials Science & Engineering A, 392, 191-202.

Kapoor R., Chakravartty J. K., 2002. Characterization of hot deformation behaviour of Zr–2.5Nb in β phase. Journal of Nuclear Materials, 306, 126-133.

Kartika Ika, Li Yunping, Matsumoto Hiroaki and Chiba Akihiko, 2009. Constructing Processing Maps for Hot Working of Co-Ni-Cr-Mo Superalloy. Materials Transactions, 50(9), 2277-2284.

Lei L., Huang X., Wang M., Wang L., Qin J., Lu S., 2011. Effect of temperature on deformation behavior and microstructures of TC11 titanium alloy. Materials Science & Engineering A 528(28), 8236-8243.

Malinov S., Sha W., McKeown J.J., 2001. Modelling the correlation between processing parameters and properties in titanium alloys using artificial neural network. Computational Material Science, 21, 375-394.

Raj R., 1981. Development of a processing map for use in warm-forming and hot-forming process, Metallurgical Transactions A, 12, 1089–1097.

Sarkar A., Chakravartty J.K., 2013. Hot deformation behavior of Zr–1Nb alloy: Characterization by processing map. Journal of Nuclear Materials 440, 136-142.

Semiatin S.L., Seetharaman V., Weiss I.,1998.Hot workability of titanium and titanium aluminide alloys—an overview. Materials Science & Engineering A, 243, 1-24.

PHYSICAL BASED CREEP STRAIN MODELLING OF 9CR MARTENSITIC STEEL

Surya Deo Yadav, Monika Schuler, Christof Sommitsch, Cecilia Poletti

Institute for Materials Science and Welding, Graz University of Technology,
Kopernikusgasse 24, A-8010 Graz, Austria

Email: surya.yadav@tugraz.at, monika.schuler@tugraz.at, christof.sommitsch@tugraz.at,
cecilia.poletti@tugraz.at

ABSTRACT

The development of appropriate models is indispensable to understand and describe the behaviour of materials under creep conditions to predict service life time. P91 is a complex 9% Cr steel having $M_{23}C_6$ decorated along prior austenitic grain boundaries, lath and packet boundaries. Additionally MX type fine carbonitrides are spread throughout the matrix. Microstructural evolution takes place when these steels are loaded at high temperatures and main features are: coarsening and transformation of precipitates, subgrain formation and growth. In present work experimental creep curves of P91 steel were compared with physical model based creep curves at different stress levels and temperatures. The model describes three types of dislocations: mobile and dipole and boundaries dislocations. The precipitation state is simulated using MatCalc software and is assumed to remain unchanged during creep. The evolution of subgrain size was studied comparing the experimental results with numerical simulation.

Keywords: P91, Martensitic steel, Creep strain modelling, Subgrain growth, Dislocation density

INTRODUCTION

The needs of modern society strongly rely on electricity and life without electrical energy is rather difficult. Although there is significant advancement in the area of renewable energy, still the requirement of world electricity strongly depends on fossil power plants. The exhaust gases from the fossil power plants are responsible for acidification in atmosphere and are the major concern in present time. Therefore, the efficiency of power plants must be raised. This can be done by increasing the steam temperature, in order to decrease the emission and fulfil the power necessitate. The power plants utilize huge amount of steels for steam tubes with good weldability, creep and corrosion resistance [1]. 9-12% Cr steels are the well-known suitable candidates for these applications [2]. Their high temperature strength depends on the precipitation state, the substructure and solid solution hardening. The role of the precipitates is to hinder the dislocation movement as well as to retard the growth of subgrains. These precipitates can coarse, or be formed of new phases at expense of useful dispersion hardening precipitates when exposed to a load at high temperatures [3]. On the other hand, creep conditions result in dynamic recovery due to annihilation and re-arrangement of dislocations, transforming the martensitic laths into more equiaxed grains [1].The synergistic effect of these processes (precipitates and structure changes) drives the materials towards softening first, and failure afterwards.

Microstructural modelling gives a better understanding of the response of materials throughout service time. The time span of steady state creep can be predicted easily when modelling is coupled with experimental results and thus the extrapolation to predict safe life can be more precise. The model, based on physical behaviour such as dislocation density and precipitation evolution, gives a deep insight about the material response during service. The martensitic steels have a complex microstructure, which can be described by different types of dislocations. A simple approach assuming one type of dislocation density cannot represent the complex dislocation structure within the martensitic structure [4].

In the present work, modelling of creep strain for P91 steel was carried out considering the dislocation density evolution during service time. Three categories of dislocations, i.e. mobile, dipole and boundary dislocations were considered. The initial precipitation state was simulated by using MatCalc; both lath size and dislocation density were used as input parameters for the numerical simulation. Finally, the model was validated with own creep curve and data from literature, as well as by microstructural characterization.

MATERIAL AND EXPERIMENTAL METHODS

The chemical composition of the tested P91 steel is given in table 1. The material was produced by tube rolling, normalized at 1060ºC for 30 min, air cooled, 60 min tempered at 770ºC and air cooled. The creep specimens were machined with an aspect ratio of five and loaded for 7000 and 9000 hours at 650ºC with an initial tensile stress of 60MPa. The creep strain was measured using the interrupted strain measurement technique according to the EN ISO 204:2009 standard. Field emission gun scanning electron microscope (FEI Quanta 200 FEGSEM) was employed for microstructural investigations.

Table 1 Chemical composition (wt.%) of P91 steel

C	**Si**	**Mn**	**P**	**S**	**Cr**	**Mo**	**Ni**	**Al**	**Nb**	**V**	**N**	**Fe**
0.12	0.3	0.45	0.013	0.003	8.23	0.98	0.13	0.014	0.06	0.22	0.041	Balance

Furthermore two creep curves, first at 80MPa, 600ºC and second at 80MPa, 650ºC from literature were used to validate the model.

MATCALC SIMULATION

The precipitation state of as received material was simulated with the help of MatCalc [5-6] software. The software is based on CALPHAD and the solid state transformation approach. The precipitation kinetics along the whole process (see fig. 1) chain was calculated considering:

- Grain boundaries and dislocations as potential nucleation sites.
- Initial grain size of austenite to be 50µm.
- Martensitic subgrains size 0.2µm.
- Thermodynamic database: mc_fe_v2.016.tdb.
- Mobility database: mc_fe_v2.001.ddb.
- Initial dislocation density of austenite $10^{11}m^{-2}$.
- Initial dislocation density of martensite $10^{15}m^{-2}$.

Figure 1 depicts the heat treatment carried out on the material as described in section 2.

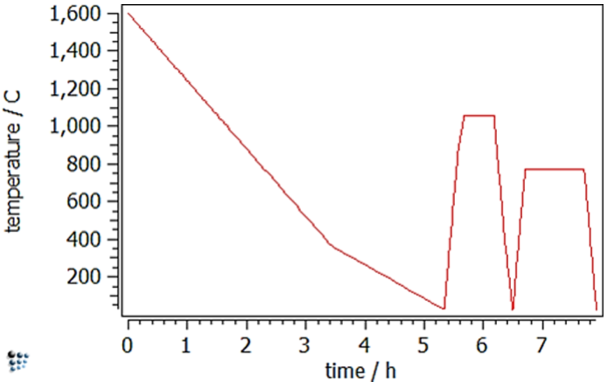

Figure 1 Heat treatment before creep loading

MODELLING OF CREEP STRAIN AND DISLOCATION DENSITY EVOLUTION

Creep Strain

When materials are loaded at high temperatures, the microstructural evolution can be described by dislocation dynamics considering reactions such as (a) multiplication of dislocations, (b) emission of dislocations from subgrain wall, (c) annihilation of dislocations, (d) immobilization, and (e) subgrain growth. A modified model developed by Ghoniem *et. al.* [7] later used by Krumphals *et. al.* [8-10] was used for the creep strain modelling. In the present work an advanced model is presented. Firstly a new term related to the depletion of dipole dislocations by transforming into boundary dislocation was introduced and secondly the constant beta was removed improving the physical interpretation.

The macroscopic creep strain rate is defined by the Orowan equation as:

$$\frac{d\varepsilon}{dt} = \frac{b}{M} \cdot \rho_m \cdot v_g \qquad (1)$$

Where b is the Burgers vector, v_g the glide velocity of dislocations, M the Taylor factor and ρ_m is the mobile dislocation density.

Dislocation Densities Model

The total dislocation density was divided in to three categories: mobile (ρ_m), dipole (ρ_{dip}) and boundary (grains and subgrains) (ρ_b) dislocations.
The rate of change of the mobile dislocation density can be given as a production term due to the interaction of mobile dislocation plus the emission from subgrain walls minus a consumption term due to annihilation at subgrain walls, static recovery and dynamic recovery:

$$\frac{d\rho_m}{dt} = \left[\frac{v_g}{h_m} \cdot \rho_m\right] + \left[\frac{v_g}{h_b} \cdot R_{sbg}\right] - \left[\frac{v_g}{2R_{sbg}} \cdot \rho_m\right] - \left[8{\rho_m}^{3/2} v_{cm}\right] - \left[d_{anh} \cdot (\rho_m + \rho_{dip}) \cdot \rho_m \cdot v_g\right] \qquad (2)$$

In the above equation R_{sbg} is the subgrain radius, $h_m = 1/\sqrt{\rho_m}$ the dislocation spacing of mobile dislocations [11], h_b the dislocation spacing within walls, ρ_{dip} the dipole dislocation

density, v_{cm} the climb velocity of mobile dislocation and d_{anh} is the length parameter for spontaneous annihilation [7].
Furthermore, the rate of change of the dipole dislocation density can also be expressed as a production term, in this case due to an immobilization rate of mobile dislocations at subgrain walls minus the conversion into boundary dislocations, static recovery and dynamic recovery:

$$\frac{d\rho_{dip}}{dt} = \left[\frac{v_g}{2R_{sbg}} \cdot \rho_m\right] - \left[\frac{v_{cd}}{h_b} \cdot \rho_{dip}\right] - \left[\frac{\rho_{dip}}{h_{dip}} \cdot v_{cd}\right] - \left[d_{anh} \cdot \rho_{dip} \cdot \rho_m \cdot v_g\right] \qquad (3)$$

Being v_{cd} the climb velocity of dipole dislocations.

Finally, the evolution of the boundary dislocation density is given by the conversion of dipole dislocations minus the formation of new subgrain surface:

$$\frac{d\rho_b}{dt} = K \cdot \left[\frac{v_{cd}}{h_b} \cdot \rho_{dip}\right] - M_{sb} \cdot \left[P_{sb} - 2\pi \cdot \left(\sum_{i=1}^{8} r_{mean,i}^2 \cdot N_{v,i}\right) \cdot \gamma_{sb}\right] \frac{\rho_m}{R_{sbg}} \qquad (4)$$

with K being a constant, M_{sb} the mobility of subgrains, P_{sb} the pressure for subgrain growth, r_{mean} the mean radius of precipitates, N_v the number density of precipitates and γ_{sb} is surface energy of subgrain boundary [7].

Subgrain Growth

In many steels, the formation of dislocation cells and subgrain boundaries takes place during high temperature deformation [12-13]. Thus, the behaviour of subgrains is incorporated in the model.

The growth rate is assumed to be the difference of the growth by a decrease in surface energy and a shrinkage due to subgrain nucleation.

Or,

$$\frac{dR_{sbg}}{dt} = M_{sb}\left[P_{sb} - 2\pi \cdot \left(\sum_{i=1}^{8} r_{mean,i}^2 \cdot N_{v,i}\right) \cdot \gamma_{sb}\right] - G\eta_v K_c R_{sbg}\left[(\rho_m + \rho_{dip})^{1/2} - \frac{K_c}{R_{sbg}}\right]\frac{\Omega D_s}{kT} \qquad (5)$$

Where G is the shear modulus, η_v the transfer coefficient of vacancies from dislocation cores to jogs, K_c a constant with value 10, Ω the atomic volume, D_s the lattice self-diffusion coefficient, k the Boltzmann constant and T is temperature. These equations were solved simultaneously [14] using Matlab software package to evaluate mobile dislocation density, dipole dislocation density boundary, dislocation density, subgrain size and creep strain [7-14].

RESULTS AND DISCUSSION

Precipitate Evolution

Fig. 2a depicts the mean radius evolution while fig. 2b shows the number density of precipitates during tempering with regard to fig. 1. The precipitates considered in the simulation were AlN, M_3C_7, $M_{23}C_6$, MX type carbo-nitrides and Laves phase. The main precipitates, which remained after tempering were MX, M_3C_7, $M_{23}C_6$ and Laves phase. These results, i.e. mean radius and number density, were taken as input parameters for the numerical simulation of the Zener drag. It could be observed the precipitates number density and mean radius are reaching nearly a constant value during tempering stage.

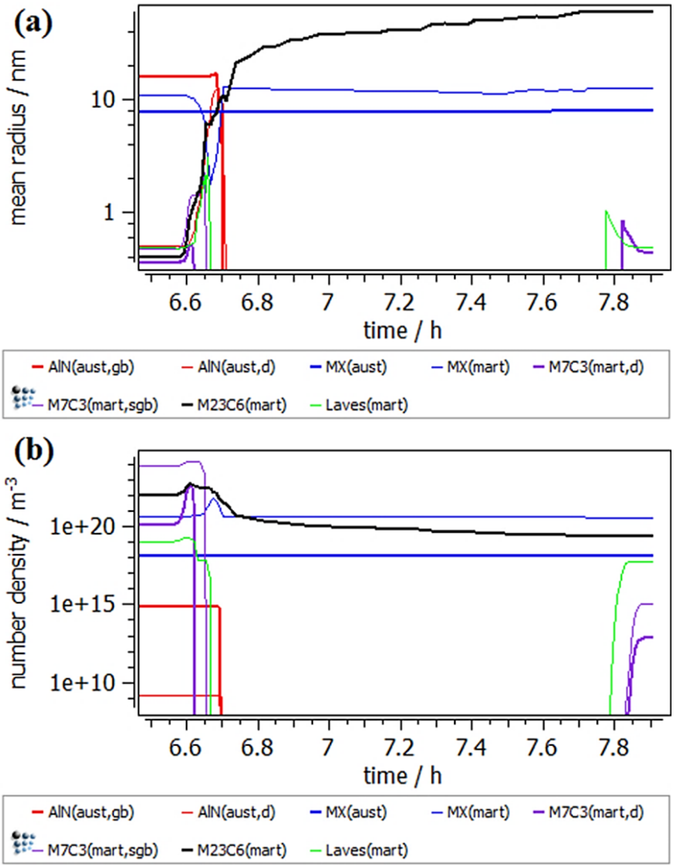

Figure 2 Evolution of (a) number density and (b) mean radius of precipitates during heat treatment

Dislocation Density

The numerical simulation was carried out applying the creep conditions described in section 2 (80MPa at 600ºC, 60MPa at 650ºC and 80MPa at 650ºC). The initial dislocation densities were set to $\rho_m = 0.5 \times 10^{14}$, $\rho_{dip} = 0.3 \times 10^{14}$ and $\rho_b = 0.2 \times 10^{14} m^{-2}$ while a subgrain size of 0.2μm was chosen for the simulation.

Fig. 3 depicts the simulation results at 80MPa and 600ºC showing the evolution of mobile, dipole and boundary dislocations densities as a function of time. After 10,000 hours of creep exposure, a steady state was achieved. Fig. 3b is a magnified view of the marked rectangular area in fig. 3a. The initial mobile dislocation density is high, and it decreases with exposure time due to the spontaneous annihilation and formation of new dipoles. These pre-existing dipoles and newly produced dipoles are annihilated as well as swept into the boundaries. Thus, the boundary dislocation density increases at the beginning when dipoles are accumulate at the boundaries and are converted to boundary dislocations (see fig. 3b). Furthermore, the boundary dislocation decreases afterwards due to subgrain growth. The total dislocation density (see fig. 3c) is decreased from 10^{15} to 0.8×10^{14}, which is quite close to the reported experimental value of $1.8 \pm 1.7 \times 10^{14}$ by Panait *et. al.* [2].

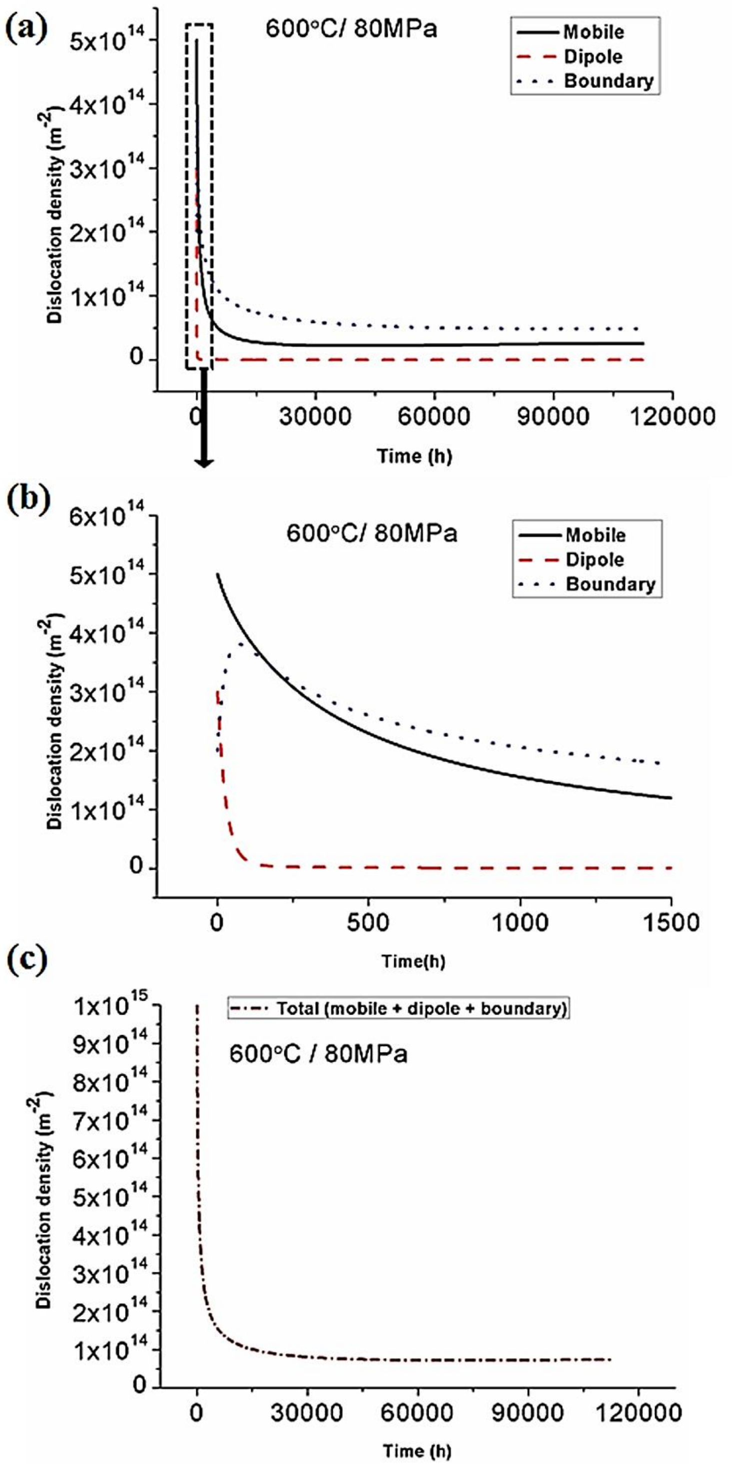

Figure 3 Evolution of dislocation density after 112,528 hours of creep loading (a) mobile, dipole and boundary, (b) detail of (a) for 1500 hours, and (c) total dislocation density

The simulation shows a similar trend of the total dislocation density with exposure time in different creep conditions (see fig. 4); however the dislocation density in case of 80MPa at 600ºC was lowest.

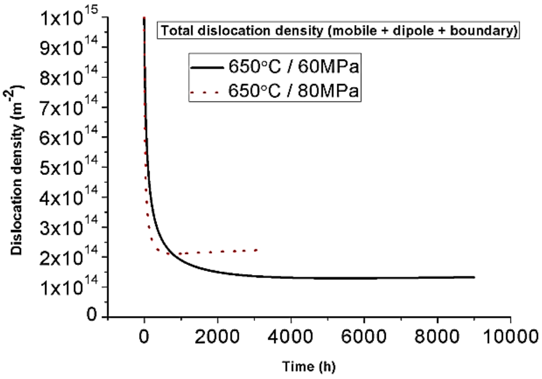

Figure 4 Evolution of the total dislocation density after 3200 and 9000 hours of creep loading

Creep Strain

Figure 5 depicts the creep curves simulated at different stresses and temperatures. The modelled creep curves show a very good agreement with own experimental curves, as well as from the literature, up to the secondary stage of creep, and deviate in the tertiary one. The tertiary stage is controlled by glide as well as damage triggered by cavity formation, agglomeration and crack propagation [15], which is so far not considered in the model.

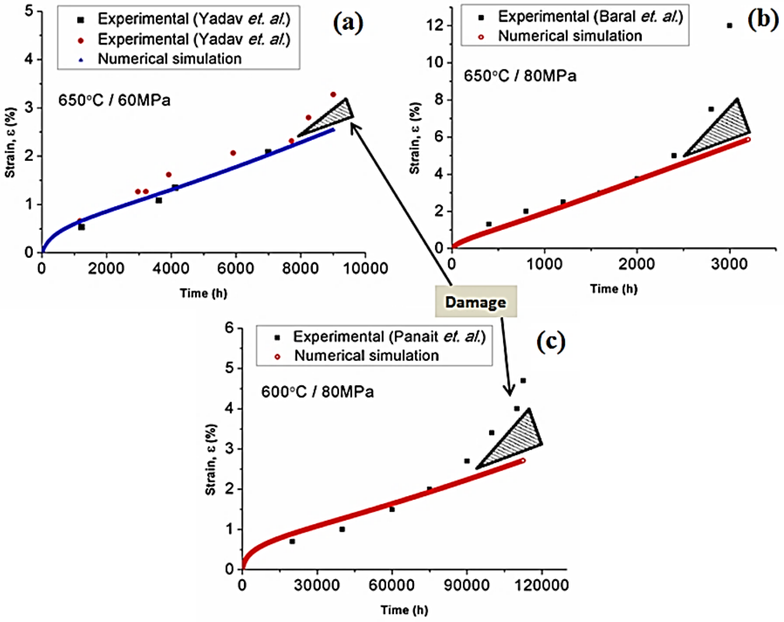

Figure 5 Simulated and experimental [15-16, 2] creep curves of P91 (a) 650ºC, 60MPa for 9000hours (b) 650ºC, 80MPa for 3200hours (c) 600ºC, 80MPa for 112,528 hours

Subgrain Growth

Figure 6a depicts the evolution of subgrain size with creep exposure time resulted from numerical simulation in different stress conditions, which shows a higher creep rate at higher stress. The subgrain size increased from 0.2µm to 1.8µm after 7000 hours of exposure at 650°C and 60MPa. Fig. 6b shows the FEG-SEM image of real 7000 hours crept specimen at the same conditions and it could be observed that subgrains are in the range of 1-3µm, validating the model. The subgrain size was larger in case of higher temperature at constant stress level (see fig. 6a and 6c).

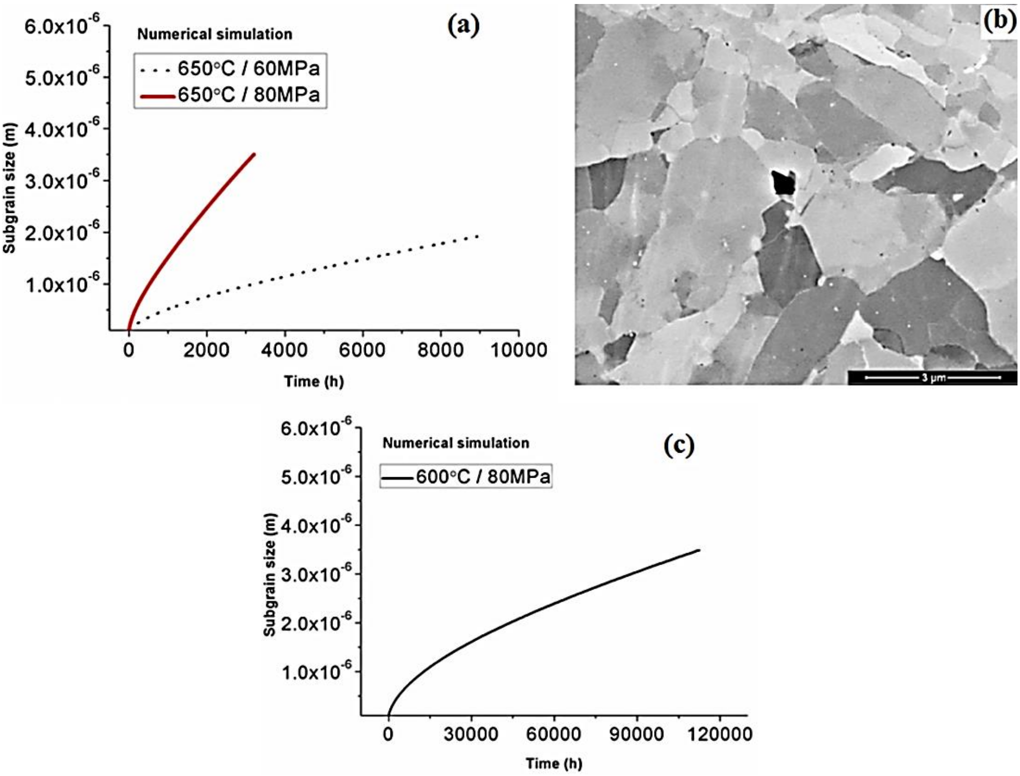

Figure 6 Subgrain growth during creep exposure simulation (a) and (c); (b) FEG-SEM image of 7000 hours creep loaded specimen at 600°C and 60MPa

SUMMARY AND CONCLUSIONS

A model was developed to describe the creep behaviour in P91 steels based on rate equations of three types of dislocation densities and taking into account the initial precipitation state. The model can predict the microstructure, by calculating the evolution of the dislocation density and the subgrain size during the service life time and creep exposure. The numerically simulated creep curves are validated with experimental curves up to the secondary stage and deviate in the tertiary creep stage due to ongoing creep damage, which is not taken into account so far in the present model.

ACKNOWLEDGMENTS

The modelling part of the presented research was carried out under the project Z-Ultra: 309916, “Z phase strengthened steels for ultra-supercritical power plants” and the experimental activities were carried out under the project Hot Pipes: 826434, “Entwicklung eines SHM-Systems für die Überwachung von Hochtemperatur-Rohrleitungen in Kraftwerken”. The authors would like to thanks, the FFG- Austrian Research Promotion Agency and the European commission for their financial support.

REFERENCES

[1] Barkar T., Agren J., “Creep simulation of 9-12% Cr steels using the composite model with thermodynamically calculated input,” *Materials Science and Engineering A*, Vol. 395, (2005), pp. 110-115.

[2] Panait C. G., Zielinska-Lipiec A., Koziel T., Czyrska-Filemonowicz A., Gourgues-Lorenzon A., Bendick W., “Evolution of dislocation density, size of subgrains and MX-type precipitates in a P91 steel during creep and during thermal ageing at 600 ºC for more than 100,000 h,” *Materials Science and Engineering A*, Vol. 527, (2010), pp. 4062-4069.

[3] Danielsen H. K., Hald J., “Behaviour of Z phase in 9-12% Cr steels,” *Energy Materials*, Vol. 1, (2006), pp. 49-57.

[4] Magnusson H., Sandström R., “Creep strain modelling of 9-12 Pct Cr steels based on microstructure evolution,” *Metallurgical and Materials Transactions A*, Vol. 38A, (2007), pp. 2033-2039.

[5] Kozeschnik E., Svoboda J., Fratzl P., Fischer F.D., “Modelling of kinetics in multi-component multi-phase systems with spherical precipitates: II: Numerical solution and application”, *Materials Science and Engineering A*, Vol. 385, (2004), pp. 157-165.

[6] http://matcalc.tuwien.ac.at/

[7] Ghoniem N., Matthews J., Amodeo R., “A dislocation model for creep in engineering materials,” *Res Mechanica*, Vol. 29, (1990), pp. 197-219.

[8] Krumphals F., Wurmbauer H., Wieser V., Sommitsch C., “Modelling the microstructure evolution of a ferritic hot work tool steel during short-term creep,” *Proc. MMM2010*, 5th Conf. on Multiscale Materials Modelling, Freiburg, Germany 2010, pp. 458-461.

[9] Krumphals F., Reggiani B., Donati L., Wlanis T., Sommitsch C., “Deformation behaviour of a ferritic hot-work tool steel with respect to the microstructure,” *Computational Materials Science*, Vol. 52, (2012), pp. 40-45.

[10] Krumphals F., Wlanis T., Sommitsch C., Holzer I., Sonderegger B., Wieser V., *Computer Methods in Material Science*, Vol. 9 (2), (2009), pp. 228-233.

[11] Kocks U. F., “Laws for work-hardening and low-temperature creep,” *Journal of Engineering Materials and Technology*, Vol. 98 (1), (1976), pp. 76-85.

[12] Amodeo R. J., Ghoniem N. M., “A review of experimental observations and theoretical models of dislocation cells and subgrains,” *Res Mechanica,* Vol. 23, (1988), pp. 137-160.

[13] Takeuchi S., Argon A. S., “Steady state creep of single-phase crystalline matter at high temperature,” *Journal of Material Science*, Vol. 11, (1976), pp. 1542-1566.

[14] Krumphals F., “Physical based modelling of creep fatigue in hot work tool steels,” *Doctoral Thesis,* Graz University of Technology, Austria, 2014.

[15] Yadav S. D., Sonderegger B., Sartory B., Sommitsch C., Poletti C., “Characterization and quantification of cavities in 9Cr martensitic steel for power plants,” *Material Science and Technology,* under review.

[16] Baral J., Swaminathan J., Ghosh R.N., “Creep behaviour of 9CrMoNbV (P91) steel having a small amount of boron,” *Procedia Engineering,* Vol. 55, (2013), pp. 88-92.

Key Engineering Materials Vols 651-653 (2015) pp 783-788
© (2015) Trans Tech Publications, Switzerland
doi:10.4028/www.scientific.net/KEM.651-653.783

Submitted: 2014-12-09
Revised: 2015-02-03
Accepted: 2015-02-06

Hybrid processing of AZ91 Magnesium alloy/nano-Al_2O_3 composites

S. D. Yadav[1, a *], P. P. Bhingole[2,b], G. P. Chaudhari[2,c], S.K. Nath[2,d] and C. Sommitsch[1,e]

[1]Institute of Materials Science and Welding, Graz University of Technology, Graz, Austria

[2]Department of Metallurgical & Materials Engineering, Indian Institute of Technology, Roorkee, India

[a*]surya.yadav@tugraz.at, [b]pramod_bhingole@yahoo.com, [c]chaudfmt@iitr.ernet.in, [d]indiafmt@iitr.ernet.in, [e]christof.sommitsch@tugraz.at

Keywords: Metal matrix composites, Mechanical properties, Wear, Casting, Ultrasonic processing

Abstract. In the present work mechanical and wear behaviour of AZ91 magnesium alloy based composites, reinforced with nano-Al_2O_3 particles is studied. The composites with different amount of alumina particles are fabricated by a hybrid processing approach. The hybrid processing involved alumina particles dispersion in molten AZ91 alloy by mechanical stirring assisted with ultrasonic processing. Dry sliding wear tests are performed using a pin on disc apparatus against hardened steel at loads ranging from 4.9 N to 14.7 N. The microstructural investigation revealed that a refined microstructure is obtained because of the heterogeneous nucleation induced by ultrasonic processing and nano-Al_2O_3 dispersion. Hardness, yield strength and maximum compressive stress of the nanocomposites are found to be superior to that of the matrix alloy. The resistance against wear is increased due to incorporation of reinforced nano-Al_2O_3particles. The wear rate of nanocomposite is decreased with increasing the amount of the reinforcement. The identified wear mechanisms are abrasion and oxidation.

Introduction

Magnesium alloys are widely researched for prospective automotive and aerospace applications. They are the promising lightweight materials for achieving better fuel economy in transportation industry. Magnesium is the lightest structural metallic material having a density of about 2/3rd that of aluminium [1]. Magnesium based metal matrix composites (MMC's) have shown excellent mechanical, physical, and thermal properties and thus have found several applications in automotive and aerospace industries [2, 3]. Magnesium based composites having discontinuous reinforcements result in enhanced specific strength and stiffness, damping capacity, dimensional stability, and creep resistance [1]. In the present time aluminium based MMCs have been used for tribological applications such as cylinder liners, brake rotors and piston rings [4]. Being the lightest structural material, magnesium based MMCs could be a replacement for those applications and thus it is worth to study both wear and fabrication process of these composites [5, 6]. Several investigators have studied the wear behaviour of Mg alloy matrix composites [6, 7]. It was reported that the wear behaviour was dependent on the amount of reinforcement. Some studies highlight the more beneficial effect on mechanical and wear properties of composites when reinforced with the same amount of nanoparticles rather than the micron sized particles [1, 8]. However when it comes to the fabrication of nanocomposites, the processing of nanoparticle reinforced composites is difficult. Stir casting in which mechanical stirring is utilized for reinforcing the particles can give good distribution and dispersion of micron size particles. But in the case of nano size particles the specific surface area is high so it is very difficult to distribute and disperse these particles by conventional stirring methods [8]. Ultrasonic cavitation based solidification processing has shown some promising results for improved distribution and dispersion of nanoparticles [8-10]. The strong impact of cavity implosion coupled with local high temperature has the ability to break the micro clusters of nanoparticles [11].

In this research, hybrid processing consisting of mechanical stirring followed by ultrasonication of the melt is utilized in order to ensure a uniform dispersion of Al_2O_3 nanoparticles in the AZ91 magnesium alloy matrix. The effect of hybrid processing on the microstructural evolution is investigated in the laboratory cast composites. Mechanical and dry sliding wear properties of the resulting nanocomposites are determined and analysed.

Material and Methods

AZ91 alloy having a nominal composition (in wt pct) of 9 Al, 1 Zn, 0.25 Mn and balancing Mg was used as matrix material. 1 and 2 wt pct of γ-alumina (Al_2O_3) powder having an average particle size of 50 nm was used as reinforcement. A high power ultrasonic system, Model VCX 1500, Sonics and Materials, USA was used for fabricating the nanocomposites. The radiator was coated with zirconia baked at 100°C for inertness. In each experiment, 200 g of AZ91 alloy was melted in a mild steel crucible heated up to 700°C, in an argon atmosphere controlled electric resistance furnace. Nano alumina particles preheated at 300°C were added to the melt accompanied with mechanical stirring for 10 minutes (Fig. 1a).

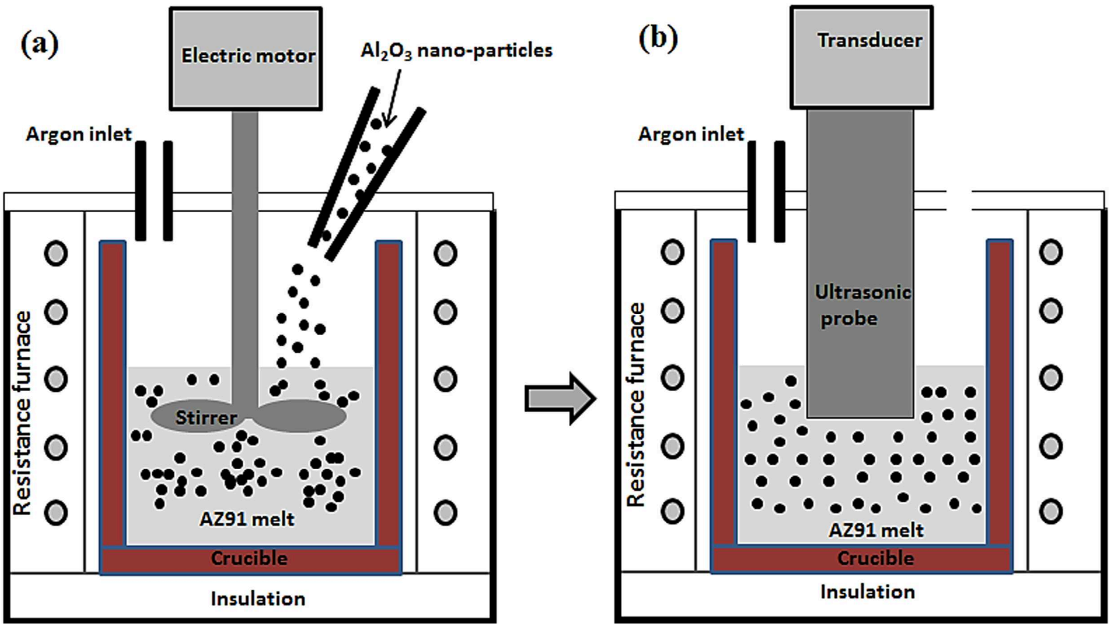

Figure 1 Schematic of fabrication process (a) Mechanical stirring (b) Ultrasonic processing

After stirring, an ultrasonic probe preheated at 700°C was lowered into the melt for ultrasonic processing (Fig. 1b). The duration of ultrasonic processing was 3 minute with an ultrasonic intensity of 5.40 $kWcm^{-2}$. After processing, the melt was water quenched. Microscopy was performed using a Leica DMI 5000M light optical microscope and a FEI-Quanta 200 FE-SEM scanning electron microscope. The mean linear intercept method was used to estimate the average grain size. Hardness was measured using a Vickers hardness tester applying 5 kgf load and 15 s dwell time. Compression test were performed at room temperature employing Gleeble® 3800 System. The specimens used for compression testing had a cross-section of 6 mm × 6 mm and a length of 12 mm [12]. The proof stress/yield strength (σ_{02}) was estimated from the stress strain data taking the flow stress at 0.2 pct offset strain, while σ_{max} was the maximum value of flow stress. Dry sliding wear tests were performed using 5 mm diameter and 15 mm long pin samples machined out from the castings. A pin-on-disc machine (M/s DUCOM, Bangalore, India) with counter face of a hardened and polished disc made of En-32 steel (HRC 62-65 hardness) was used for the wear tests. The weight loss of the pin was measured at different intervals of sliding time. Three normal loads 4.9 N, 9.8 N and 14.7 N were used with a constant sliding speed of 1 ms^{-1}.

Results and discussion

Microstructure. Figs. 2(a-c) show the light optical micrographs (LOM) of AZ91 alloy without reinforcement and with different amount of reinforcement. It can be seen that besides α-Mg phase (white), β-$Mg_{17}Al_{12}$ phase (black) is also present in all the castings, which is consistent with X-Ray diffraction analysis of the corresponding specimens (Fig. 2d).

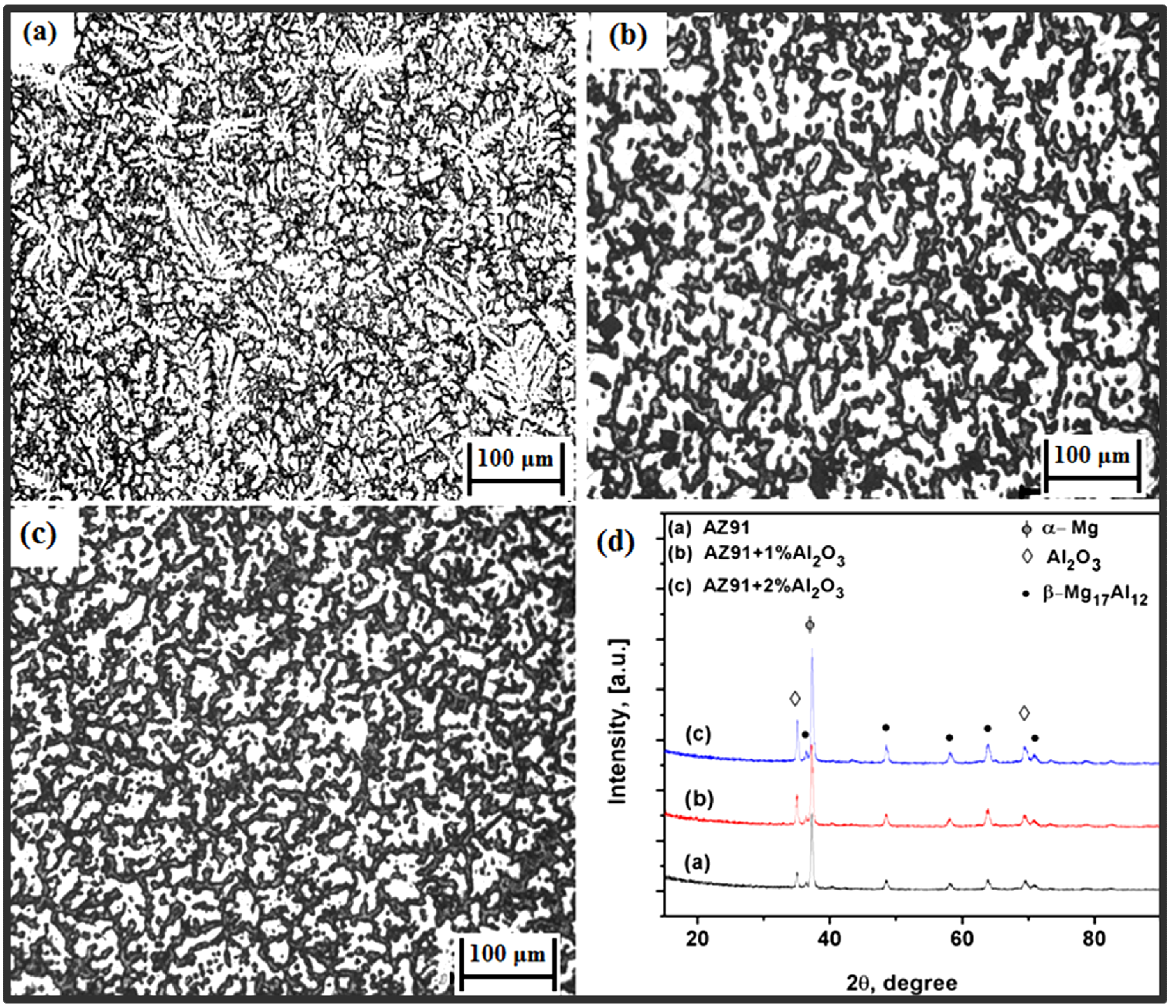

Figure 2 (a) Unprocessed AZ91 alloy (b) Hybrid processed 1 pct Al_2O_3/AZ91 composite (c) Hybrid processed 2 pct Al_2O_3/AZ91 composite (d) X-ray diffraction patterns of unprocessed AZ91 and hybrid processed nano-Al_2O_3/AZ91 alloy composites

In addition, Al_2O_3 diffraction peaks can also be seen in all the nanocomposites. From Fig. 2a, it is evident that the microstructure is predominantly interconnected by dendrites and consists of the primary α-Mg phase. The β-$Mg_{17}Al_{12}$ phase is distributed along the dendrite boundaries. From Figs. 2b and 2c it can be seen that the microstructure of the nanocomposites is less dendritic compared to that of the monolithic alloy. The grain size of the composite is decreased further with increasing the amount of reinforcement. The observed grain refinement can be attributed to a combination of various effects arising because of the presence of Al_2O_3 nanoparticles and an ultrasound induced cavitation phenomenon in the melt. Firstly, the nanoparticles in the melt can provide additional nucleation sites for enhanced heterogeneous nucleation during the solidification [10]. Secondly, reinforced particles can also retard the grain growth [7]. Furthermore, there is ultrasound induced grain refinement based on various mechanisms such as cavitation enhanced heterogeneous nucleation, cavitation enhanced wetting of nanoparticles, and cavitation induced endothermic vaporization of liquid inside the expanded cavities during their growth [13, 14].

Mechanical properties. Fig. 3a shows the true stress-true strain curves for AZ91 alloy and nano-Al_2O_3/AZ91 alloy composites. The variation of yield strength and hardness with the weight fraction of the reinforced particles is shown in Fig. 3b and Fig. 3c respectively. Mechanical properties like hardness, yield strength and maximum stress of the nanocomposites are better than that of the AZ91 base alloy. It is evident from Figs. 3a-c that the mechanical properties of nano-Al_2O_3/AZ91 composites are improved with increasing the amount of reinforcement. A nano alumina reinforcement of only 2 wt pct can increase the hardness by about 25% and proof stress by about 15%.

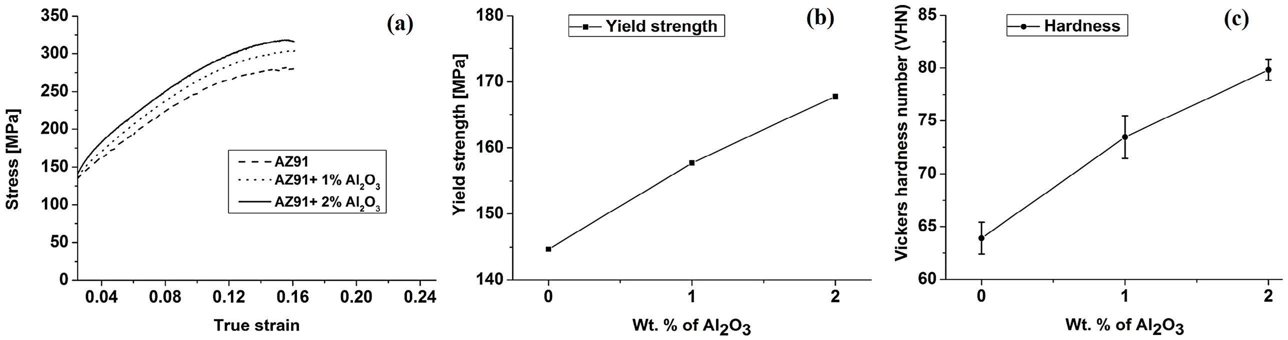

Figure 3 (a) True stress-true strain curves (b) Yield stress dependence on the amount of reinforcement (c) Hardness dependence on the amount of reinforcement

The yield strength can be explained on the basis of an analytical model [15], wherein strengthening is attributed to the Orowan strengthening effect [16], enhanced dislocation density, the load-bearing effect, and to the grain refinement. Orowan strengthening is effective in case of nanocomposites because of Orowan bowing phenomenon. Particles having a size of 10 to 100 nm are responsible for Orowan bowing mechanism [17, 18]. Since the alumina dispersoids having an average particle size of 50 nm are used in these hybrid processed composites, this mechanism is expected to contribute to the observed strengthening. The critical resolved shear stress of dispersion hardened alloys is given by: $\tau = Gb / (l-2r)$, where G, b, l, and r are the shear modulus, burgers vector, average particle spacing, and particle radius, respectively. The average particle spacing can be estimated as: $l = r / f^{1/2}$, where f is the volume fraction of dispersoids. Assuming that the entire amount of the added particles are dispersed in the melt, the average particle spacing, l, is estimated as 370 nm and 262 nm respectively, for 1 wt pct and 2 wt pct nano alumina reinforced composites. Since the critical resolved shear stress varies inversely as $(l-2r)$, we find that the 2 wt pct reinforced composite exhibits higher yield strength. Besides their contribution to the yield strength, the nano alumina disperoids also lead to a higher strain hardening [18]. This is evident from the Fig. 3a, wherein 1 wt pct and 2 wt pct nano-composites exhibit a larger strain hardening as compared to the unreinforced AZ91 alloy. In this work (Fig. 1), significant grain refinement is also observed, which results in further strengthening of the composites [11]. The observed increase in the yield strength of nanocomposites may be a result of synergy of grain refinement and Orowan strengthening.

Dry sliding wear behaviour. It is evident from Fig. 4a and 4b that the wear rate increases with an increase in the applied load for all the compositions. In addition, Fig. 4b shows that the wear rate decreases with an increase in the amount of nano-Al_2O_3 in the composites. With merely 2wt. pct of reinforcement, at 4.9 N load, there is about 13 pct reduction in wear rate as compared to that of the base alloy. The improvement in wear resistance is because of the nano-Al_2O_3 dispersoids, which act as load supporting elements [7] and also because of the strengthening as explained in section 'mechanical properties'. The worn surfaces of AZ91 alloy and 2 wt. pct nano-Al_2O_3/AZ91 composite tested under a load of 14.7 N are shown in Fig. 4c and 4d respectively.

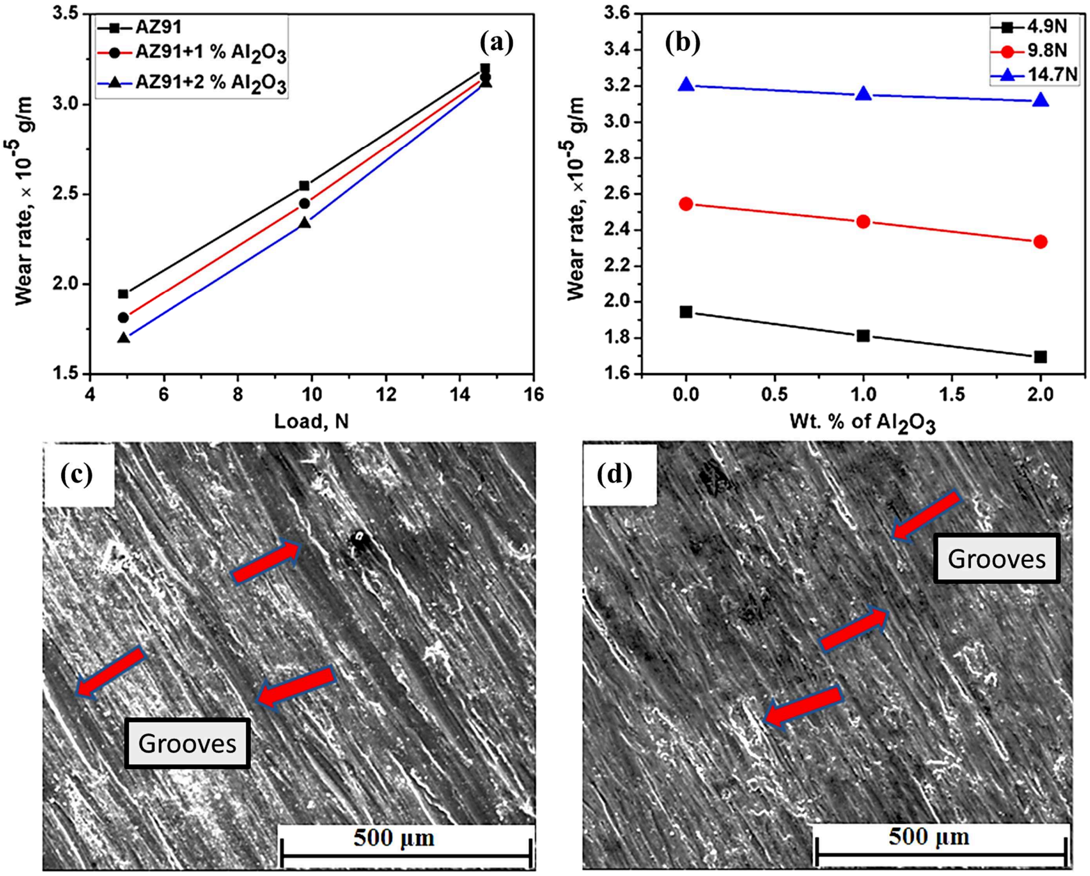

Figure 4 Wear rate of AZ91 and nano-Al_2O_3/AZ91 alloy composites as a function of (a) load and (b) amount of reinforcement; SEM micrograph of dry sliding wear tested specimens under a load of 14.7 N (a) AZ91 (b) 2 wt. pct Al_2O_3/AZ91 alloy composite

It is evident that the surface of AZ91 Mg alloy has deeper and wider grooves as compared to composite. These grooves are produced by the ploughing action of harder asperities on hardened steel counter face due to abrasion, which are further covered by an oxide layer. The surface is oxidised due to frictional heating. These are typical characteristics of abrasion followed by oxidative wear. These oxide layers are removed in form of fragments causing wear at the surface [6]. The formation of oxide layer and its breakage leads to wear along with abrasion [19]. Fig. 4d shows the worn surface of the composite and it can be seen that the composite has smaller grooves than the monolithic alloy.

Summary

AZ91 magnesium alloy composites reinforced with nano alumina particles were successfully fabricated by a hybrid processing approach consisting of mechanical stirring followed by ultrasonic processing. Hybrid processing of the melt refined the microstructure of the AZ91 alloy based nanocomposites. The observed grain refinement is attributed to an enhanced heterogeneous nucleation aided by a synergistic action of nano alumina particles dispersion and ultrasound induced cavitation and streaming effects. The hybrid processed nanocomposites exhibited better mechanical properties than the AZ91alloy. Yield strength, maximum compressive stress, hardness and resistance to the dry sliding wear of the nanocomposites were superior to those of the AZ91 alloy.

Acknowledgement

The author’s acknowledge SERC, Department of Science and Technology, Government of India and European Commission (Z-Ultra: 309916) for financial support. Special thanks to Prof. Cecilia Poletti for the encouragement to write the paper.

References

[1] C.Y.H. Lim, D.K. Leo, J.J.S. Ang, M. Gupta, Wear of magnesium composites reinforced with nano-sized alumina particulates, Wear, 259 (2005) 620-625.

[2] T. Imai, S.W. Lim, D. Jiang, Y. Nishida, Superplasticity of a AlN/Mg-5wt pct Al alloy composite made by a vortex method, Scr. Mater. 36 (1997) 611-616.

[3] Q.C. Jiang, X.L. Li, H.Y. Wang, Fabrication of TiC particulate reinforced magnesium matrix composites, Scr. Mater. 48 (2003) 713-717.

[4] H.K. Feng, S.R. Yu, Y.L. Li, L.Y. Gong, Microstructure and properties of Sip/Al–Si surface composites prepared by ultrasonic method, Mater. Des. 30 (2009) 2420-2424.

[5] P. Rohatgi, Cast aluminium-matrix composites for automotive applications, JOM 43 (1991) 10-15.

[6] C.Y.H. Lim, S.C. Lim, M. Gupta, Wear behavior of SiCp-reinforced magnesium matrix composites, Wear 255 (2003) 629-637.

[7] J. Yao, W. Li, L. Zhang, F. Wang M. Xue, H. Jiang, J. Lu, Wear mechanism for in situ TiC particle reinforced AZ91 magnesium matrix composites, Tribol. Lett. 38 (2010) 253-257.

[8] G. Cao, H. Konishi, X. Li, Recent development on ultrasonic cavitation based solidification processing of bulk magnesium nanocomposites, Int. J Metal Cast. 2(1) (2008) 57-68.

[9] H. Kumar, G.P. Chaudhari, Creep behavior of AS41 alloy matrix nano-composites, Mater. Sci. Eng. A 607 (2014) 435-444.

[10] G. Cao, H. Choi, H. Konishi, S. Kou, R. Lakes, X. Li, Mg-6Zn/1.5 pct SiC nanocomposites fabricated by ultrasonic cavitation-based solidification processing, J Mater. Sci. 43 (2008) 5521-5526.

[11] S. Suslick, Y. Didenko, M.M. Fang, T. Hyeon, K.J. Kolbeck, W.B. McNamara, M.M. Midleni, M.Wong, Acoustic cavitation and its chemical consequences, Phil Tans R Soc A 357 (1999) 335-353.

[12] Z. Trojanova, P. Lukac, Compressive deformation behavior of magnesium alloys. J Mater. Process Technol. 162-163 (2005) 416-421.

[13] B. Patel, G.P. Chaudhari, P.P. Bhingole, Microstructural evolution in ultrasonicated AS41 magnesium alloy, Mater. Let. 66 (2012) 335-338.

[14] P.P. Bhingole, G.P. Chaudhari, S.K. Nath, Processing, microstructure and properties of ultrasonically processed in situ MgO-Al_2O_3-$MgAl_2O_4$ dispersed magnesium alloy composites, Composites: Part A 66 (2014) 209-217.

[15] Z. Zhang, D.L.Chen, Consideration of Orowan strengthening effect in particulate-reinforced metal matrix nanocomposites: A model for predicting their yield strength, Scr. Mater. 54 (2006) 1321-1326.

[16] Z. Zhang, D.L. Chen, Contribution of Orowan strengthening effect in particulate-reinforced metal matrix nanocomposites, Mater. Sci. Eng. A 483-484 (2008) 148-152.

[17] K.T. Ramesh, Nanomaterials - Mechanics and Mechanisms, Springer, New York, (2009) 134.

[18] G. Gottstein, Physical Foundations of Materials Science, Springer Verlag, Berlin Heidelberg, (2004) 274.

[19] N. Saheb, T. Laoui, A.R. Daud, M. Harun, S. Radiman, R. Yahaya, Influence of Ti addition on wear properties of Al-Si eutectic alloys, Wear 249 (2001) 656-661.